Modeling Dynamic Rock Mass Deformation with the Numerical DDA Method

Thesis submitted in partial fulfillment
of the requirements for the degree of
"DOCTOR OF PHILOSOPHY"

by

Dagan Bakun Mazor

Submitted to the Senate of Ben-Gurion University of the Negev

November 2011

Beer-Sheva

Modeling Dynamic Rock Mass Deformation with the Numerical DDA Method

Thesis submitted in partial fulfillment
of the requirements for the degree of
"DOCTOR OF PHILOSOPHY"

by

Dagan Bakun Mazor

Submitted to the Senate of Ben-Gurion University of the Negev

Approved by the advisors:

Prof. Yossef H. Hatzor _____

Prof. Steven D. Glaser _____

Approved by the Dean of the
Kreitman School of Advanced Graduate Studies _____

November 2011

Beer-Sheva

This work was carried out under the supervision of

Prof. Yossef H. Hatzor

From the Department of Geological and Environmental Sciences,

Ben-Gurion University of the Negev, Israel

Prof. Steven D. Glaser

From the Department of Civil and Environmental Engineering,

University of California Berkeley, CA, USA.

The work was carried out in the

Department of Geological and Environmental Sciences

Faculty of Natural Sciences

ACKNOWLEDGMENTS

I am very fortunate to have received Prof. Yossef H. Hatzor's guidance throughout the past six years. I am grateful for his outstanding professionalism, for him believing in me and supporting me through rough moments, and for letting me grow on my own and spread my wings.

I also wish to express my special thanks to Prof. Steven Glaser from University of California, Berkeley, for his guidance, and for many hours of discussions and brain storming.

I would like to express my gratitude to Dr. William S. Dershowitz, and Prof. Carlos J. Santamarina, who contributed from their broad knowledge and took part in the co-written papers.

Dr. Gen-hua Shi is gratefully acknowledged for making the most recent version of 3D-DDA code available for this study, and for providing the formulations I used in the analytical solution for dynamic block sliding.

I would like to thank my Ph.D candidate committee: Prof. Oren Vilnay, from the Dept. of Structural Engineering at BGU, Dr. Mark Talesnick from the Faculty of Civil and Environmental Engineering at the Technion and Prof. Yehuda Eyal from the Dept. of Geological and Environmental Sciences at BGU, for their suggestions and discussions.

I am heartily thankful to the faculty members in our department: Prof. Yehuda Eyal who taught me much about "Mechanical layering" structures and to Dr. Michael Tsesarsky, for his educated contribution and his DDA experience.

Financial support from the U.S.–Israel Bi-national Science Foundation (BSF) through research grant agreement 2004-122 is gratefully acknowledged. I would like also to thank the Kreitman School for Advanced Graduate Studies for the Negev fellowship; Dr. Levi Kroitoru, Dr. Ilan Bruner, and Dr. Adi Padan for the Assaf Gur Memorial Award of outstanding thesis, and to the Shimshilashvily family for the Eli Shimshilashvily Memorial Award for excellent TA.

Mr. Joel Carr and the research group at UC Berkeley Davis Hall laboratory are thanked for professional assistance in conducting shaking table experiments. My friend Omer Biran is thanked for assistance with direct shear tests performed at BGU.

The Israel Nature and Parks Authority (INPA) and Eitan Campbell from Masada National Park are gratefully thanked for assistance in the installation of monitoring devices and their warm hospitality in Masada. Dr. Ulrich Corsmeier from Karlsruhe Institute of Technology is thanked for sharing his data from the West Masada metrological station.

Data for the geoDFN-DDA models were taken from the Ramleh open pit mine of the Israel Cement Enterprises Ltd. Uri Mor is thanked for his help during field inspections and discussion.

I wish to thank the administrative staff of our department, firmly headed by Mrs. Rivka Eini, for her help in smoothening up the university bureaucracy. The technical staff of the department is thanked for all the support provided during the years. Special thanks are extended to our lab neighbor Mr. Diro Kozashvily.

My friends from the geological department: Ilia Wainshtein, Gony and Omer Biran, Ronnie and Tamir Kamai, Uri Nachshon, Shahar Shani-Kadmiel and Dr. Huirong Bao are gratefully thanked for helpful discussions. Not forgetting my friends who spent their time with me in the field: Yuval Tal, Elahanan Livne, Matan Cymbalista, Noam Morodish, and Asaf Inbal.

I wish to express my deep gratitude to my beloved family for their unlimited support. Special thanks to Yaara Mazor for her English reviews.

Finally, to the one who has been with me all throughout, consulting, understanding and supporting me with endless love: my wife Hagar.

THIS DISSERTATION IS DEDICATED TO MY BELOVED WIFE, HAGAR

ABSTRACT

This work focuses on studying the dynamic response of rock masses to seismic and thermal loading, accompanied by the development of an enhanced procedure to simulate realistic rock mass structures numerically.

The numerical Discontinuous Deformation Analysis (DDA) method for computing large deformations in rock masses is used in this research. The recently developed three dimensional version of the method (3D-DDA) is verified and validated using analytical solutions and shaking table experiments for the dynamic response of a three dimensional wedge-shaped block loaded by seismic vibrations. The well established two-dimensional code (2D-DDA) is utilized to model seismically-induced block displacement for a case study in Masada Mountain.

Preliminary attempts to model complex geological structures using the numerical DDA method revealed a shortcoming in the ability of the existing DDA line generation and block cutting algorithms to simulate common fracture patterns in sedimentary rock masses which comprise the bulk of the exposed outcrops in Israel. To overcome this limitation, a pre-processor is developed in this research based on an existing code (FRACMAN) which allows to assign different statistical distributions to structural parameters and to impose realistic geological constraints on numerical Discrete Fracture Networks (DFN). The DFN model is then imported as vector-based numerical data to the DDA block cutting algorithm in order to obtain a numerical mesh of finite blocks.

An original analytical solution is proposed for considering short-period dynamic problems in rock slope stability, such as a 3D block that is loaded by seismic vibrations. Analytical and 3D-DDA numerical solutions for dynamic sliding of a tetrahedral wedge-shaped block are compared with results of shaking table experiments performed on a concrete model, the interface friction of which is determined by direct shear tests in the lab. Results of constant and variable velocity direct shear tests reveal that the tested concrete interface exhibits a velocity weakening behavior. This is confirmed by shaking table experiments where friction degradation upon multiple cycles of shaking culminated in block run-out. The measured shaking table results are fitted with the proposed 3D analytical solution to obtain a remarkable linear logarithmic relationship between friction coefficient and sliding velocity which remains valid for five orders of magnitude of sliding velocity. It is concluded that velocity-dependent friction along rock discontinuities should be integrated into dynamic rock slope analysis, either analytical or numerical, to obtain more realistic results when strong

seismic ground motions of relatively long duration are considered.

In addition to the short-period dynamic loading, new evidence for long-period thermal response of rock masses is indicated from electronically monitored rock blocks from the natural rock slopes of the Masada Mountain. A "ratchet" model for thermally-induced wedging failure mechanism is presented to explain how cyclic thermal oscillations may induce an extremely low rate of uni-directional block translation. Physical and mechanical lab tests provide the assumed depth of penetration of the heating front during seasonal cycles of exposure as well as the thermal expansion coefficient of the rock mass. These, along with the shear stiffness of the sliding interface, allow quantifying the expected thermally induced displacement rate of blocks in Masada through the proposed wedging-ratcheting failure mechanism.

A distinct block in the East slope of the mountain exhibiting a tension crack opening of 200 mm was monitored for displacement and temperature during a single seasonal cycle in 1998. The mapped geometry of the block in the East face is simulated under cycles of earthquake vibrations utilizing the 2D-DDA, based on the assumed seismicity of the region, the known topographic site effect, and the laboratory measured frictional resistance of the sliding interface.

It is found that for a time window of 5000 years, the observed 200 mm displacement of the East slope block is more likely to have been thermally, rather than seismically, controlled. This result implies that in climatic regions where the temperature amplitude over a seasonal cycle is sufficiently high, thermally induced displacements play an important role in rock slope erosion, where a wedging – ratcheting failure mechanism is possible.

The contribution of this study is that it improves the ability to analyze rock masses deformation according to dynamic environmental loading. The enhanced approach developed in this research allows create numerically complex rock structures and utilize them for dynamic rock masses simulations. The newly developed analytical solution for dynamic sliding in 3D enables to study the velocity dependency of interface friction degradation. This contribution is very important for understanding block run-out during rock slope failures and for improvement of numerical methods used in this scope. Finally, the thermally induced "ratchet" model demonstrates in new light the influences of temperature fluctuations on rock slope stability. Yet, it is recommended that the feasibility of the "ratchet" mechanism should be studied more deeply in future researches using laboratory experiments and by implementing coupled thermo-mechanical solutions.

TABLE OF CONTENTS

LIST OF FIGURES

LIST OF TABLES

CHAPTER 1 – INTRODUCTION

1.1 Overview

Rock masses are fractured by nature; therefore dynamic failure typically occurs by deformation along pre-existing discontinuities. Consequently, dynamic analysis of rock structures requires knowledge about the mechanical and geometrical properties of bedding planes, faults, and any other type of fracture. The most important geometrical variables are orientation (dip and dip-direction), the trace length, and spacing between two adjacent discontinuities. These are determined in the field from boreholes, excavations, or natural outcrops using traditional scan-line or window surveys, or novel methods such as digital image processing. Mechanical properties of the discontinuities are determined both by field surveys and lab experiments.

Once rock mass characterization is obtained, mathematical approaches are employed to analyze static and dynamic problems of removable blocks that are formed by intersection of pre-existing fractures and excavated free surfaces in the rock mass and half-space combinations that have the potential of sliding as rigid bodies towards a certain direction are determined. Naturally, without the application of external forces, removable rock blocks remain static in the rock mass due to shear resistance along discontinuity interfaces.

Various environmentally controlled mechanisms have been considered in an attempt to explain slope failures in rock masses along pre-existing discontinuities: high-magnitude earthquakes, pore pressure buildup in rock joints, freezing and thawing of water in joints, and more recently, thermally induced stresses due to climatic fluctuations. These driving mechanisms have been suggested as triggers for landslides and sizeable rock collapses.

This research focuses on the development of an enhanced procedure to simulate numerically realistic rock mass structures based on geological field mapping, and on the dynamic response of removable blocks to both short-term seismic loading and long-term thermal fluctuation.

1.2 Research objectives

The research presented in this dissertation focuses on the dynamic behavior of rock masses, with emphasis on rock slope stability. The objectives of this research are:

1) To develop an approach to simulate realistic, complex geological fracture patterns.

2) To verify the three-dimensional Discontinuous Deformation Analysis (3D-DDA) code using a newly developed analytical solution and results from shaking table experiments.

3) To suggest a new model for thermally induced block displacements in discontinuous rock slopes based on "ratcheting" mechanism.

1.3 Thesis outline

The contents of the dissertation are arranged in the following order: Chapter 2 is a brief overview of the analytical, numerical and experimental methods used in the context of slope stability analysis. Chapter 3 presents a new approach, which combines two numerical methods: the discrete fracture network (DFN) and the discrete element discontinuous deformation analysis (DDA), and allows simulating rock mass deformation in complex geological structure patterns. The results are discussed in this chapter in terms of underground opening stability and surface settlement, and have been published as a scientific paper in the *International Journal of Rock Mechanics and Mining Sciences* (Bakun-Mazor et al., 2009),

In chapter 4, the role of interface friction is studied by slow direct shear tests and rapid shaking table experiments in the context of short-period dynamic slope stability analysis. A new analytical solution for dynamic sliding in three-dimensions (3D) is proposed and used for both verification of 3D-DDA code and evaluation of friction degradation from shaking table results. This chapter has been published as a scientific paper in the *International Journal for Numerical and Analytical Methods in Geomechanics* (Bakun-Mazor et al., 2012).

Chapter 5 presents a new model for thermally induced block displacements in discontinuous rock slopes, using results of field monitoring campaigns from the East and West rock slopes of the Masada Mountain. The applicability and limitation of the proposed failure mechanism are considered and the comparison between climatic and seismic driving mechanisms is discussed. Chapter 5 has been submitted recently to the *International Journal of Rock Mechanics and Mining Sciences* as a scientific paper. Finally, chapter 6 summarizes the key findings of this research.

CHAPTER 2 – RESEARCH METHODS

2.1 Analytical methods

2.1.1 Block theory

Rock masses are inherently three-dimensional, therefore stability analysis in rock slopes calls for a truly three dimensional (3D) approach. A 3D limit equilibrium analysis for rock slopes has been formulated using stereographical projection coupled with vector algebra (Londe et al., 1969; Goodman, 1976; Hoek and Bray, 1981; Goodman and Shi, 1985). In their book on Block Theory Goodman and Shi (1985) address mathematically the removability of a block bounded by an arbitrary number of surfaces and show how to determine the applicable failure mode. Once the failure mode is established, whether single or double face sliding, static equilibrium is formulated to evaluate the factor of safety against sliding.

Utilizing the original static limit equilibrium formulation presented by Goodman and Shi (1985), a new analytical solution for dynamic block sliding in 3D is developed in this thesis (see chapter 4).

2.1.2 Newmark type analysis

Considering seismically-induced dynamic deformation in rock slopes, a solution for rigid block sliding on a single plane was suggested both by Newmark (1965) as well as Goodman and Seed (1966). This procedure, largely known as "Newmark type analysis", assumes that permanent deformation initiates when earthquake-induced inertial forces acting on a potential sliding block exceed the yield resistance of a slip surface (Wartman et al., 2003). The cumulative displacement of the block is calculated by integrating the acceleration time history twice, while the yield acceleration is used as a reference datum (see Figure 2-1). The original Newmark analysis is based on the assumptions that the block is subjected to one component of horizontal input motion (neglecting the other two components of shaking) and that the shear resistance of the interface does not change with ongoing cycles of motion. It should be pointed out, however, that already in the pioneering paper by Goodman and Seed (1966), a procedure to account for friction degradation as a function of number of cycles was proposed and demonstrated (Figure 2-1). Although Yan (1991) modified the original Newmark procedure to account for vertical accelerations, an analytical approach that takes into full account all three dimensional components of vibrations simultaneously has not been proposed to date.

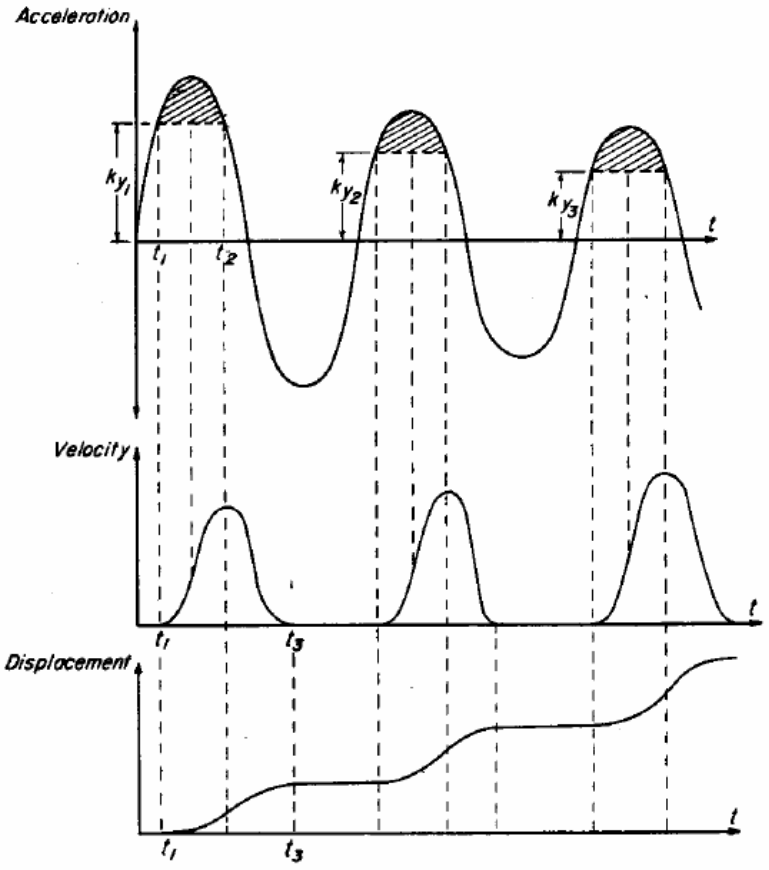

Figure 2-1. Illustration for the concept of the "Newmark's type analysis": The displacement in the lower figure results from the double integration of the acceleration function in the upper figure between t1 and t2 - beyond the yield acceleration (ky in this figure) (Goodman and Seed, 1966).

2.1.3 Rate and state

The time dependency of frictional resistance is very important in slope stability analysis as rock avalanches formed by large scale failures of bedrock may be triggered when frictional resistance is diminished with cycles of motion and sliding velocity. Besides changes in pore pressure due to climate effects (Hermanns et al., 2004) or thermo-poro-mechanical effects (Vardoulakis, 2000; Veveakis et al., 2007; Goren and Aharonov, 2009), friction angle degradation during slip may be explained by rock fragmentation (Davies and McSaveney, 2009; Taboada and Estrada, 2009), subtle anisotropy in grain arrangements on the interface (Friedmann et al., 2003), or rate and state effects (Dieterich, 1979; Ruina, 1983). Friction degradation during slip requires a modification of the Newmark analysis (Matasovic et al., 1998), by incorporating a shear strength degradation criterion as a function of either displacement (Goodman and Seed, 1966) or velocity (Sornette et al., 2004; Mandez et al.,

2009). For rate dependency, Dieterich (1979) and Ruina (1983) proposed the 'rate and state' friction laws where the friction coefficient is a function of both slip rate and a state variable:

$$\mu = \mu_0 + A\ln\left(\frac{V}{V_0}\right) + B\ln\left(\frac{\theta V_0}{D_c}\right) \tag{2.1}$$

where μ_0 is a reference friction coefficient under a constant reference slip rate V_0, V is the sliding velocity, A and B are dimensionless empirical fitting parameters which respectively characterize the sliding and time dependence of friction, D_c is a characteristic slip distance essential to reach steady-state sliding, and θ is a state variable. The most commonly used state evolution law is known as 'Dieterich law':

$$\frac{d\theta}{dt} = 1 - \frac{V\theta}{D_c} \tag{2.2}$$

Figure 2-2 shows schematically the observed frictional response to a sudden imposed change in sliding velocity. The parameter A, known as the direct velocity effect, is related to the change in rate, and the parameter B is related to the change in state. As illustrated in Figure 2-2 the friction coefficient at steady state is:

$$\mu = \mu_0 + (A - B)\ln\left(\frac{V}{V_0}\right) \tag{2.3}$$

Thus, steady state friction exhibits velocity weakening if B is greater than A, and velocity strengthening otherwise. The rate and state friction laws have been used to address various geophysical problems, as comprehensively reviewed by Scholz (1998).

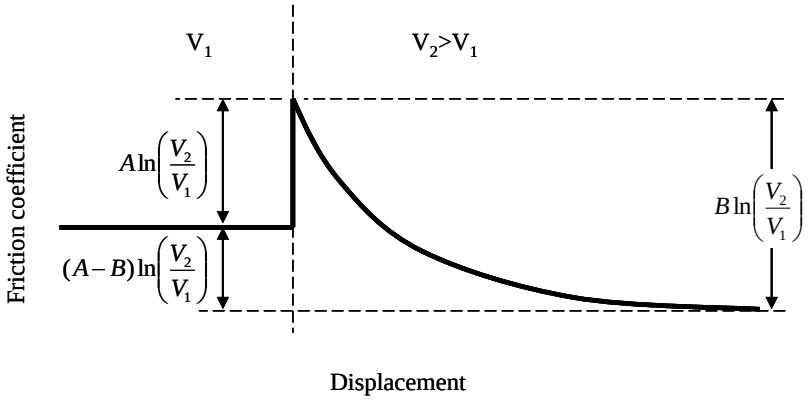

Figure 2-2. The concept of "rate-and-state" (velocity weakening): Illustration for the experimentally observed frictional response to sudden increase in sliding velocity.

2.2 Experimental methods

2.2.1 Shaking table

In order to study the dynamic sliding response of a single block subjected to horizontal input motion, the single-degree-of-freedom, hydraulically-driven, shaking table of the Earthquake Simulation Laboratory at U. C. Berkeley is used in this research. The centerpiece of the shaking table system is a 38 inch wide by 48 inch long horizontal plate driven by a 222.4 kN (50 kip) force, 15.24 cm (6 in.), closed-loop servo-controlled hydraulic actuator manufactured by MTS (Series 244). A Hewlett Packard model 33120A arbitrary function generator produced the table command signal. The function generator is capable of producing constant-amplitude repetitive signals such as sinusoidal, triangular, or square functions.

Measurement instrumentation consisting of accelerometers and displacement transducers are attached to the shaking table and to the experimental system, as described in chapter 4. The accelerometers are DC-response type (Model 141 manufactured by Setra), have a nominal range of +/- 2 *g*, exhibit a flat response between 0 to 200 Hz and nominal natural frequency of 300 Hz. Prior to testing, the accelerometers are calibrated in the field of gravity. The accelerometers, 30 gr in weight, are screwed to both the shaking table plate and the experimental system. Linear variable displacement transducers (LVDT) measure the position of both shaking table and sliding block. A DL750 ScopeCorder manufactured by Yokogawa is used as both oscilloscope and data recorder in acquisition rate of 100 Hz.

A general view of the shaking table setup is shown in Figure 2-3, while a detailed explanation of the test settings is given in chapter 4.

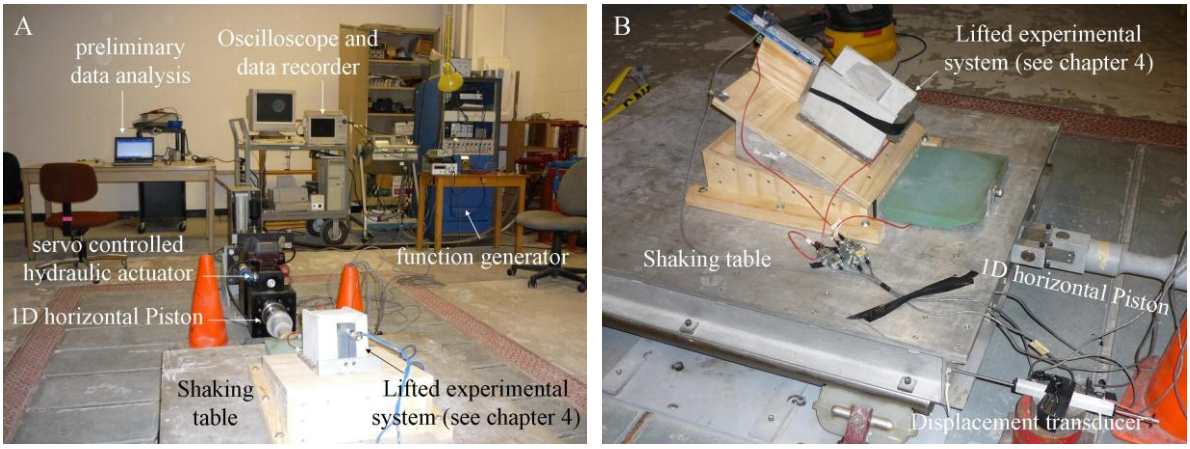

Figure 2-3. Front (A) and side (B) views of the shaking table setting set up at the Earthquake Simulation Laboratory, U. C. Berkeley.

2.2.2 Direct Shear

In this research, both peak and residual friction angles are determined experimentally using the direct shear apparatus at Ben-Gurion University rock mechanics laboratory. The direct shear apparatus, manufactured by TerraTek, is a servo controlled test system built of two load frames, normal and shear, combined to act simultaneously (Figure 2-4A). The normal and shear load cell capacities are 1000 kN and 300 kN, respectively. The tested samples are cemented into the upper and lower 180×180×140 mm^3 shear boxes (Figure 2-4B), using Portland 350 cement.

Shear and dilatational displacements are monitored by six LVDTs, with a maximum range of 50 mm and 0.25% linearity full scale: the vertical (dilatational) displacements are monitored by four LVDTs, mounted on four corners of the shear box; The horizontal (shear) displacements are monitored by two LVDTs, mounted on two opposite sides of the tested interface. Utilizing a computer control interface, output signals from all channels can be used as servo control variables at an acquisition rate of 50 Hz. The average value of the two shear displacement transducers output is used to control the sliding velocity, and the output from the normal piston load cell is utilized to control the normal stress during sliding.

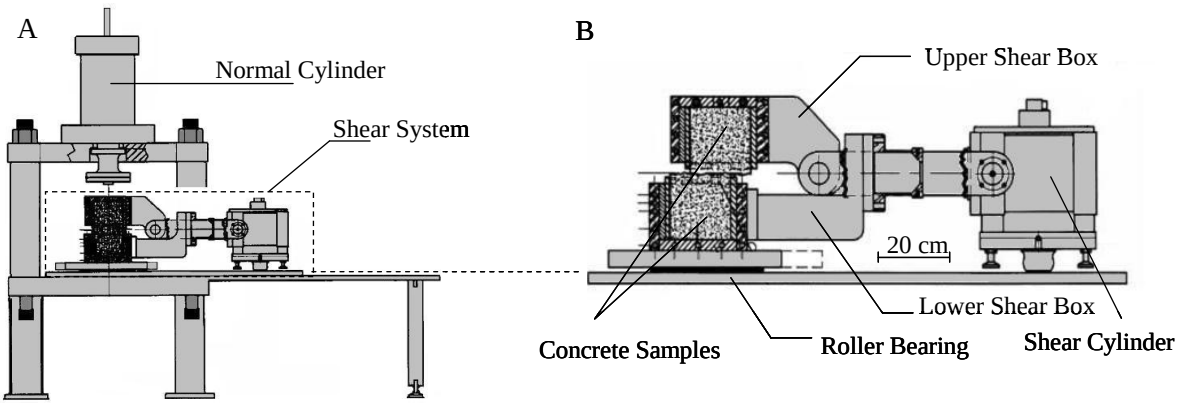

Figure 2-4. Direct shear testing setup at the Ben-Gurion University rock mechanics laboratory: A) Layout of the servo-controlled direct-shear load frame, B) Details of the shear box assembly.

2.3 Numerical methods

Over the last three decades, different numerical methods have been developed for modeling continuous and discrete systems. The computational process of the continuous approach is obtained by discretization of the continuum, and by sub-division of the problem domain into a large number of standard-shaped elements, with a finite number of degrees of freedom. The most common and popular numerical method is the Finite Element Method (FEM) (e.g. Cravero and Iabichino, 2004) which may have a simple problem geometry (by adopting only a very few, limited dominating discontinuities), but cannot address the effects of fracture population on the material behavior and properties. The Distinct Element Method (DEM) (Cundall, 1988; Hart et al., 1988) approach, on the other hand, treats the material domain concerned as an assemblage of individual blocks (or particles for granular materials) interfaced by discontinuities. In this research which focuses on analysis of discontinuous rock masses, the Discontinuous Deformation Analysis (DDA) approach is extensively used. The basic concepts of DDA method are provided below. The DDA method is used here for both short term dynamic response of sliding blocks to seismic loading and long period accumulated response to thermally-induced cyclic loading.

2.3.1 Basic concepts of DDA

The DDA is a special type of DEM proposed by Shi (1988) to provide a useful tool for investigating the kinematics of blocky rock masses. Similar to the DEM approach, DDA models the discontinuous media as a system of individual deformable blocks that move independently without interpenetration. However, the formulation of the blocks is very similar to the definition of a finite element mesh, but where all the elements are bounded by pre-existing discontinuities and the unknowns of the equations are the displacements and deformations of the blocks. The blocks, or elements, are not restricted to standard shapes as in FEM, but can be of any convex or concave shape. Although originating from the DEM family, DDA closely parallels the FEM and is basically a generalization of it (Shi, 1988).

In this research both two-dimensional (2D) and three-dimensional (3D) DDA versions are used. While in 2D version there are six degrees of freedom per block (two translations, one rotation, two normal strains, and one shear strain) the 3D contains twelve degrees of freedom (three translations, three rotations, three normal strains, and three shear strains). Since equilibrium is required for each degree of freedom of each block, there are six and twelve equilibrium equations per block, in the 2D and 3D versions, respectively. The

description of DDA formulation is presented here for the 3D version.

Basic formulation for 3D-DDA

Assuming linear elasticity and homogeneous deformation, the displacement (u, v, w) of any point (x, y, z) of the i[th] block can be related in three dimensions to twelve displacement variables:

$$[D_i] = \left(u_0 \; v_0 \; w_0 \; r_1 \; r_2 \; r_3 \; \varepsilon_x \; \varepsilon_y \; \varepsilon_z \; \gamma_{xy} \; \gamma_{yz} \; \gamma_{zx}\right)^T \tag{2.4}$$

where (u_0, v_0, w_0) are the rigid body translation of a specific point (x_0 ,y_0 , z_0), r_1, r_2 and r_3 are the rotation angles (in radians) of the block around z-axis, x-axis and y-axis, respectively, and the coefficients ε_x, ε_y, ε_z, γ_{xy}, γ_{yz}, γ_{zx} are the normal and shear strains in the block. By adopting a first order displacement approximation, the displacement of any point (x, y, z) in the block can be represented by:

$$\begin{pmatrix} u \\ v \\ w \end{pmatrix} = [T_i][D_i] = \begin{bmatrix} 1 & 0 & 0 & -(y-y_0) & 0 & (z-z_0) & (x-x_0) & 0 & 0 & \frac{(y-y_0)}{2} & 0 & \frac{(z-z_0)}{2} \\ 0 & 1 & 0 & (x-x_0) & -(z-z_0) & 0 & 0 & (y-y_0) & 0 & \frac{(x-x_0)}{2} & \frac{(z-z_0)}{2} & 0 \\ 0 & 0 & 1 & 0 & (y-y_0) & -(x-x_0) & 0 & 0 & (z-z_0) & 0 & \frac{(y-y_0)}{2} & \frac{(x-x_0)}{2} \end{bmatrix} \cdot [D_i] \tag{2.5}$$

Assuming that n blocks are defined in a block assembly, the system of simultaneous equilibrium equations can be written in the matrix form as:

$$\begin{pmatrix} K_{11} & K_{12} & K_{13} & \cdots & K_{1n} \\ K_{21} & K_{22} & K_{23} & \cdots & K_{2n} \\ K_{31} & K_{32} & K_{33} & \cdots & K_{3n} \\ \vdots & \vdots & \vdots & \ddots & \vdots \\ K_{n1} & K_{n2} & K_{n3} & \cdots & K_{nn} \end{pmatrix} \begin{pmatrix} D_1 \\ D_2 \\ D_3 \\ \vdots \\ D_n \end{pmatrix} = \begin{pmatrix} F_1 \\ F_2 \\ F_3 \\ \vdots \\ F_n \end{pmatrix} \tag{2.6}$$

Where each coefficient K_{ij}, is defined by the contacts between blocks i and j, and where $i = j$ it depends on the material properties of block i alone. Since each block has twelve degrees of freedom, each element K_{ij} in the coefficient matrix is a 12 X 12 submatrix. The system in Equation (2.6) can also be expressed in the compact form as KD = F where K is a 12n X 12n stiffness matrix, and D and F are 12n X 1 deformation and force matrices, respectively.

The total number of unknown deformations is the sum of the degrees of freedom of all the blocks. The total potential energy Π is the summation over all potential energy sources; stresses and forces. The simultaneous equations are derived by minimizing the total potential energy Π of the block system:

$$k_{ijrs} = \frac{\partial^2 \Pi}{\partial d_{ri} d_{sj}}, \quad r,s = 1,2,...,12$$
$$F_{ir} = -\frac{\partial \Pi(0)}{\partial d_{ri}}, \quad r = 1,2,...,12 \tag{2.7}$$

where

$$d_{ri} = \begin{pmatrix} d_{1i} & d_{2i} & d_{3i} & \cdots & d_{12i} \end{pmatrix}^T = \begin{pmatrix} u_i & v_i & w_i & r_{1_i} & r_{2_i} & r_{3_i} & \varepsilon_{x_i} & \varepsilon_{y_i} & \varepsilon_{z_i} & \gamma_{xy_i} & \gamma_{yz_i} & \gamma_{zx_i} \end{pmatrix}^T$$
$$d_{sj} = \begin{pmatrix} d_{1j} & d_{2j} & d_{3j} & \cdots & d_{12j} \end{pmatrix}^T = \begin{pmatrix} u_j & v_j & w_j & r_{1_j} & r_{2_j} & r_{3_j} & \varepsilon_{x_j} & \varepsilon_{y_j} & \varepsilon_{z_j} & \gamma_{xy_j} & \gamma_{yz_j} & \gamma_{zx_j} \end{pmatrix}^T$$

and the subscripts *i* and *j* represent the *i*-th block and the *j*-th block, respectively. The solution for the system in Equation (2.7) is constrained by a system of inequalities associated with block kinematics. Block system kinematics in DDA avoids penetration and tension between blocks. These two constraints are applied using a "penalty" method, in which stiff springs are attached to block contacts. Since tension or penetration at the contacts will result in extension or contraction of the springs, a process that requires energy, the minimum energy solution is one with no tension or penetration.

When the blocks are in contact, Coulomb's friction law applies to the contact interface, and the simultaneous equilibrium equations are formulated and solved for each loading or time increment. When the blocks are separated, the virtual spring is removed. DDA considers both statics and dynamics using a time-step marching scheme and an implicit algorithm formulation. The static analysis assumes the velocity as zero at the beginning of each time step, while the dynamic analysis inherits the velocity of the previous time step. The integration of a polynomial function over a general polygon area is performed in DDA using the analytical Simplex solution.

Previous works on DDA

Due to its rigorous scheme of block kinematics and equilibrium conditions achieved by minimizing the total potential energy, DDA has attracted the attention of research and geotechnical engineering worldwide. With many people contributing to its development and application, the original 2D-DDA is well developed in terms of both theory and computer coding (e.g. MacLaughlin et al., 2001; Sitar et al., 2005). However, 2D DDA is applicable only to 2D problems, usually plane strain or plane stress.

In contrast to the case of the original 2D version, only a limited number of attempts to

check the validity and accuracy of 3D-DDA have recently been published (e.g. Yeung et al., 2003; Jiang and Yeung, 2004; Liu et al., 2004; Moosavi et al., 2005; Wang et al., 2006; Grayeli and Hatami, 2008; Keneti et al., 2008) perhaps due to the difficulty in developing a complete contact theory that governs the interaction of many 3D blocks (Yeung et al., 2007). Considering 3D validations, Shi (2001) reports very high accuracy for two examples of block sliding modeled with 3D-DDA, subjected to gravitational load only. Moosavi et al. (2005) compare 3D-DDA results for dynamic block displacement with an analytical solution proposed originally by Kamai and Hatzor (2008). Yeung et al. (2003) studied the tetrahedral wedge problem using physical models and field case histories and reported good agreement with 3D-DDA with respect to the obtained failure mode and the block displacement history, although no quantitative comparison between 3D-DDA and lab test results was reported.

2.3.2 Discrete Fracture Network

The Discrete Fracture Network (DFN) (e.g. Dershowitz and Einstein, 1988) method is a special discrete model that considers fluid flow and transport processes in fractured rock masses through a system of connected fractures. The technique was created in the early 1980s for both 2D and 3D problems, and has been continuously developed since, with many applications in civil, environmental and reservoir engineering and other fields of geosciences (Jing, 2003). In this research the commercial FRACMAN code (Dershowitz et al., 2000) is used as a preprocessor in developing a new hybrid geoDFN-DDA approach, which allows to assign different statistical distributions to structural parameters, as described in chapter 3.

CHAPTER 3 - A HYBRID GEODFN-DDA PREPROCESSOR FOR SIMULATING DEFORMATION IN COMPLEX ROCK STRUCTURES

3.1 Introduction

Sedimentary rock masses exhibit a geological structure known as "mechanical layering" (Gross, 1993) where vertical to sub-vertical joints are bounded by bedding plane boundaries (Figure 3-1A), and a ratio between bed thickness and joint spacing is typically defined (Narr and Suppe, 1991; e.g.Gross, 1993; Bai and Gross, 1999). This chapter demonstrates the use of discrete fracture models which incorporate the "mechanical layering" concept to improve stability analysis for underground openings. This potentially represents a significant advance over earlier rock engineering approaches which relied on simplified, statistically based, fracture patterns. These simplified models have typically been parameterized in terms of for example joint persistence (Einstein et al., 1983) joint trace length (Mauldon and Mauldon, 1997) and bridge (Shi and Goodman, 1989b; Kemeny, 2005) (Figure 3-1B).

This chapter presents an approach which combines the "mechanical layering" fracture spatial model (Dershowitz et al., 2000) for sedimentary rock (referred to below as a geologic discrete fracture network or geoDFN) with the discrete element DDA method (Shi, 1993). The DDA approach is applicable for rock masses in which the significant fractures effecting stability must be modeled explicitly. This includes rock masses with more fractures than can be analyzed using the clamped beam models (Obert and Duvall, 1967) and the Voussoir beam analogue (Evans, 1941; Beer and Meek, 1982; Sofianos, 1996; Diederichs and Kaiser, 1999), and rock masses where the number of fractures is insufficient to particle flow code (Cundall and Strack, 1979) or plastic continuum approximations (e.g. Klerck et al., 2004). It is assumed that application of discrete element methods, either DEM (Cundall, 1988; Hart et al., 1988) or DDA (Shi, 1993) is essential for correct stability analysis in such rock masses, provided that the rock mass structure is modeled correctly.

To demonstrate the sensitivity of numerical modeling results to geological structure, the influence of joint and bridge length on rock mass stability is explored by incorporating geoDFN models into the block cutting algorithm of DDA and studying the resulting rock mass deformations. It is concluded that adding such enhanced capabilities to the existing block cutting code of DDA is important for accurate prediction of both roof deflections and surface settlements due to underground mining in fractured rock masses.

3.2 A hybrid approach for modeling rock mass deformation

Truthful numerical simulation of structural patterns in discontinuous rock masses is an important prerequisite for accurate stability assessment of underground openings. As the discussion is limited here to two dimensions, line, rather than plane generation schemes are explored, via the existing FRACMAN software (Dershowitz et al., 2000) and DDA code (Shi, 1993). The statistical trace line generation code in the DDA environment (DL) is based on an important paper by Shi and Goodman (1989b) where joint traces are characterized and simulated using mean joint length (L), bridge (b), and spacing (s) (Figure 3-1B). Line generation in DL is based on a simple Poisson process described by normal distributions for each of the three simulated parameters with user specified degree of randomness (DR), a parameter which controls the degree of deviation from the mean which is allowed during the simulations (see Shi and Goodman, 1989b for details). After line generation is complete all line data are provided to the DDA block cutting code (DC). The block cutting process results in a DDA mesh consisting of closed and discrete blocks with known area, center of mass, and edge coordinates (see Figure 3-1C), all of which are used for the forward modeling DDA code (DF), to obtain rock mass deformation.

The key to successful application of this approach is the generation of a realistic fracture pattern. In sedimentary rocks, it is commonly observed that the fracture pattern is well described by Gross's concept of "Mechanical Layering" (Gross, 1993). This can not be achieved with the standard DL code which is based on a simple Poisson spatial process. In mechanically layered rock masses joint trace lengths are constrained by bedding plane boundaries. The fracture pattern in fractured rock masses with "Mechanical Layering" is described by the Fracture Spacing Index (FSI), defined as the ratio between the mechanical layer thickness and median joint spacing (e.g. Narr and Suppe, 1991).

A hybrid geoDFN-DDA approach is presented here to address exactly such cases. The hybrid approach begins by generating a three dimensional, mechanically layered fracture pattern using FRACMAN which allows the simulation of realistic fracture patterns including spatial correlations and geological processes such as mechanical layering. For the purposes of the two-dimensional DDA analysis, a 2-D trace plane is cut through the three dimensional discrete fracture network model (DFN) to provide a 2D trace model which can be simulated with the DL code. The DDA block cutting algorithm (DC) is then applied to generate a mesh of finite blocks. Once the DDA mesh is constructed forward modeling of deformation can be performed with the DF code. A flow chart showing the essentials of this procedure is shown

in Figure 3-2.

Consider for example a mechanically layered rock mass consisting of one set of horizontal layers (beds) and one set of vertical joints as presented schematically in Figure 3-1 but with specified statistical distributions. The layer thickness in this example are described by log normal distribution with the following parameters: log[mean(m)] = 0, log[deviation(m)] = - 0.2 and minimum layer thickness of 0.7m. A minimum layer thickness is imposed to eliminate generation of unrealistically slim blocks due to the application of a constant fracture spacing index, which in the presented example is set at FSI = 1.3 for all layers, a common value for sedimentary rocks (Ruf et al., 1998). A three dimensional visualization of the mechanically layered rock mass obtained in FRACMAN environment is shown in Figure 3-3A. The computed 2D block mesh for a selected cross section obtained with the DDA DC code is shown in Figure 3-3B. This hybrid FRACMAN - DDA procedure brings together the power of two different geo-engineering tools, one for diverse statistical simulations of geological fracture patterns and the other for robust mechanical deformation analysis.

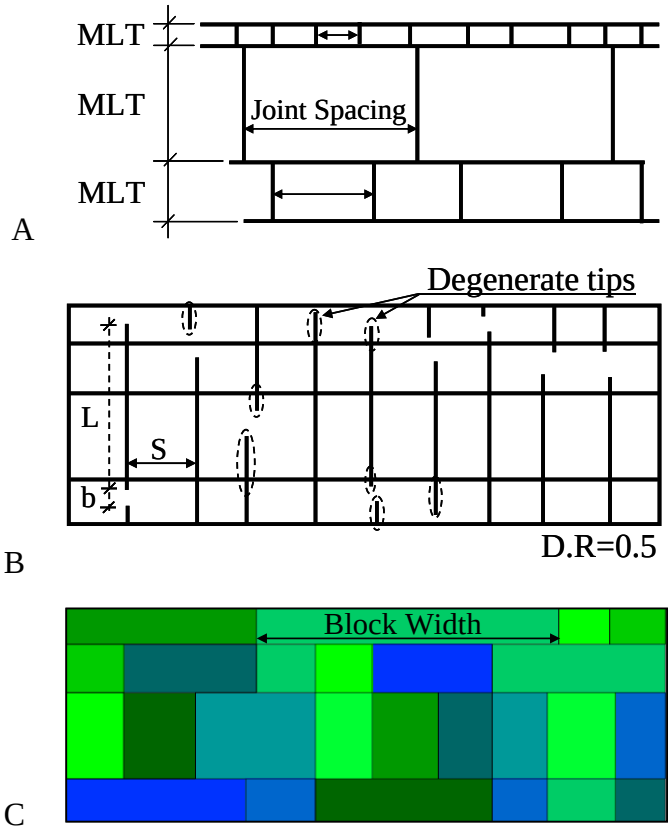

Figure 3-1. A) Schematic diagram illustrating "mechanical layering" in sedimentary rocks (MLT- Mechanical Layer Thickness), B) Definition of terms used in synthetic generation of joint trace maps, mesh generated in DDA line generation code DL, and C) Output of DDA block cutting code (DC).

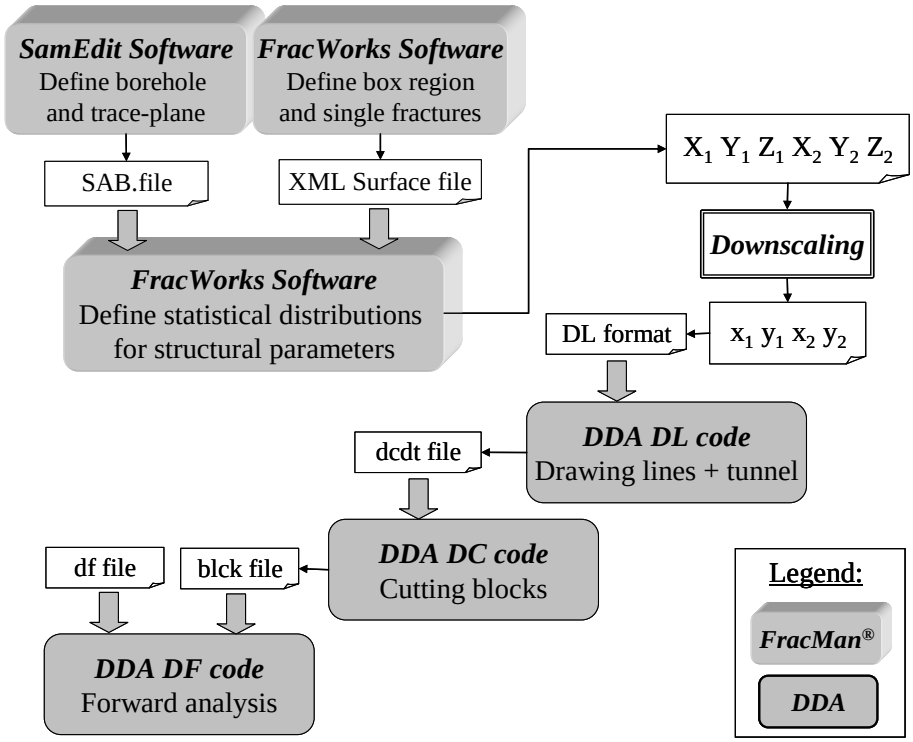

Figure 3-2. Flow chart diagram showing implementation of the hybrid geoDFN-DDA pre processor.

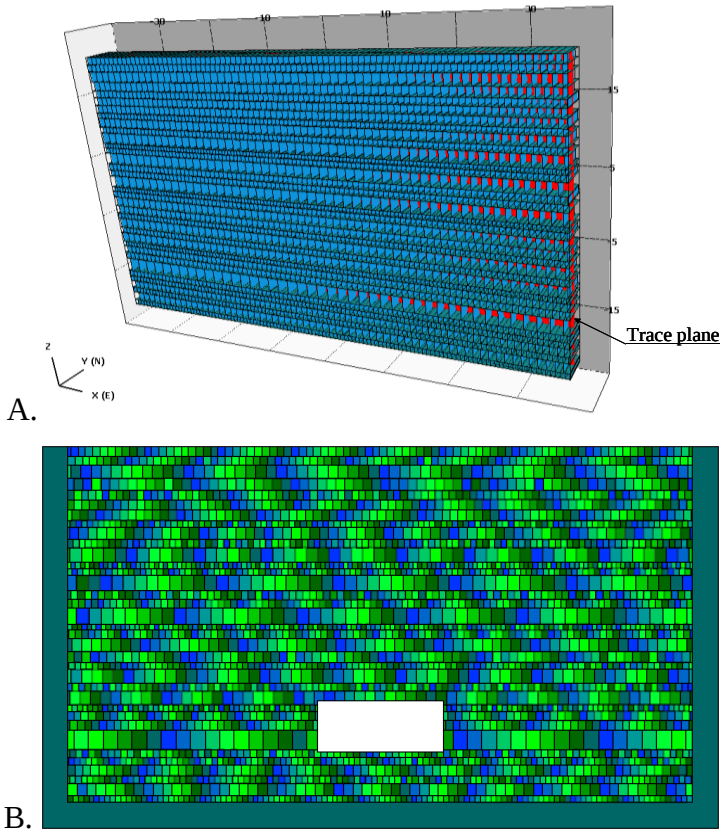

Figure 3-3. A) FRACMAN simulation of mechanically layered rock mass (for structural parameters see text); B) DDA mesh using line coordinate input from FRACMAN.

3.3 Structural analysis of simulated rock masses

To compare between the hybrid geoDFN-DDA and the standard DDA joint trace simulation approaches, structural characteristics are discussed in meshes obtained with the hybrid procedure, where mechanical layering is imposed on the simulation (mesh denoted FMML from now on), and in meshes obtained with the standard DL and DC codes, where mean joint length, bridge, and spacing can be varied within some bounds defined by the degree of randomness. In particular, it is studied how variations in joint length and bridge affect block size distribution in meshes obtained in the two different approaches. In both approaches the same identical layer thickness distribution, obtained using FMML, is used, with an imposed minimum layer thickness of 0.7m. Since an FSI value of 1.3 is imposed in the generation of the FMML mesh, the joint spacing value for the minimum thickness layer in the FMML mesh is set at 0.54m. This joint spacing value is used as the mean joint spacing value for the entire rock mass and a degree of randomness of DR = 0.5 is applied for L, b, and s in all DL simulations. The complete matrix for DDA simulations in this study is provided in Table 3-1 and the outline of the mesh is shown in Figure 3-4 with measurement point location for future reference.

Preliminary analysis of the computed block systems enables to obtain some important structural rock mass characteristics such as number of blocks, block width, and block area distributions, utilizing the powerful integration scheme implemented in the DC block cutting code. This analysis is performed before forward modeling is conducted and relates primarily to structural characterization of the rock mass. Any important geometric characteristic of the simulated rock mass can be studied quantitatively by the meshes generated, and its effect on the mechanical response can be inferred after forward modeling is complete.

Consider for example the block width and block area distributions obtained from DL simulations in comparison to FMML (Figure 3-5). In both FMML and DL simulations the block size distributions obtained are similar. The total number of blocks however, while fixed in the FMML mesh, clearly increases with increasing mean joint length and decreases with increasing mean bridge length. Namely, with increasing mean trace length and decreasing mean bridge length the number of blocks cut by the DC code out of the DL trace maps increases. This observation is intuitive when it is considered that the probability for line intersections in a randomly selected unit area in the rock mass should increase with increasing trace length and with decreasing bridge length. The 2D line intersection probability, a prerequisite for block cutting in the DC code as well as for block formation in the real rock

mass, is discussed elsewhere (Hatzor and Feintuch, 2005). Since layer thickness distribution is fixed in all meshes, with increasing bridge length individual blocks cut by the DC code are expected to be wider, since less blocks will be cut in each layer. This effect is shown graphically in Figure 3-6 using results of all DL simulations. This result has significant effect on rock mass deformation as will be discussed in the following section. Figure 3-5 and Figure 3-6 which describe quantitatively structural characteristics of the rock mass, can be used to obtain some constraints on the expected rock mass geomechanical response, and can enhance engineering judgment concerning the "quality" of the rock mass, a parameter which otherwise must be based on empirical classification methods such as the GSI (Hoek and Brown, 1997), Q (Barton et al., 1974), and RMR (Bieniawski, 1989).

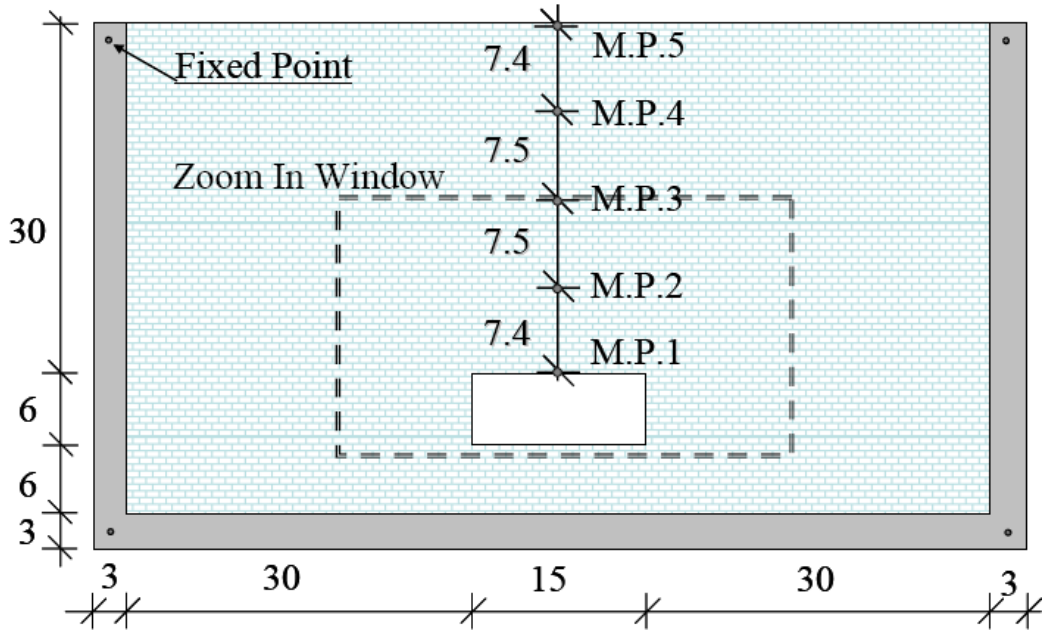

Figure 3-4. Outline of the mesh used for forward DDA simulations (units are meters).

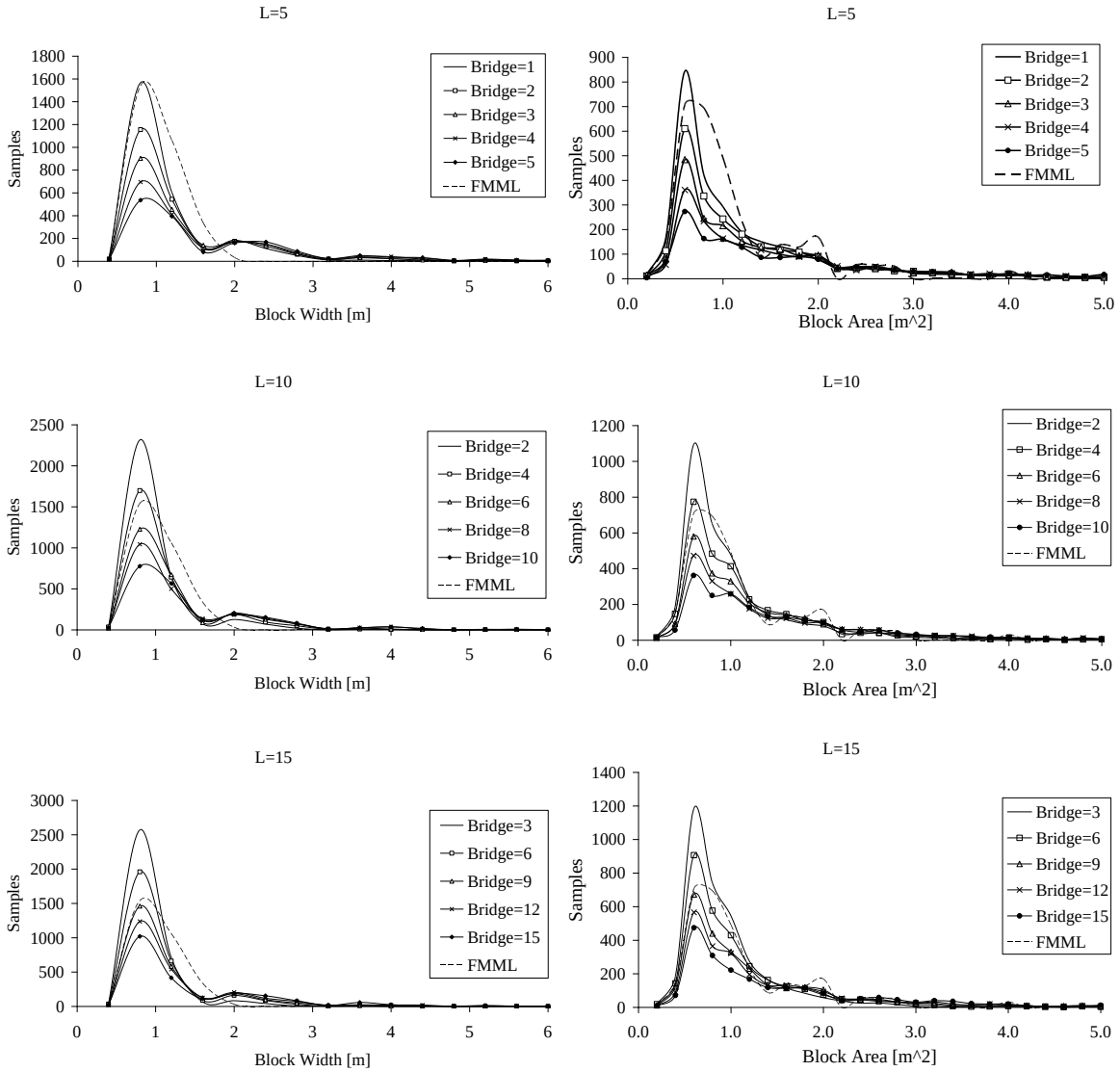

Figure 3-5. Block Width (left) and block size (right) distributions obtained from preliminary analysis.

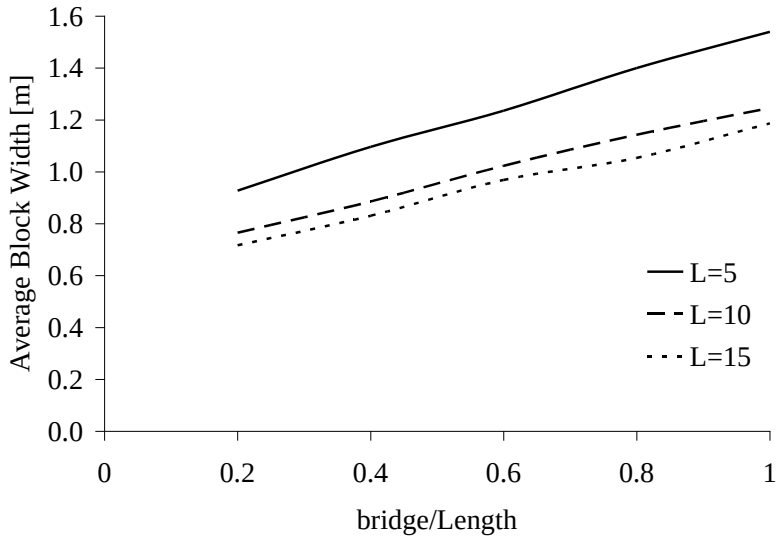

Figure 3-6. Obtained average block width as a function of joint bridge / joint length ratio.

3.4 Mechanical response of simulated rock mass structures

To compare between the deformation of a mechanically layered rock mass and a rock mass simulated by mean joint spacing (*s*), length (*L*), and bridge (*b*) values, the forward modeling code in the DDA environment is employed once for the mesh obtained using the hybrid procedure (FMML), and then for models 1- 15 obtained using DL code (see Table 3-1). The assumed geometrical and mechanical parameters for DDA forward modeling are listed in Table 3-2.

The response of a mechanically layered rock mass to an underground opening with a rectangular geometry is shown in Figure 3-7. The immediate roof which includes measurement point 1 (Figure 3-4) collapses and the opening attains a new equilibrium. Note that the height of the loosened zone is approximately 0.5B, where B is the opening width, which is the probable maximum loosened zone as predicted by Terzaghi (1946) for unsupported horizontally stratified rock mass. Note also that above the loosened zone (around measurement point 2) several individual Voussoir beams are developed and attain a new state of equilibrium following some preliminary vertical deflection. The vertical displacement and axial stress developed in the five measurement points are plotted in Figure 3-8 C and D, respectively. The stabilization of the roof segment containing measurement points 2,3,4, and 5 is indicated by the arrest of the downward vertical deflection (Figure 3-7C) and by the development of stable arching stresses in the beams (Figure 3-7D).

The deformation pattern of the roof for rock structures obtained using standard line generation is shown in Figure 3-8 for mean joint trace length of 5m and 10m (graphical simulation outputs for L = 15m are omitted for brevity). Note that the deformed meshes presented in Figure 3-8 are confined to the zone of interest above the immediate roof, as delineated in Figure 3-4 and Figure 3-7A. The vertical displacement data obtained for the rock mass above the immediate roof (measurement points 3, 4, 5 - Figure 3-4) are sown in Figure 3-9 in terms of the bridge over length (*b/L*) ratio, where the FMML results are plotted as well for reference.

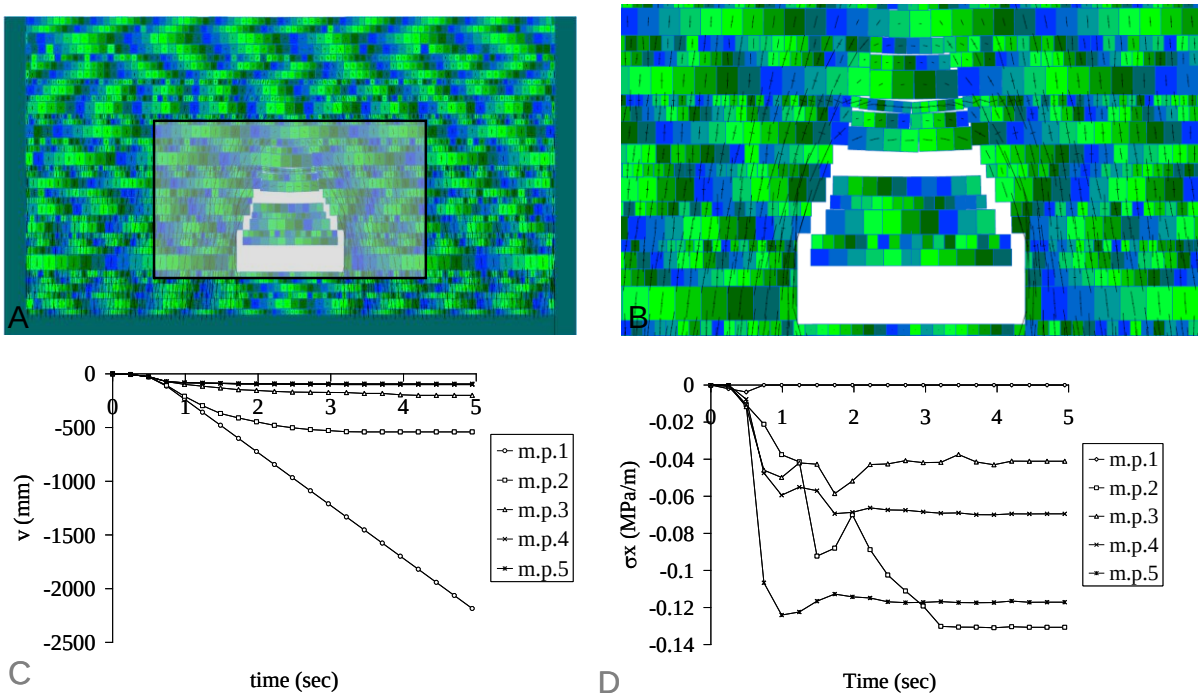

Figure 3-7. Mechanical Layering model (FMML) response. A) Whole deformed model, B) Zoom-in on the loosened zone (see location in Figure 3-4 and Figure 3-7A) , C) Accumulated vertical displacement for 5 sec, and D) Horizontal compressive stress vs. time.

Table 3-1. Matirx of DDA simulations. Legend: *L* = mean joint length, *b* = mean rock bridge, *s* = mean joint spacing, and DR = degree of randomness(Shi and Goodman, 1989a).

Model	L (m)	b (m)	s (m)	D R
1		1		
2		2		
3	*5*	3	*0.54*	*0.5*
4		4		
5		5		
6		2		
7		4		
8	*10*	6	*0.54*	*0.5*
9		8		
10		10		
11		3		
12		6		
13	*15*	9	*0.54*	*0.5*
14		12		
15		15		

Table 3-2. Input parameters for DDA simulations.

Mechanical Properties	
Elastic Modulus, GPa	15.3
Poisson's Ratio	0.21
Density, kg/m^3	2300
Numerical Control Parameters	
Dynamic control parameter	0.99
Number of time steps	10000
Time interval, sec	0.0005
Assumed max. disp. Ratio, m	0.0005
Penalty stiffness, GN/m	0.1
Friction angle, degrees	30

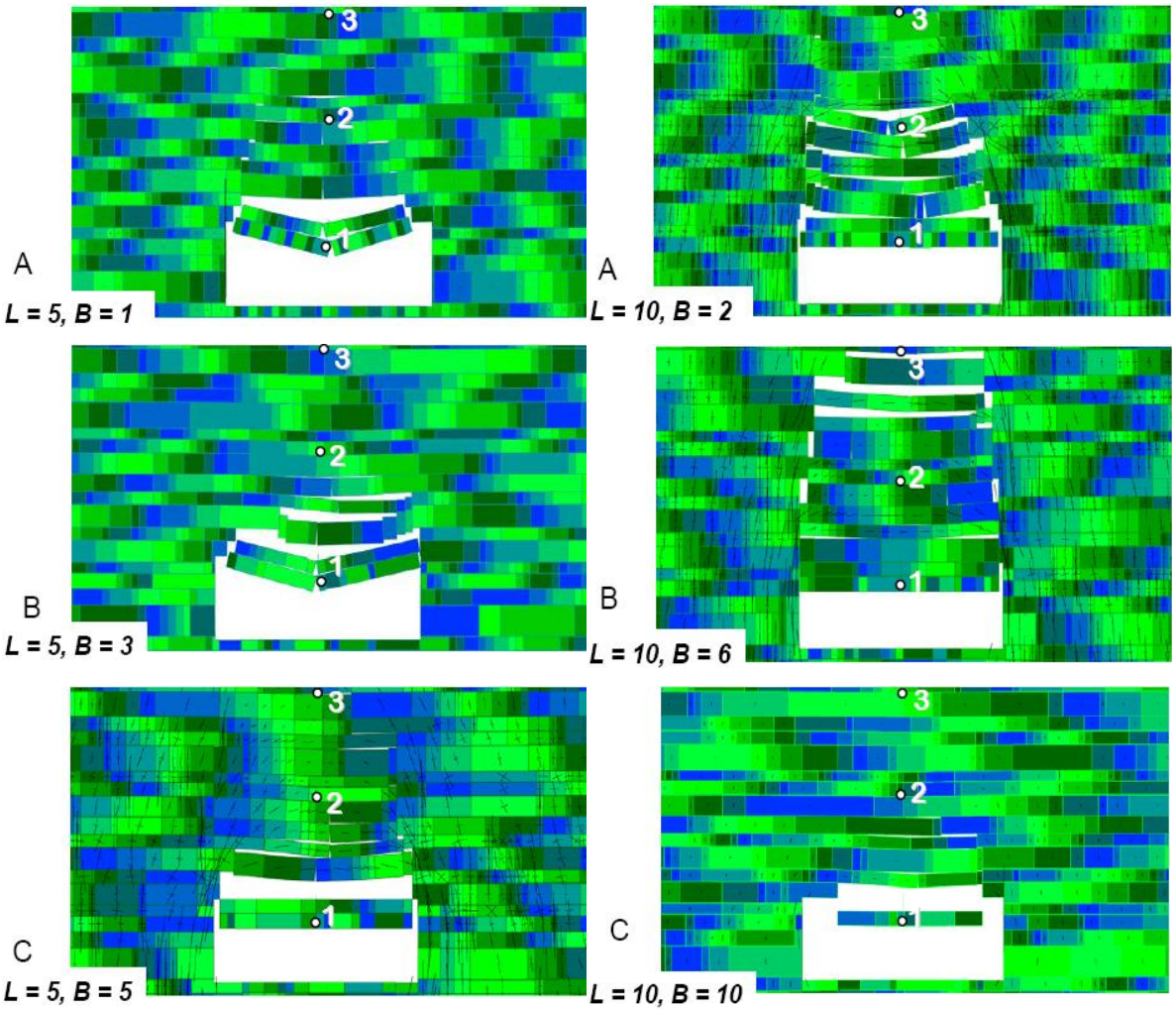

Figure 3-8. Deformation pattern of the roof for different *B/L* ratios and joints length (see Figure 3-4 for perspective location).

3.5 Discussion

3.5.1 The influence of bridge length on the stability of the immediate roof

With increasing bridge length the intersection probability of two joints belonging to two different sets in a randomly selected unit area in the rock mass naturally decreases (Hatzor and Feintuch, 2005). Therefore, with increasing bridge length fewer blocks are expected in the rock mass, as discussed above. In the layered rock mass configuration modeled here this also implies wider blocks in each layer. Previous studies indicate that jointed layer stability increases with increasing block width (Passaris et al., 1993; Ran et al., 1994) up to an optimal width beyond which vertical shear along the abutments will dominate over stable arching – as the dead weight of the overlying continuous beams becomes too high (Hatzor and Benary, 1998). The average block width with respect to beam span in the simulations performed in this research is well within the range for which Hatzor and Benary (1998) found increasing stability with increasing block length (Figure 3-10). This effect is shown here for the two simulated joint trace lengths in the graphical outputs of the deformed meshes in the immediate roof zone (Figure 3-8) but this is particularly evident for the L=10m set of plots. It can be appreciated by visual inspection of the graphical outputs that with increasing bridge length individual layers behave more rigidly, as they consist of a smaller number of blocks, and consequently of wider individual blocks. This effect is important for the stability of the immediate roof area (measurement points 1 and 2) where failure of entire roof slabs is permissible kinematically.

3.5.2 The influence of joint length on rock mass deformations

In Figure 3-9 the vertical deformations in the rock mass away from the immediate roof zone and all the way up to the surface (measurement points 3, 4, 5) are plotted as a function of mean joint trace length as well as *b/L* ratio. Inspection of Figure 3-9 reveals that the influence of the *b/L* ratio on rock mass deformation above the immediate roof zone is not significant as can be appreciated from the flat curves in this plot. The parameter which seems to be the most significant for rock mass deformation above the immediate roof zone seems to be the simulated mean joint trace length. With increasing length of through going joints (Gross and Eyal, 2007), more vertical shear deformation is possible in the rock mass in comparison to mechanically layered rock masses where the vertical extent of cross joints is bounded by bedding plane boundaries. This study clearly indicated that mechanically layered rock masses

exhibit less vertical deformation, and consequently less surface settlements, then a rock mass with long through-going joints, even when the total number of blocks in the rock mass is equal.

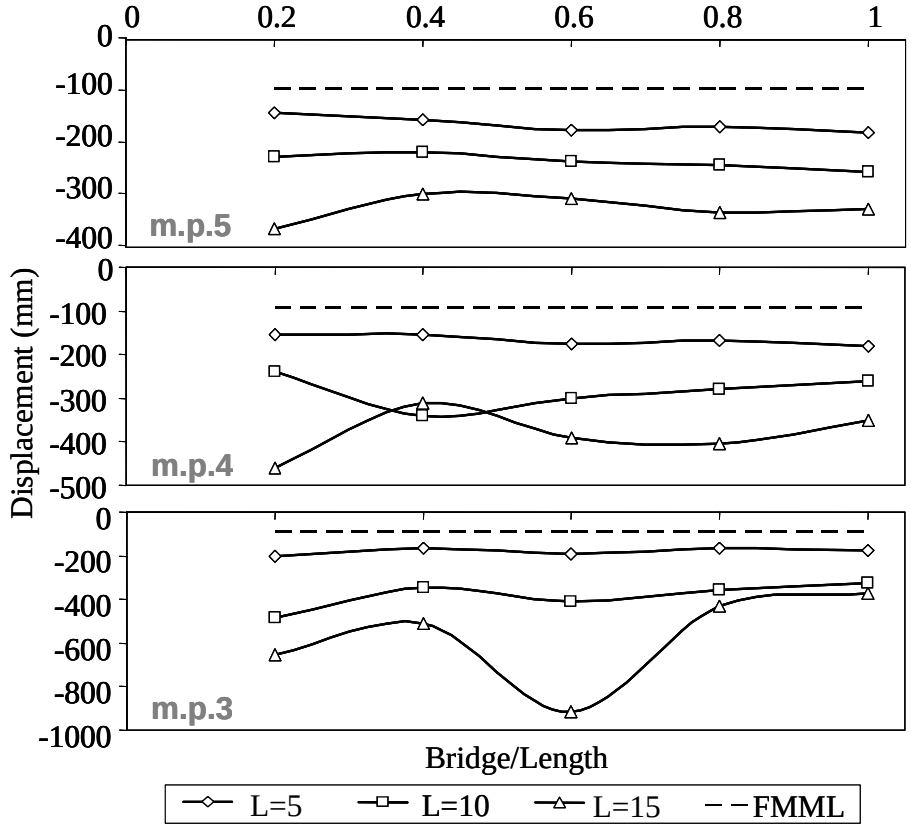

Figure 3-9. Final vertical displacement (after 5 sec) above immediate roof as a function of joint bridge / joint length. FMML results shown for reference.

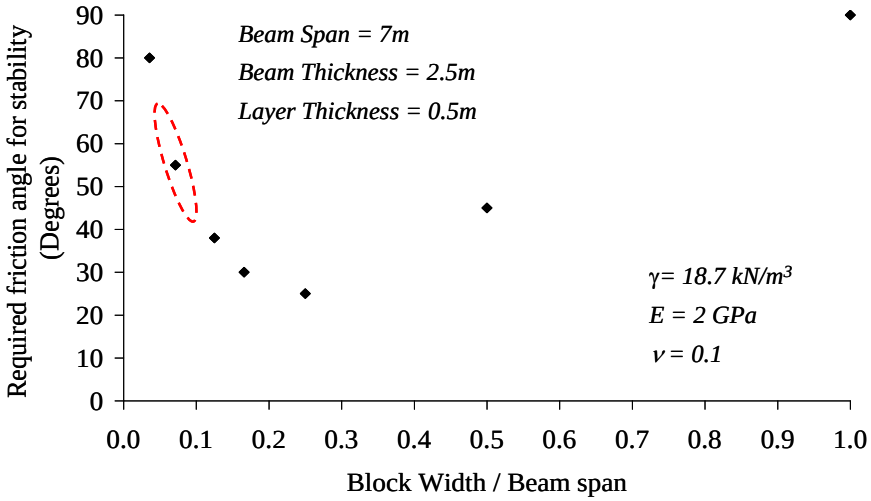

Figure 3-10. Friction angle required for stability vs. ratio between block width and beam (opening) span (after Hatzor and Benary, 1998). Dashed ellipse shows the relevant block widths / opening ratio for the simulations performed in this study.

CHAPTER 4 - DYNAMIC SLIDING OF A TETRAHEDRAL WEDGE

4.1 Introduction

A new analytical solution for dynamic block sliding in three dimensions is developed in this chapter based on the original static limit equilibrium formulation presented by Goodman and Shi (1985) for both single face and double faces sliding (Figure 4-1). The chapter begins with dynamic single plane sliding problems where the block is free to slide in any direction along the sliding plane (see Figure 4-1a), and proceeds with the dynamic sliding of a tetrahedral wedge where the sliding direction is controlled by the orientation of the two boundary planes (see Figure 4-1b). In the case of single plane sliding the results are compared with classical Newmark's solution. In the case of a tetrahedral wedge both the analytical and numerical results are compared with dynamic shaking table experiments performed on a physical model of a tetrahedral wedge.

Application of any analytical solution, sophisticated or accurate as it may be, is only valid for a single, rigid block for which the failure mode must be assumed in advance. In order to study the dynamic behavior of a rock slope consisting of multiple and interacting rigid blocks however, a discrete numerical approach such as the numerical discontinuous deformation analysis (DDA) method (Shi and Goodman, 1989a; Shi, 1993) is required. However, an accurate performance of the numerical method does require rigorous validation studies using comparisons to analytical solutions and/or physical models of simplified problem geometries. In this chapter the 3D-DDA version (Shi, 2001) is validated using the results obtained from shaking table experiments.

In the current formulation of both 2D as well as 3D DDA codes a constant friction angle value is assumed for the sliding interface regardless of the intensity or duration of shaking. In the course of shaking table experiments friction degradation of the sliding interface is clearly observed during dynamic shaking, leading to block "run out" after a certain number of cycles of motion. To obtain a quantitative measure of the amount of dynamic frictional degradation the shaking table results are used in conjunction with the new analytical solution so that the velocity dependency of the sliding interface could be determined.

As the time dependency of friction resistance is important here, the classic Coulomb-Mohr friction criterion has been modified to incorporate "rate-and-state" effects using a double-direct-shear apparatus (Marone et al., 1992) or more recently a conventional (single) direct shear system for rock interfaces (Biran et al., 2010). In this chapter, the single direct

shear apparatus is used to determine the dynamic friction law for the studied interfaces.

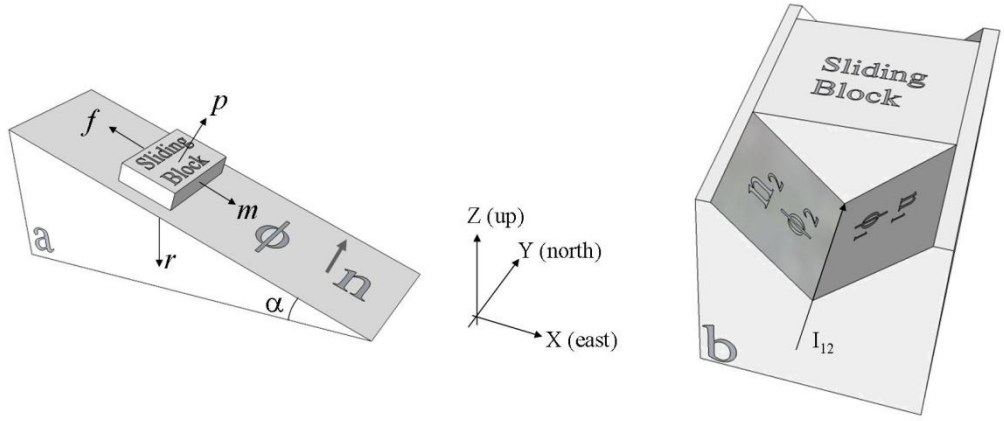

Figure 4-1. Schematic illustration of single (a) and double (b) face sliding in 3D.

4.2 Analytical solution for dynamic sliding of wedge

4.2.1 Limit Equilibrium Equations

The static limit equilibrium equations formulated for each time step are discussed in this section for both single and double face sliding. Naturally, the expected failure mode must be known in advance to formulate the equilibrium equations. In the cases discussed here the resultant forces are applied to the centroid of the sliding block, slightly in contrast to the physical reality where the input motion is applied to the foundation upon which the block rests. Algorithms for MATLAB functions for both single and double face sliding are given in appendix 1.

Single Face Sliding

A typical three dimensional model of a block on an incline is illustrated in Figure 4-1a. The dip and dip direction angles are, $\alpha = 20^{\circ}$ and $\beta = 90^{\circ}$, respectively. Although it is a simple 2D problem, the model is plotted as if it were 3D to demonstrate the advantages of the new solution. For this purpose, a Cartesian coordinate system (*x,y,z*) is defined where *X* is horizontal and points to east, *Y* is horizontal and points to north, and *Z* is vertical and points upward. The normal vector of the inclined plane is: $\hat{n} = [n_x, n_y, n_z]$, where:

$$\begin{aligned} n_x &= \sin(\alpha)\sin(\beta) \\ n_y &= \sin(\alpha)\cos(\beta) \\ n_z &= \cos(\alpha) \end{aligned} \tag{4.1}$$

The force equations presented below refer to a block with a unit mass. Hence, these

equations can be discussed in terms of accelerations. The resultant force vector that acts on the system at each time-step is $\bar{r} = [r_x, r_y, r_z]$. The driving force vector that acts on the block ($\overline{m}$), namely the projection of the resultant force vector on the sliding plane, at each time step is:

$$\overline{m} = (\hat{n} \times \bar{r}) \times \hat{n} \tag{4.2}$$

The normal force vector that acts on the block at each time step is:

$$\bar{p} = (\hat{n} \cdot \bar{r}) \hat{n} \tag{4.3}$$

At the beginning of a time step, if the velocity of the block is zero then the resisting force vector due to the interface friction angle ϕ is:

$$\bar{f} = \begin{cases} -\tan(\phi)|\bar{p}|\hat{m} & , \quad \tan(\phi)|\bar{p}| < |\overline{m}| \\ -\overline{m} & , \quad else \end{cases} \tag{4.4}$$

where $\hat{m}$ is a unit vector in direction $\overline{m}$.

If, at the beginning of a time step the velocity of the block is not zero, then:

$$\bar{f} = -\tan(\phi)|\bar{p}|\hat{v} \tag{4.5}$$

where $\hat{v}$ is the direction of the velocity vector.

In an unpublished report, Shi (1999) refers only to the case of a block subjected to gravitational load, where the block velocity and the driving force have always the same sign. The same is true for the original equations published in the block theory text by Goodman and Shi (1985). However, in the case of dynamic loading the driving force can momentarily be opposite to the block velocity.

Double Face Sliding

Double face sliding, or as often referred to as the wedge analysis, is a classic problem in rock mechanics that has been studied by many authors (e.g. Londe et al., 1969; Goodman, 1976; Hoek and Bray, 1981; Hatzor and Goodman, 1997). A typical model of a three dimensional wedge is shown in Figure 4-1b. The normal to plane 1 is $\hat{n}_1 = [n_{x1}, n_{y1}, n_{z1}]$ and the normal to plane 2 is $\hat{n}_2 = [n_{x2}, n_{y2}, n_{z2}]$. Consider a block sliding simultaneously on two boundary planes along their line of intersection $\hat{I}_{12}$, where:

$$\hat{I}_{12} = \hat{n}_1 \times \hat{n}_2 \tag{4.6}$$

The resultant force in each time step is as before $\bar{r} = [r_x, r_y, r_z]$, and the driving force in each time step is:

$$\bar{m} = (\bar{r} \cdot \hat{I}_{12})\hat{I}_{12} \tag{4.7}$$

The normal force acting on plane 1 in each time step is $\bar{p} = [p_x, p_y, p_z]$, and the normal force acting on plane 2 in each time step is $\bar{q} = [q_x, q_y, q_z]$, where:

$$\bar{p} = ((\bar{r} \times \hat{n}_2) \cdot \hat{I}_{12})\hat{n}_1 \tag{4.8}$$

$$\bar{q} = ((\bar{r} \times \hat{n}_1) \cdot \hat{I}_{12})\hat{n}_2 \tag{4.9}$$

As in the case of single face sliding, the direction of the resisting force ($\bar{f}$) depends upon the direction of the velocity of the block. Therefore, as before, in each time step:

$$\bar{f} = \begin{cases} -\left(\tan(\phi_1)|\bar{p}| + \tan(\phi_2)|\bar{q}|\right)\hat{m} & , \ \bar{V} = 0 \quad and \quad \left(\tan(\phi_1)|\bar{p}| + \tan(\phi_2)|\bar{q}|\right) < |\bar{m}| \\ -\bar{m} & , \ \bar{V} = 0 \quad and \quad \left(\tan(\phi_1)|\bar{p}| + \tan(\phi_2)|\bar{q}|\right) \geq |\bar{m}| \\ -\left(\tan(\phi_1)|\bar{p}| + \tan(\phi_2)|\bar{q}|\right)\hat{v} & , \ \bar{V} \neq 0 \end{cases} \tag{4.10}$$

4.2.2 Dynamic equations of motion

The sliding force, namely the block acceleration during each time step, is $\bar{s} = [s_x \ s_y \ s_z]$ and is calculated as the force balance between the driving and the frictional resisting forces:

$$\bar{s} = \bar{m} + \bar{f} \tag{4.11}$$

The block velocity and displacement vectors are $\bar{V} = [V_x, V_y, V_z]$ and $\bar{D} = [D_x, D_y, D_z]$, respectively. At $t = 0$, the velocity and displacement are zero. The average acceleration for time step i is:

$$\bar{S}_i = \frac{1}{2}(\bar{s}_{i-1} + \bar{s}_i) \tag{4.12}$$

The velocity for time step i is therefore:

$$\bar{V}_i = \bar{V}_{i-1} + \bar{S}_i \Delta t \tag{4.13}$$

It follows that the displacement for time step i is:

$$\bar{D}_i = \bar{D}_{i-1} + \bar{V}_{i-1}\Delta t + \frac{1}{2}\bar{S}_i \Delta t^2 \tag{4.14}$$

Due to the discrete nature of the suggested algorithm, sensitivity analyses were performed to discover the maximum value of the time increment for the trapezoidal integration method without compromising accuracy. It is found that the results are sensitive to the time interval size as long as the friction angle is greater than the slope inclination, and the time increment can not be larger than 0.001 sec to obtain accurate results.

4.3 Comparison to classical Newmark's approach

The validity of the new developed 3D analytical formulation presented above is tested using the classical 2D Newmark's solution for the dynamics of a block on an inclined plane. The typical Newmark's solution requires condition statements and is solved using a numerical time step algorithm as discussed for example by Kamai and Hatzor (2008). The Newmark's procedure is related here to as the 'exact solution', in order to distinguish between the existing approach and the analytical solution proposed here. Figure 4-2A shows a comparison between Newmark, analytical, and 3D-DDA solutions for a plane with dip and dip direction of $\alpha = 20^o$ and $\beta = 90^o$, respectively, and friction angle of $\phi = 30^o$. A sinusoidal input motion in the horizontal X axis is used for dynamic loading, so the resultant input acceleration vector is $\bar{r} = [r_x\ r_y\ r_z] = [0.5\sin(10t)\ 0\ -1]g$. The accumulated displacements are calculated up to 10 cycles ($t_f = 2\pi$ sec). The input horizontal acceleration is plotted as a shaded line and the acceleration values are shown on the right hand-side axis. The theoretical mechanical properties as well as the numerical parameters for the 3D DDA simulations are listed in Table 4-1. For both the Newmark's and analytical solutions the numerical integration is calculated using a time increment of $\Delta t = 0.001$ sec. For the 3D approaches (the new analytical solution and 3D-DDA), the calculated displacement vector is normalized to one dimension along the sliding direction.

An excellent agreement is obtained between the new analytical and Newmark's solutions throughout the first two cycles of motion. There is a small discrepancy at the end of the second cycle which depends on the numerical procedures and will decrease whenever the time increment decreases. The relative error of the new analytical solution and 3D-DDA method with respect to the existing Newmark's solution is shown in the lower panel of Figure 4-2A, where the relative error is defined as:

$$E_{rel} = \frac{\left|D_{Newmark} - D_{compared\,solution}\right|}{\left|D_{Newmark}\right|} \cdot 100\% \tag{4.15}$$

The relative errors for both the analytical solution and 3D DDA are found to be less the 3% in the final position.

4.4 Comparison between 3D analytical and numerical approaches

The agreement between the 3D analytical and 2D Newmark's solutions has been established in the previous section; therefore the analytical solution will be used next as a reference for numerical dynamic simulations with 3D-DDA. Figure 4-2B presents a comparison between the analytical and 3D DDA solutions for the case of a block on an inclined plane (see Figure 4-1a) subjected to two components of a dynamic, horizontal, input loading function. The resultant input acceleration vector is $\bar{r} = [r_x\ r_y\ r_z] = [0.5\sin(10t)\ 0.5\sin(5t)\ -1]g$, and the friction angle is again $\phi = 30^o$. The two components of the input horizontal acceleration are plotted as shaded lines and the acceleration values are shown on the right- hand side axis. Note that the relative error presented in the lower panel is now with respect to the 3D analytical solution, defined as:

$$E_{rel} = \frac{\left|D_{analytic} - D_{3D\ DDA}\right|}{\left|D_{analytic}\right|} \cdot 100\% \tag{4.16}$$

The relative error in the final position in this simulation is approximately 8%.

The comparisons thus far were between analytical and numerical solutions, both of which incorporate significant assumptions regarding material behavior and boundary conditions. In the next section physical model test results will be used to study the applicability of both the numerical and analytical approaches employed above.

Table 4-1. Numerical parameters for 3D-DDA forward modeling simulation.

	Block on an incline model	Tetrahedral Wedge
Mechanical Properties:		
Elastic Modulus, MPa	20	200000
Poisson's Ratio	0.25	0.25
Density, kg/m^3	1000	1700
Friction angle, Degrees	30	30 ÷ 36
Numerical Parameters:		
Dynamic control parameter	1	1
Number of time steps	628	8000
Time interval, Sec	0.01	0.005
Assumed max. disp. Ratio, m	0.01	0.01
Penalty stiffness, MN/m	10	10000 ÷ 20000

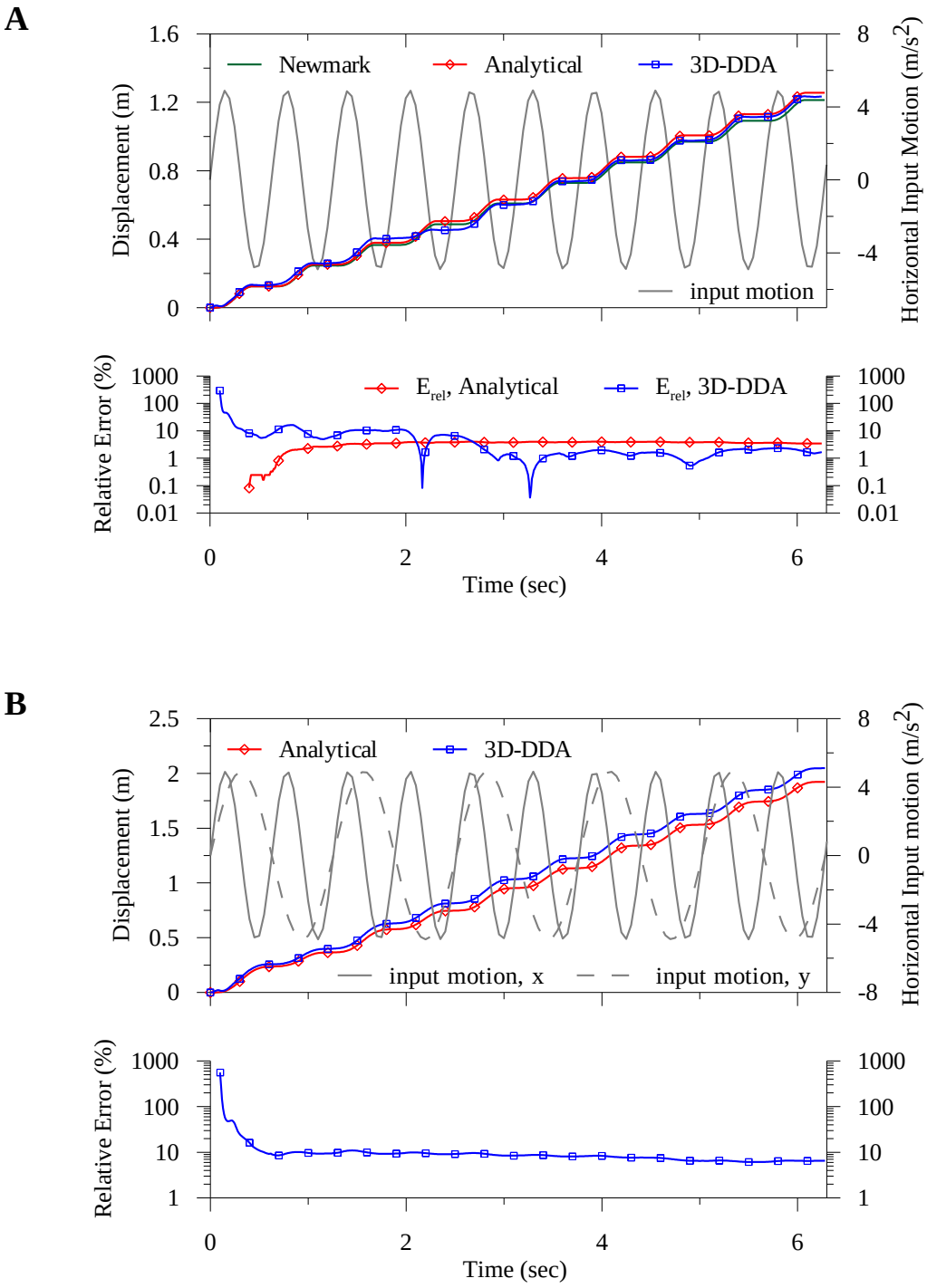

Figure 4-2. Dynamic block displacement for single face sliding: A) Comparison between 2D Newmark solution, the new 3D analytical solution, and 3D-DDA for horizontal input acceleration parallel to the X axis. Relative error with respect to Newmark solution is plotted in the lower panel, B) Comparison between the new 3D analytical solution and 3D-DDA for 2D horizontal input acceleration parallel to X and Y axes simultaneously. The relative error is calculated with respect to the new 3D analytical solution.

4.5 Experimental determination of interface friction

Both numerical and analytical solutions require a definition of the peak and residual friction angles of the interface along which dynamic sliding takes place. Peak and residual friction angles for the tested interface were determined experimentally using direct shear tests performed at Ben-Gurion University rock mechanics laboratory. Special cubic concrete samples were cast specifically for that purpose using B30 Portland cement with water/cement ratio of 0.3 in PVC moulds. First the peak friction angle for very low normal stress was determined using simple tilt tests by slowly increasing the inclination of the base block and measuring the inclination when sliding initiated. Next direct shear tests were performed on the same cubic concrete blocks utilizing the hydraulic, closed-loop, servo-controlled system at the Ben-Gurion University rock mechanics laboratory (Figure 2-4) where both axial and shear pistons could be operated using either load or displacement outputs as the control variable. Two types of direct shear tests were performed: 1) Velocity stepping under a constant normal stress of 5 MPa and variable slip rates of 10, 0.5, 1, and 3 μm/sec, to explore velocity-dependency of the concrete interface, and 2) Five-segment direct shear tests under constant normal stress values of 1, 2, 3, 4, and 5 MPa and constant displacement rates of 0.002, 0.020, and 0.100 mm/sec, to determine steady state friction coefficient as a function of sliding velocity.

4.6 Dynamic shaking table experiments

A 13 cm width by 20 cm long concrete block was attached to the horizontally driven shaking table of the Earthquake Simulation Laboratory at U. C. Berkeley (Figure 2-3). The base block was set at an inclination of 28^{o} below horizontal to the North such that the inclinations of the two boundary planes were 51.4/065.8 and 51.4/295.2, arranged symmetrically about the shaking axis (Figure 4-3). The concrete blocks for the dynamic shaking table experiments were made using the same preparation procedures described above with a static interface friction angle of 36^{o}. A well fitted tetrahedral concrete block was placed on the wedge-shaped slab such that under gravitational pull only the block remained stationary. Note that after few shaking experiments, the concrete interface was rubbed and consequently the static interface friction angle was decreased.

Two 1-D linear accelerometers were fixed to the table and to the fixed block. Two displacement transducers measured the relative displacement of the sliding block and shaking table (see Figure 4-3). A third linear accelerometer was attached to the upper sliding block in

order to measure the natural frequency of the experimental construction. A discrete Fast Fourier Transform (FFT) performed on the free vibration signal due to a hammer blow in parallel to the shaking table axis yielded a natural frequency for the experimental set up in the range of 70 - 90 Hz.

Sinusoidal input motions with frequencies ranging between 2 to 5 Hz and amplitudes of 0.20 - 0.28 g were induced by the function generator. The sinusoidal input motions were ramped up linearly for 5 seconds, followed by full amplitude for several tens of seconds, to the time that the block completed 10 cm of sliding, the largest traveling distance allowed by the system configuration.

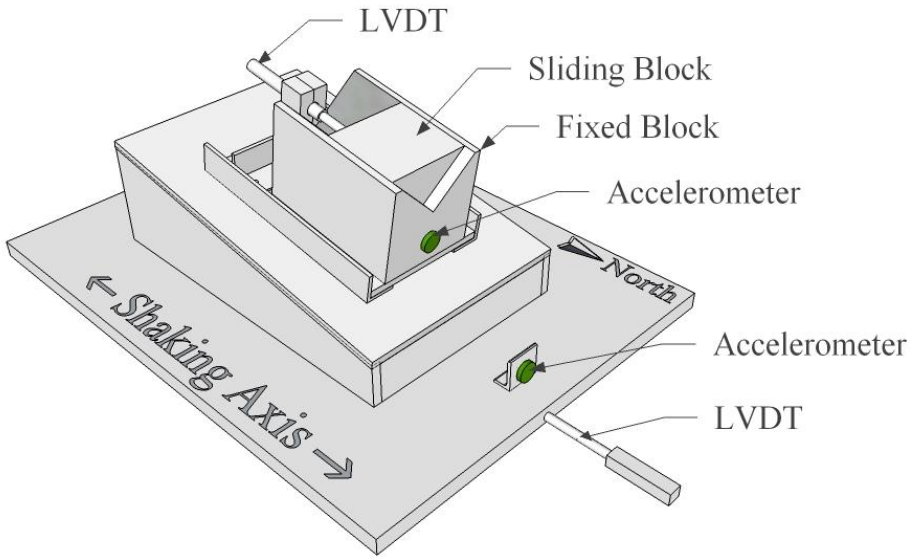

Figure 4-3. Layout of the tetrahedral wedge assembly mounted on the UCB shaking table facility.

4.7 Results

4.7.1. Determination of friction angle from tilt and direct shear experiments

The average friction angle obtained from 20 tilt-tests for the concrete interface was 36^o, with standard deviation of 3^o. Another 20 tilt-tests after gentle polishing of the concrete interface yielded average friction angle of 32^o with standard deviation of 2^o.

A representative result of a direct shear velocity stepping test is presented in Figure 4-4 where the response of the interface to changes in the imposed sliding velocity is shown. Induced velocity decrease from 10 to 0.5 μm/sec results in immediate reduction in friction

coefficient followed by steady state sliding at a higher friction coefficient, whereas induced velocity increases from 0.5 to 1 μm/sec and from 1 to 3 μm/sec both result in immediate increase in friction coefficient followed by steady state sliding at a lower friction coefficient, suggesting that the tested interface exhibits a "velocity weakening" behavior. The immediate response to the change in the induced sliding velocity before steady state sliding is attained (open circles in Figure 4-4) is known as the direct velocity effect and is proportional to the *A* parameter of the rate and state friction law as explained in section 2.1.3 (see also Scholz, 1998).

Towards the end of each constant velocity sliding segment frictional resistance seems to apparently increase (see Figure 4-4). There are no observations of the actual interface condition during each sliding segment, but visual inspections of the tested interface at the end of each complete test reveal that the interface was damaged during the entire testing. The slight increase in shear strength detected at the end of each steady state sliding segment is therefore attributed to the apparent increase in the contact area due to interface fragmentation.

The induced velocity ratio between two segments (V_2/V_1) allows to evaluate the rate and state *A* and *B* coefficients (Dieterich, 1979; Ruina, 1983). Assuming steady-state sliding is reached in each segment, the values of $A \approx 0.027$ and $B \approx 0.035$ are obtained for the tested concrete interface.

To determine classical Coulomb-Mohr failure envelopes for different sliding rates, the normal stress was changed while steady state sliding was maintained, as shown for example in Figure 4-5A for sliding velocity of 0.020 mm/sec. The resulting Coulomb-Mohr failure envelopes for three different values of sliding velocity are plotted in Figure 4-5B, where highly linear trends are indicated. It is found that the Coulomb - Mohr friction coefficient clearly exhibits velocity dependence, decreasing in the tested interface from $\mu = 0.6547$ (corresponding to $\phi = 33^o$) to $\mu = 0.6220$ (corresponding to $\phi = 32^o$) as sliding velocity increases from 0.002 to 0.100 mm/sec, suggesting again a "velocity weakening" interface as inferred from the series of velocity stepping tests discussed above.

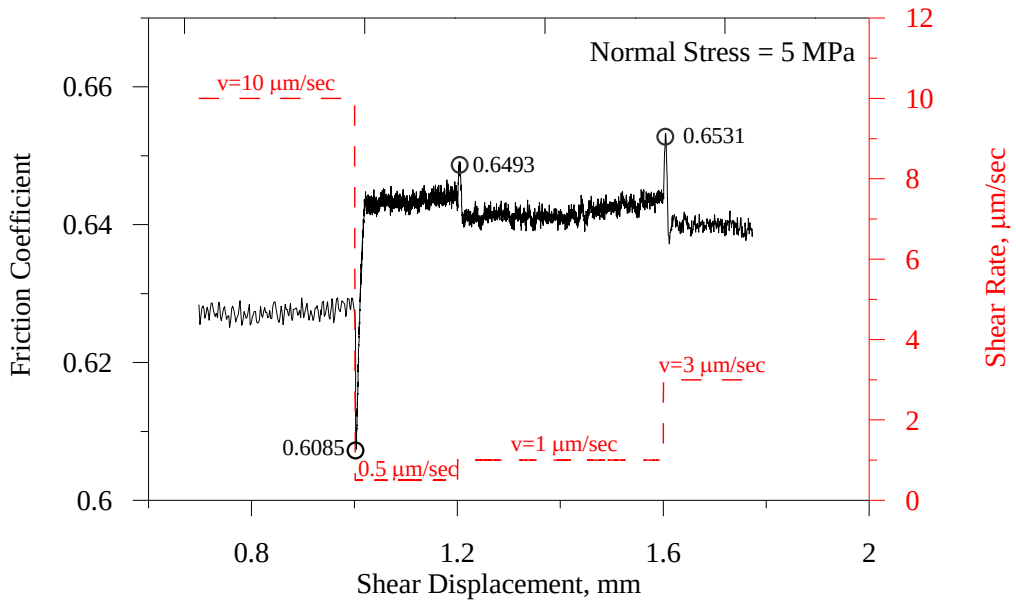

Figure 4-4. Representative result of a velocity stepping tests performed with the direct shear system shown in Figure 2-4.

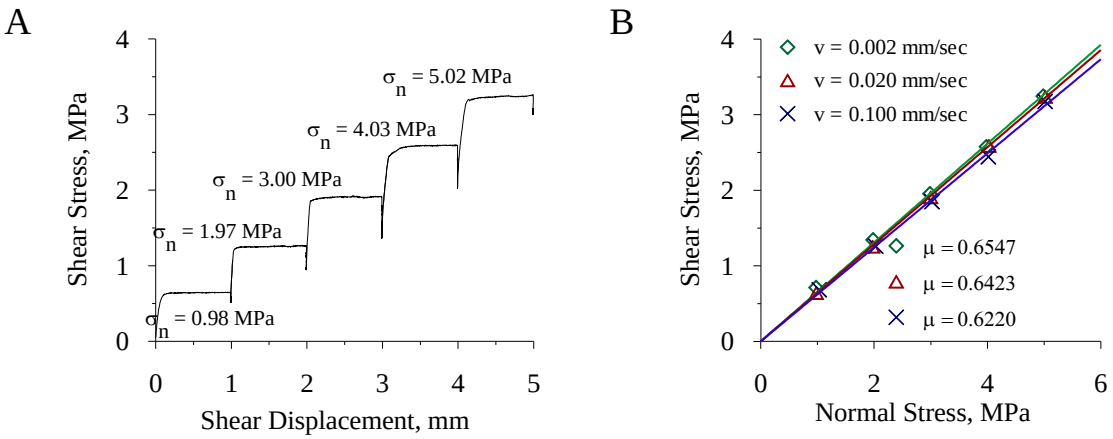

Figure 4-5. Direct shear test results for determination of the effect of imposed sliding velocity on Coulomb-Mohr friction: A) Representative example of a complete stress-displacement history for a typical five-segment test (v = 0.020 mm/sec), B) Coulomb-Mohr envelopes for the tested concrete interface obtained with three values of shear rate.

4.7.2. Comparison between dynamic shaking table experiments and 3D-DDA results

Comparison between 3D-DDA and shaking table experiments for the dynamic sliding of a tetrahedral wedge is shown in Figure 4-6. The input motion is sinusoidal at a frequency of 2Hz and amplitude of 0.21 *g* corresponding to shaking table amplitude of 13 mm. Two different input motion modes are modeled: 1) "loading mode" - application of the dynamic force at the centre of mass of the (upper) sliding block, 2) "displacement mode" - application of the dynamic displacement into the (lower) foundation block. To allow meaningful analysis in "displacement mode" high input frequencies were filtered out using a low pass Butterworth

filter of 2.5 Hz. To preserve similarity between the original loading functions used in DDA simulations, the same filtering procedure was performed also for analysis in "loading mode".

Both DDA simulations are carried out using a constant value of friction angle on both planes, namely $\phi_1 = \phi_2 = \phi$. To determine the appropriate input friction angle for 3D-DDA simulations, the displacement data for the wedge was used in the following manner. Consider Figure 4-7A where actual block displacement initiates at a time $t_i = 8.8$ sec after the beginning of the experiment. The corresponding level of input acceleration of 0.14 g at t_i is used to recover the limiting value of friction angle for the two boundary planes of the wedge by inversion, using a pseudo-static limit equilibrium analysis for a tetrahedral wedge. The limiting friction angle value thus obtained is $\phi = 30^o$. This limiting value of the friction angle is confirmed by the new 3D analytical solution discussed above for the given wedge geometry and level of induced shaking.

It is found that in both input motion modes the computed displacement results are highly sensitive to the choice of the numerical penalty stiffness parameter, while the defined friction angle play only a secondary role (see Figure 4-6). In "loading mode" accurate results are obtained when the numerical penalty stiffness value is increased up a maximum value of 40 GN/m (Figure 4-7), beyond which the numerical solution does not converge. The upper limit penalty value for the "displacement mode" is found to be 20 GN/m, beyond which the numerical solution again does not converge. Otherwise no significant differences are found between the two different modes of input motion. A small discrepancy is detected between the measured and computed block response at the beginning of the simulation in both loading modes (Figure 4-7). This behavior is attributed to the high sensitivity of the numerical code to the choice of the numerical penalty stiffness value. The numerical control parameters for 3D-DDA simulations are listed in Table 4-1. Note that the model dimensions are in mm and in contrast to a previous study (Tsesarsky et al., 2005) no kinetic damping is applied here.

3D-DDA in its current stage of development assumes a constant friction angle value for the sliding interfaces. The shaking table test results, however, suggest that the dynamic displacement of the physical block departs from classical Newark's type displacement and actually exhibits "run out" behavior (see Figure 4-8) that can only be explained by means of frictional degradation as a function of the number of cycles of motion. In the next section the new analytical solution is employed to determine quantitatively, by back analysis, the rate and amount of friction degradation during dynamic slip.

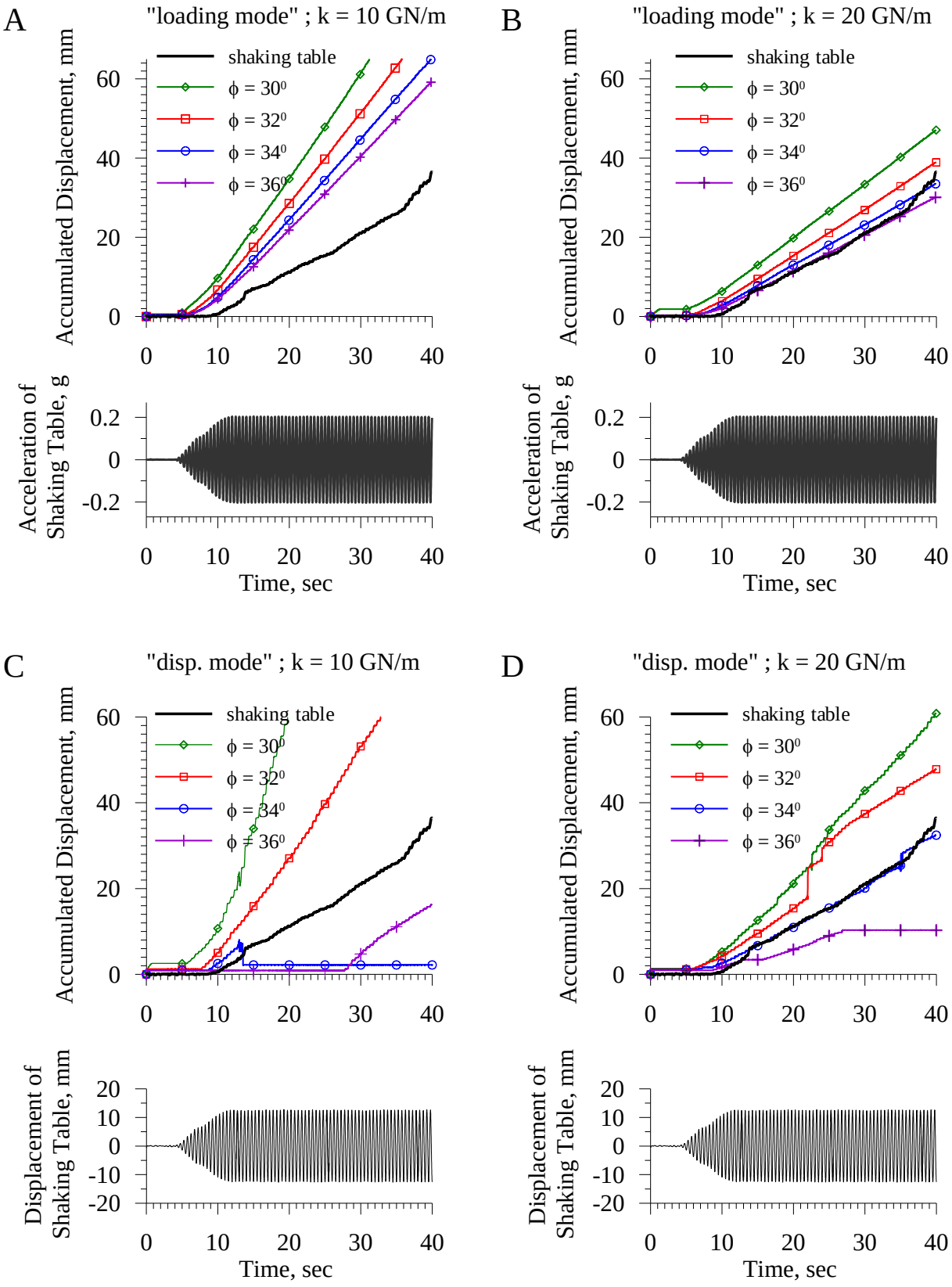

Figure 4-6. 3D-DDA validation using shaking table experiment results for the dynamic sliding of a wedge, for two different numerical penalty stiffness values (k = 10 and 20 GN/m) and two different input motion ("loading" and "displacement") modes.

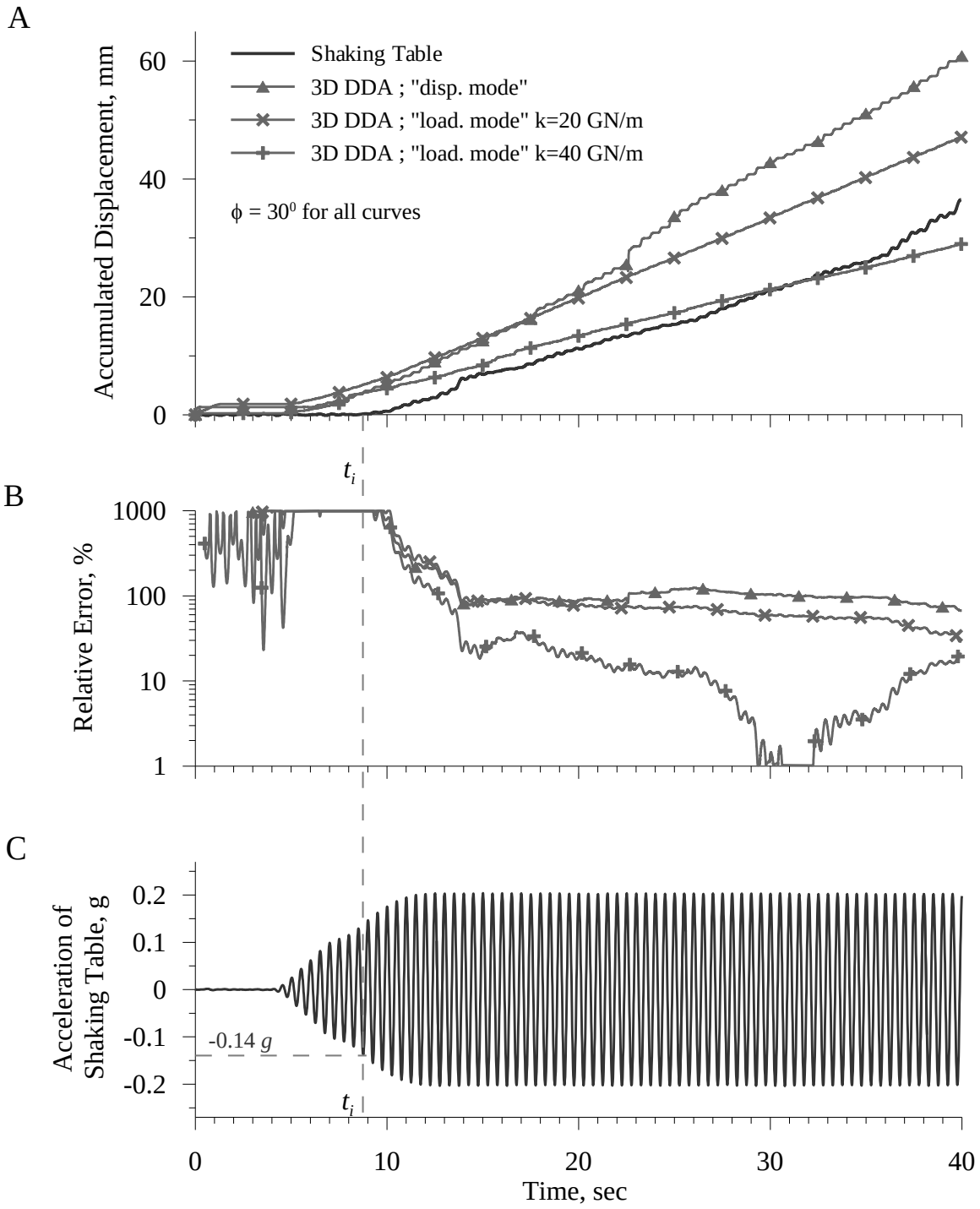

Figure 4-7. Determination of input friction angle for 3D-DDA simulations: A) Comparison between 3D-DDA and shaking table results; B) Relative error between computed and measured data; C) 2 Hz sinusoidal input motion with amplitude of 0.21 *g* as recorded on the shaking table. A limiting friction angle of 30º is defined, corresponding to horizontal yield acceleration of 0.14 *g*.

4.7.3. Dynamic friction degradation

Two representative tests exhibiting "run-out" behavior are shown in Figure 4-8. The obtained time dependent sliding function can be approximated by three linear segments. To reproduce the physical test results analytically three different values of friction angle are therefore introduced into the new analytical solution to best fit the experimental data, recalling that the friction angles for the two boundary planes of the wedge are assumed equal. The "best fit" friction angles thus obtained for each sliding segment along with maximum shaking table acceleration are listed in Table 4-2 for eight different experiments. Inspection of the results shown in Table 4-2 reveals the striking similarity between back calculated friction angle values obtained in all tests. The consistency in the back analyzed friction angle values is demonstrated in Figure 4-9 where results from two representative sets of experiments are plotted.

The number of loading cycles required for onset of friction degradation is found to be between 30 and 50 in the current experimental set up, with input acceleration amplitudes of 0.21 - 0.22 *g* and input frequency of 2 Hz. As would be expected, the number of loading cycles required for onset of friction degradation is reduced with increasing acceleration amplitude.

The average sliding velocity for the best fit friction coefficients obtained for all tests is plotted in Figure 4-10. Clearly the tested interface exhibits velocity weakening behavior that can explain the observed "run out" of the wedge as shown in Figure 4-8. Interestingly, the friction coefficients obtained from slow direct shear tests plot on the same linear trend obtained from back analysis of shaking table experiments (Figure 4-10).

Table 4-2. List of back calculated tests.

Test	ϕ_1, *degrees*	ϕ_2, *degrees*	ϕ_3, *degrees*	*Max. Shaking Table Acceleration, g*
CU	29.5	29	27	0.206
CV	29.5	29	27	0.206
CW	29.4	28.7	26	0.208
CY	29.3	28.8	27	0.205
CZ1	29.9	29.4	27	0.219
CZ2	29.9	29.4	27.2	0.217
CZ3	29.6	29.3	27.1	0.218
CZ4	29.8	29.5	28.5	0.217

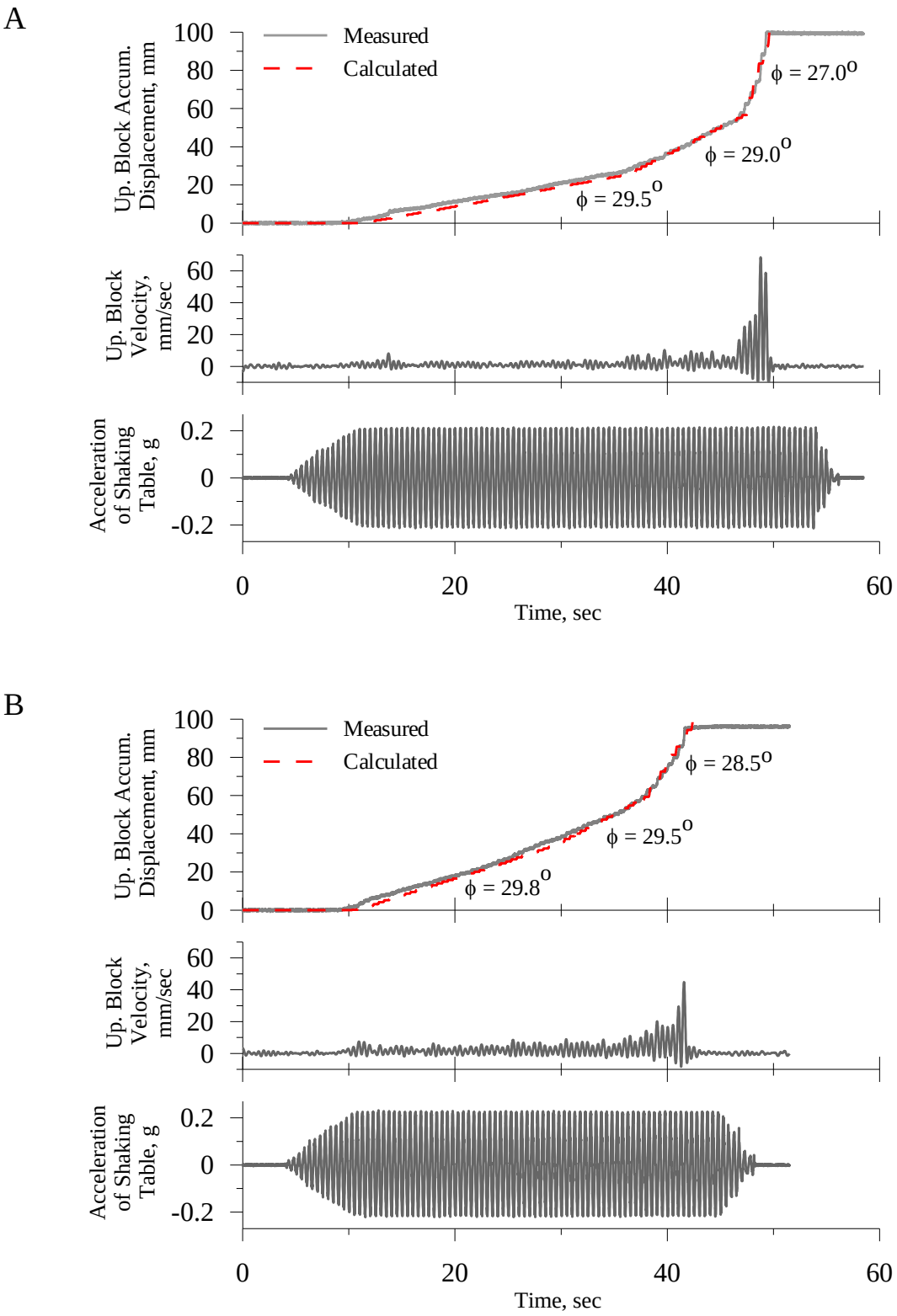

Figure 4-8. Best fit between analytical solution and shaking table results allowing for friction degradation due to dynamic slip. Input frequency 2Hz, input acceleration amplitude: A) 0.21 g; B) 0.22 g.

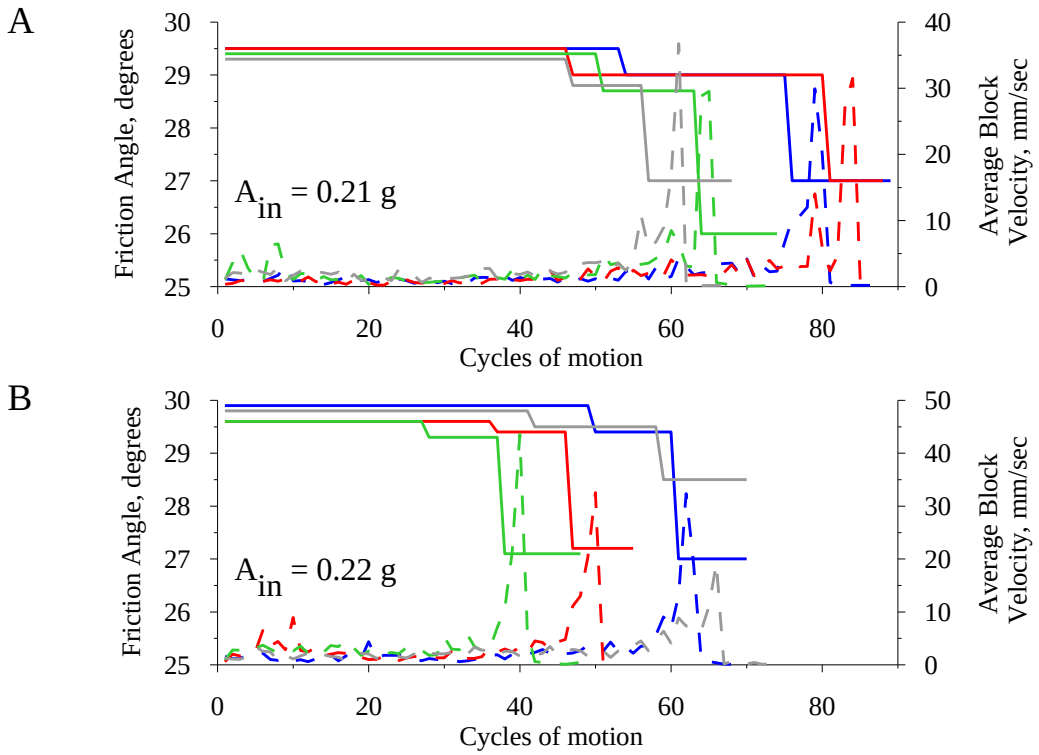

Figure 4-9. Friction angle (solid lines) and average sliding velocity (dashed lines) as a function of shaking cycles with sinusoidal input frequency of 2 Hz and induced amplitude of 0.21 *g* (A) and 0.22 *g* (B), obtained from back analysis of 8 shaking table experiments.

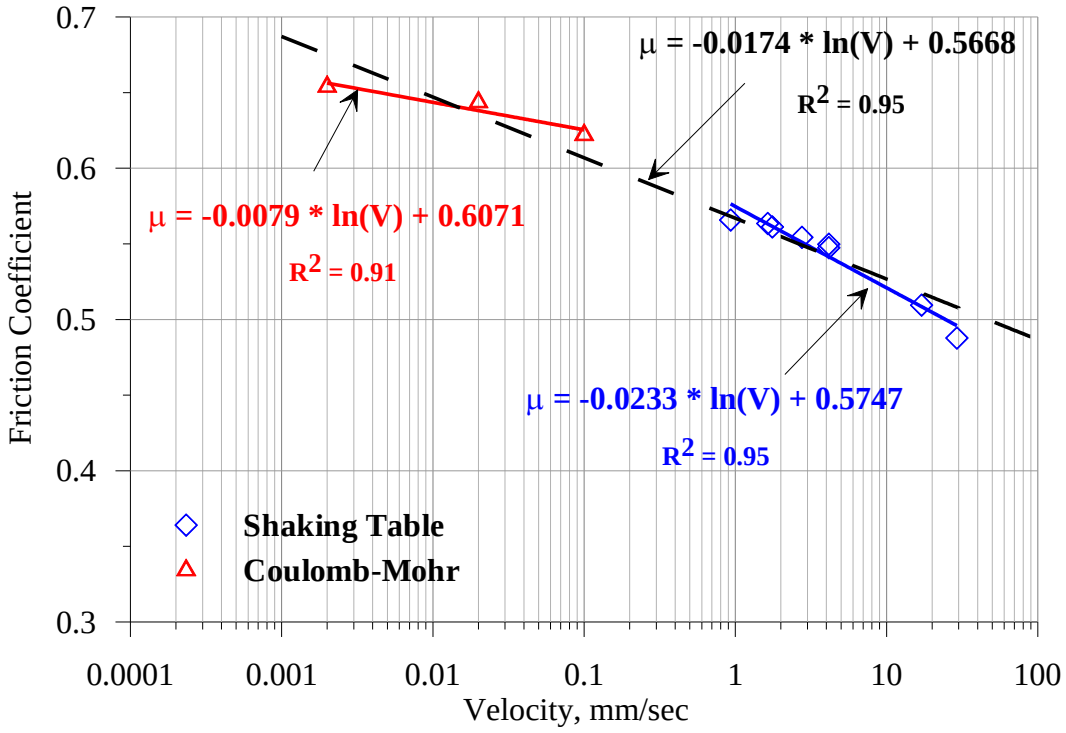

Figure 4-10. Friction coefficient as a function of sliding velocity: open triangles - data obtained from direct shear tests, open diamonds - back calculated results from shaking table experiments.

4.8 Discussion

This study presents the first attempt known to the author to perform fully dynamic analysis with 3D-DDA and to check the accuracy of the method using both analytical solutions and physical test results. One of the strengths of the DDA method is that the mode of failure of the block system is a result of the analysis and not an assumption, especially regarding 3D analysis. The numerical results obtained with 3D-DDA are found to be in good agreement with both methods of validation, with the numerical results being slightly on the conservative side when compared to results of shaking table experiments. It is found that dynamic application of 3D-DDA is highly sensitive to the numerical penalty (contact spring stiffness); this sensitivity may lead to observed sliding initiation in 3D-DDA that precede the actual arrival time of the theoretical yield acceleration. On the other hand, it is found that the friction angle in 3D-DDA play only a secondary role when computing dynamic sliding, as obtained from comparison between Figure 4-6A and B.

Two methods of dynamic input are studied, referred to here as "loading" and "displacement" modes, both of which provide similar results within the accuracy resolution sought in this study. The "loading mode" is found to be less sensitive to the numerical penalty and consequently results obtained with this input method are smoother. As in 2D-DDA, the most accurate results with 3D-DDA are obtained with a highest value of numerical penalty, beyond which the numerical solution does not converge. The optimum value of this numerical control parameter is case specific and depends, to a great extent, on the elastic modulus and mass of the modeled block (see Table 4-1).

In the 3D-DDA codes used in this research a constant value of frictions angle is assumed for a given interface, whereas physical test results suggest that frictional degradation does occur with increasing numbers of shaking cycles culminating, ultimately, in wedge "run out" (see Figure 4-8). The actual amount of friction loss is determined here by best-fitting the shaking table results with the new 3D analytical solution.

With a low amplitude sinusoidal input it is found that several tens of seconds of cyclic motion are required to induce run out. The number of cycles required for block run out is found to be inversely proportional to the amplitude of shaking. Few tens of cycles of motion at a frequency range of 2-5 Hz may represent a relatively large earthquake in moment magnitude (M_w) range of 7 - 8. Kanamori and Brodsky (2004) show that the source duration of such an earthquake may reach up to 100 sec.

Velocity stepping and classic direct shear tests indicate that the tested concrete interface exhibits velocity weakening. Velocity weakening is also inferred from the results of the dynamic shaking table experiments where friction degradation culminated in block run out. Interestingly, friction degradation leading to block run out is obtained here under dry conditions, in contrast to recent studies on the run out of large landslides (Vardoulakis, 2000; Veveakis et al., 2007; Goren and Aharonov, 2009). Note that there are three fundamental differences between the direct shear and shaking table tests: 1) in direct shear tests the velocity of the sliding block is induced by the hydraulic servo-control command whereas in shaking table tests the velocity of the block is in response to the induced displacement of the underlying table, 2) in direct shear tests friction values are obtained from "steady state" sliding whereas steady state conditions are never obtained in the shaking table experiments and friction values are inferred by inversion. While for the case of shaking table tests it cannot be determined if friction degradation is a result or a cause of the sliding velocity of the tested wedge, it is clear that interface friction and sliding velocity are interrelated, and 3) the normal stresses in the direct shear test are in the order of 10^6 Pa, where in the shaken block the normal stresses are three orders of magnitude lower. However, since the concrete interface is very smooth, it is assumed that the friction angles obtained by the direct shear tests represent dynamic response of the tested concrete interface under slow velocities.

The friction coefficients obtained from slow direct shear tests and rapid shaking table experiments are plotted in Figure 4-10 on a semi logarithmic scale, with velocity spanning 5 orders of magnitude. The results are quite striking. First, the slow rate direct shear tests as well as the fast rate shaking table experiments each plot on a linear trend, and second, both sets of tests can be fitted on the same linear trend with a very good linear regression coefficient of $R^2 = 0.95$, confirming in essence the rate and state law of seismology (Dieterich, 1979; Ruina, 1983) but with different testing methodology (the rate and state law was originally formulated from analysis of velocity stepping tests; see section 2.1.3). The (A - B) term of the Dieterich-Ruina "rate and state" variable friction law can be recovered from results of the direct shear tests where steady - state sliding was clearly reached (see Figure 4-10). The obtained A - B value thus obtained (-0.0079) is one order of magnitude lower than a single value obtained from the entire suite of test data (-0.0174). Therefore, extrapolation from slow rate direct shear test data to fast rates proves in accurate, and from engineering stands point - un-conservative.

The classical static or pseudo-static analyses, as well as Newmark's solution, do not take into account friction degradation along rock discontinuities, and therefore cannot predict run-

out phenomena in rock slopes in response to ground vibrations emanating from strong earthquakes of long duration. It is concluded that velocity-dependent friction across rock discontinuities should be integrated into dynamic rock slope analysis, either analytical or numerical, to obtain more realistic results when strong ground motions of long duration are considered.

CHAPTER 5: A THERMALLY INDUCED "RATCHET" MODEL FOR ROCK SLOPE STABILITY

5.1 Introduction

Considering daily and seasonal temperature influences, many researchers have detected extremely slow, creep-like, slope displacements due to cyclic temperature changes in long-term monitoring surveys (Hatzor, 2003; Watson et al., 2004; Gunzburger et al., 2005; Gischig et al., 2011a; Gischig et al., 2011b; Mufundirwa et al., 2011). Incidentally, the motivation for some of these monitoring surveys was the preservation of cultural heritage sites around the world, for example in Slovakia (Vicko et al., 2009), Japan (Greif et al., 2006), and Israel (Hatzor et al., 2002).

Gunzburger et al. (2005), in their investigation of the Rochers de Valabres slope in the Southern Alps of France, using a high-precision geodetic monitoring system and numerical modeling, found that daily surface temperature oscillations played an important preparatory role in rock fall events. They showed that daily temperature fluctuations may be responsible for generating irreversible displacements on some fractures. Nevertheless, they concluded that the monitoring of preparatory factors was not sufficient to predict eminent slope collapse. Mufundirwa et al. (2011) monitored natural rock slope deformation due to thermal stresses across fractures in a chert rock mass. By a new method to minimize displacement proportional to temperature, they recovered the recognized displacement that has been related to reversible thermo-elastic response of the rock mass and the sensor and concluded that thermal fatigue predominantly caused permanent fracture deformations. Gischig et al. (2011a; 2011b) demonstrated how thermo-mechanical effects can drive rock slope deformation at greater depths below the annual thermally active layer. They found that deformation and progressive rock slope failure can be driven solely by thermo-mechanical forcing.

Various researchers have suggested that daily and seasonal temperature fluctuations may generate thermally induced stresses sufficiently high to propagate pre-existing cracks in the rock mass (e.g. Vargas Jr et al., 2009). Furthermore, although the seasonal temperature front penetrates only a few meters into the rock mass, it may still have significant mechanical consequences in terms of displacements or stress changes far from the rock surface, especially for rock slopes with critically stressed discontinuities (Gunzburger et al., 2005; Gischig et al., 2011a; Gischig et al., 2011b).

Watson et al. (2004) utilized data obtained from an extensive instrumentation monitoring program at the Checkerboard Creek in British Columbia, Canada. Their monitoring record indicates a persistent annual displacement cycle that matches the thermal cycle, as recorded near the bedrock surface. Their numerical analysis indicates that the permanent displacement occurs along steeply dipping discontinuities which often intersect in the rock mass to form wedges.

In this chapter a thermally induced wedging mechanism is suggested to explain how cyclic thermal oscillations induce intermittent expansion and contraction of the tension crack, causing seasonal translation of rock blocks. A new evidence for thermally induced block displacements is presented using both thermal and displacement data from a monitored rock block in the West face of Masada Mountain, Israel, along with re-visited and re-analyzed monitoring data from the East face of Masada. A removable block at the Eastern slope of the mountain, referred to as Block 1, is used as a case study, where an accumulated displacement of 200 mm took place during the geological history. The theoretical possibility of obtaining thermally induced block displacements in Masada rock slopes is explored, given the measured seasonal temperature amplitude and the mechanical and physical properties of the rock mass. Then, the seismic loading in Masada rock slopes is addressed, based on the assumed seismicity of the region and the measured topographic site effect in the mountain. The two loading mechanisms, thermal vs. seismic, that drive rock slope deformation are discussed and their relative significance in rock slope deterioration are compared.

5.1.1 Geological setting of Masada

Masada Mountain, a world heritage site, is an uplifted, lozenge -shaped horst within the band of normal faults that comprise the western margins of the Dead Sea rift (DSR) valley (see Figure 5-1A). The rock mass consists of bedded dolomites and limestones, inclined 5˚ up to 20˚ to the East (J1), and is intensely fractured by two orthogonal, sub-vertical, and very persistent joint sets, striking roughly parallel and normal to the long axis of the mountain, namely J2 set strikes NNE and J3 strikes ESE. In a regional study in the western margins of the Dead Sea pull-apart, Sagy et al. (2003) suggest that these two dominating regional joint set patterns were developed during a single tectonic phase. The mean joint spacing at Masada varies from few decimeters the West face up to 5-10 m in the East face of the mountain (Hatzor, 2003).

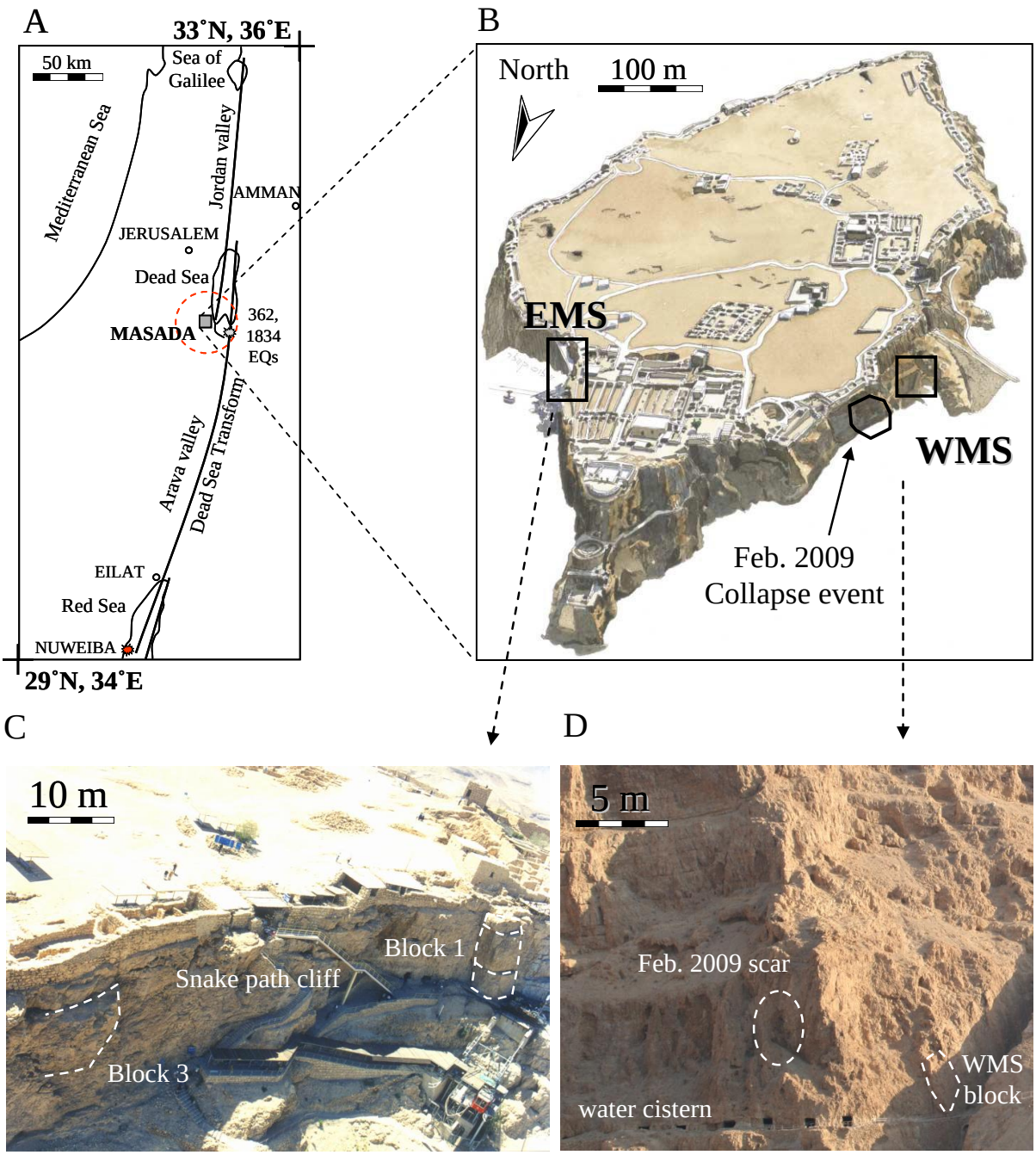

Figure 5-1. Location maps. A) the Masada Mountain in the Western margins of the Dead Sea rift valley. B) location of the monitoring stations (EMS = East Masada Station; WMS = West Masada Station), C) monitored blocks in the "Snake Path" cliff (EMS), D) collapsed block at WMS.

5.1.2 Climatic setting and observed weather induced collapse in Masada

Climatically, Masada Mountain is located in the Eastern part of the Judean Desert, an arid zone with mean annual rainfall values of 35 mm/year, and average seasonal minimal and maximal temperatures of 12.7 ˚C and 39.7 ˚C, respectively, as reported by the Israeli Meteorological Service (2011) for the period of 1983 - 2000. Within the framework of the

MASAL research project (Meteorological Observation and Assimilation of the Atmosphere on Long term, Dead Sea, Israel) (Corsmeier, 2006; Schmitz, 2009) a fully equipped meteorological station, located 300 meters from the West slope of Masada, has been recording the amount of precipitation, temperature, and wind velocity since 2006.

During the night of February 10, 2009, a heavy rain storm struck the West face of Masada Mountain. Consequently, a sizeable rock fall was triggered, the debris of which damaged the ancient path leading to the water cisterns that were excavated by the Romans some 2000 years ago for water storage in the Western cliffs of the mountain. The February 10, 2009, slope failure (Figure 5-1D) was the motivation for installing a monitoring system in the West slope of the mountain in July 2009, for investigation of the dynamic response of rock blocks to thermal fluctuations.

5.2 West and East monitoring stations in Masada

5.2.1 West Masada Station (WMS)

In order to measure with high precision the rock block response to daily and seasonal environmental oscillations, a monitoring system was installed in June 2009 on a single block separated from the West cliff of Masada by two intersecting joint sets (Figure 5-2). The monitoring system, manufactured by SIM STRUMENTI SNC (2009), consisting of four joint meters, temperature, and relative humidity transducers, has been collecting output data at an acquisition rate of 12 samples per day (24 Hr) since July, 2009. The layout of the joint meters as installed in the Masada West Station (WMS) is presented in Figure 5-2. The joint meters (model DS810) are 50-mm-range Potentiometers with 0.1% linearity full scale and measurement accuracy of +/- 0.02 mm. The thermal expansion coefficient of the joint meter is 1.5 X 10^{-6} ˚C^{-1} and its calibrated operating range is -30 ˚ to +100 ˚C. The static end of each joint meter, containing the sensor, was anchored to the massive rock body while the free end was attached to the removable block. The joint meters (WJM 1-4) were installed perpendicular to the joint trace as follows: WJM 1 was installed on an open joint belonging to joint set J2, WJM 2 and WJM 3 were installed across a joint belonging to joint set J3. In order to account for thermal effects on the monitoring system a dummy joint meter (WJM 4) was installed directly on the intact, continuous rock face. Details for joints openings and joint meters configuration are given in Table 5-1.

An air temperature is measured with a temperature sensor (model WE710) with precision of 0.25 ˚C and a range of -25 ˚C to 105 ˚C. A relative humidity is measured with a

Humidity meter (model WE720) under an operating temperature range of -20 ˚C to +80 ˚C. The measurement devices were connected to two separate data acquisition systems (Model ML-4CH).

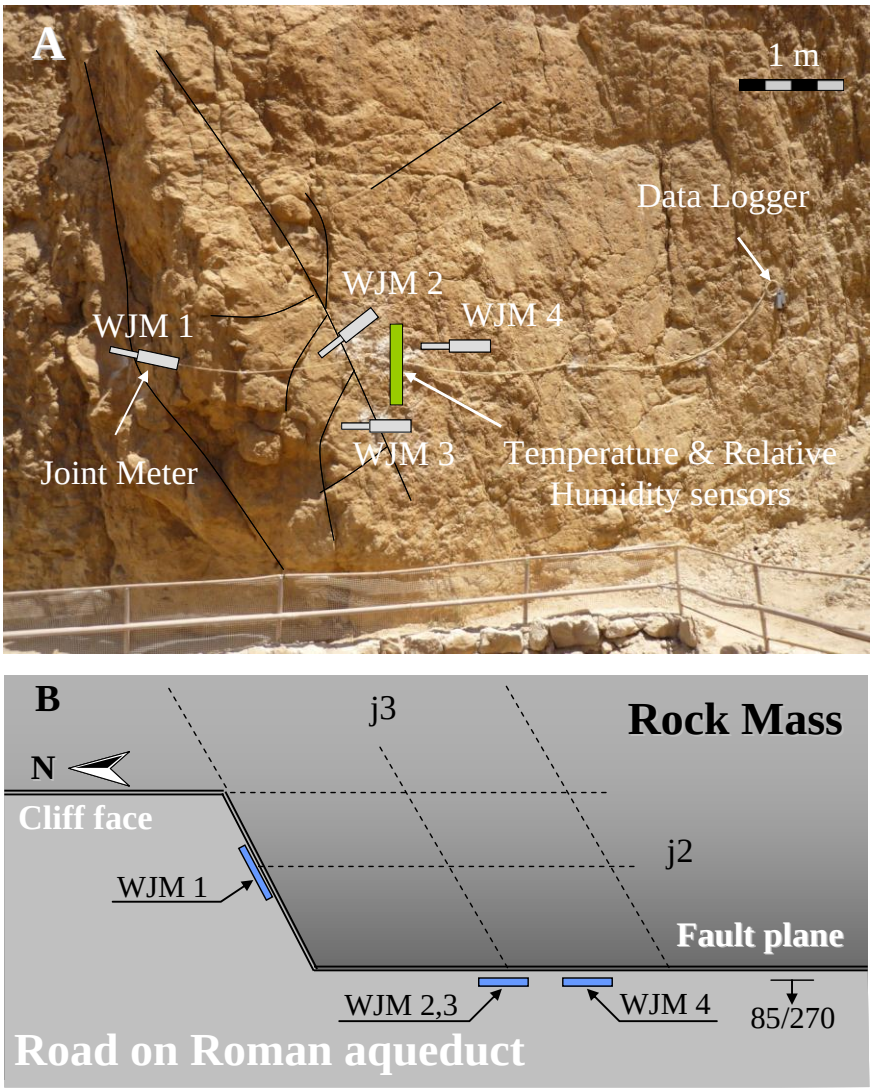

Figure 5-2. The environmental monitoring system at WMS, A) Face view of monitored block (WJM = West Joint Meter), and B) plan view schematically illustrating the rock mass structure and joint meter position. For joint and joint meter data see Table 5-1.

Table 5-1. Joint Meters (JM) configuration in the Masada West slope monitoring station (WMS)

JM	Distance between bolts (cm)	Joint opening (cm)	JM orientation (dip/dip direction)
1	26.4	10 - 12	2/250
2	25.2	3 – 12	33/340
3	25.0	1	3/180
4	24.8	-	0/000

5.2.2 East Masada Station (EMS)

In a previous rock slope stability study Hatzor (2003) monitored time dependent displacements of rock blocks (referred to as "Block 1" and "Block3" in that study) embedded in the “Snake Path” cliff at the East face of Masada Mountain, using sensitive joint meters. Block 1 is a prismatic block resting on a gently (19 ˚) Easterly-dipping bedding plane (J1), separated from the cliff by two sub-vertical, orthogonal tension cracks (J2 and J3) (see Figure 5-3A). The block height is 15 m and its width is about 7 m. Four joint meters (EJM 1-4) were mounted across the two tension cracks that separate Block 1 from the "Snake Path" cliff, along with temperature transducer (T1) that was mounted inside an open tension crack at the back of the block (see Figure 5-3A). Block 3, located at the south part of the cliff (see Figure 5-1C), separated from the rock mass by a single tension crack, also rests on an Easterly dipped bedding plane. Two joint meters (EJM 10 and 11) were installed across the tension crack (J3) at the back of the block. Another temperature transducer (T2) was installed within an open fracture nearby the block (Figure 5-3B).

Time – dependent displacements of Block 1 and Block 3 and the air temperature near the blocks were recorded from January 14 to June 30, 1998. Cable bolt support was then installed in Block 1 to anchor the block to the cliff, in connection with a slope reinforcement campaign that was conducted at the East slope at that time, while Block 3 remained un-reinforced to this day. The East slope monitoring system of Hatzor (2003) is referred to here as "Masada East Station" (EMS).

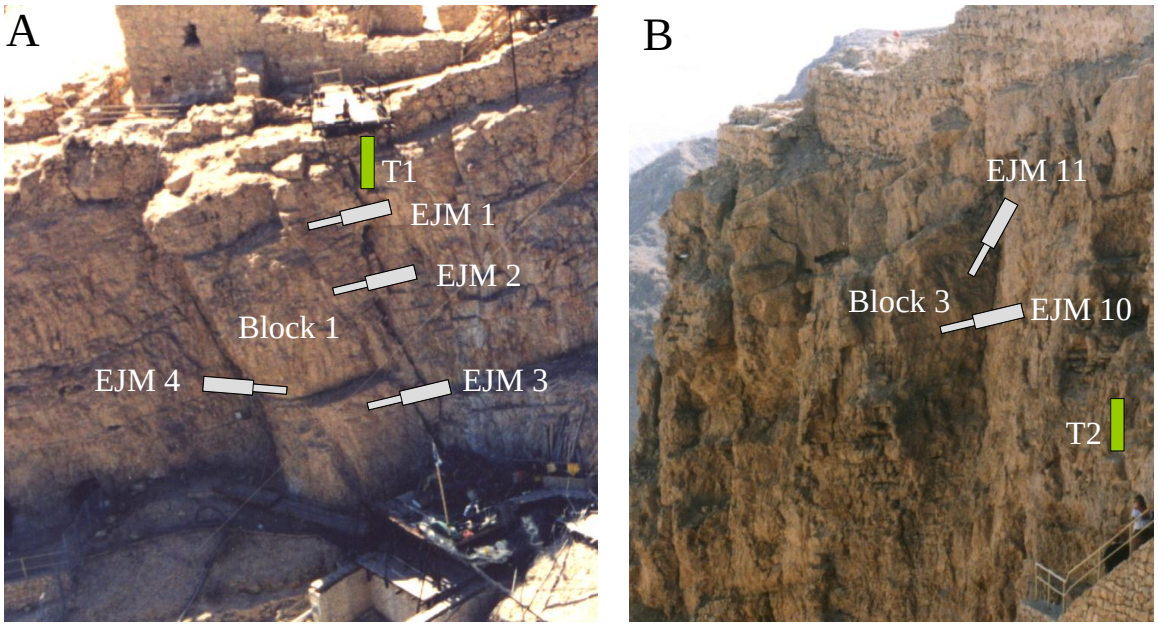

Figure 5-3. Monitoring system layout at EMS (after Hatzor, 2003) where EJM stands for East Joint Meter: Block 1 (A), Block 3 (B).

5.3 Temperature and displacement monitoring results

The outputs of WMS instruments are plotted in Figure 5-4 for a period of 25 months (July 2009- August 2011). The joint meters were wired such that joint opening returns positive output. The raw data recorded at two hours intervals is shown in Figure 5-4A (gray lines), smoothed by daily moving average (solid lines). As clearly indicated in Figure 5-4A the "dummy" joint meter installed on intact bed-rock (WJM 4) shows a nearly static response while the rock joints (WJM 1-3) exhibit relatively large fluctuations over time. To study the relationship between air temperature and joint displacement, moving averages with a 30 days time window has been performed on the original raw data obtained from WJM 1-4. The results are plotted in Figure 5-4B as a function of time, and an inverse relationship between cooling and joint closure is clearly indicated. Note that the output of dummy transducer (WJM4) exhibits a certain amount of drift, believed to be an artifact as the transducer is mounted on solid rock.

Results obtained from Blocks 1 and 3 at EMS are shown in Figure 5-5 for a period of 5.5 months between January 14 and June 30, 1998. Since the data acquisition rate in EMS was not constant, Figure 5-5 represents the joint meter displacement (in mm) and air temperature as a function of time, using daily average data. The joint meters output was zeroed such that the beginning of the monitoring period was set at the origin for each joint meter output. Accumulated joint closure related to increasing air temperature was recorded at all joint meters during the monitoring period at the East slope. Although a full annual period was not recorded in EMS during the monitoring survey at 1998, it is clearly evident that inter-seasonal fluctuations in air temperature directly affect joint opening and closing, as inferred from the joint meters output.

In contrast to the short monitoring period in East slope, the recent monitoring data from the West slope provide information about long-term joint displacement and air temperature and the relationship between them. The annual amplitude of both air temperature and joint displacement can be inferred from the results. The annual amplitude recorded by WJM 2 is 0.14 mm while the annual air temperature amplitude is 9.1 ˚C.

Monitoring data presented in Figure 5-4 and Figure 5-5 from WMS and EMS suggest that joint opening and closure are strongly correlated with air cooling and heating. This correlation implies that contraction and expansion of the rock on both sides of the crack manifests in joint opening or closure, as clearly indicated by joint meter outputs. The relationship between joint opening and air temperature for one annual cycle in WMS is

plotted in Figure 5-6 using monthly averaging of the raw data. The annual cycle for WJM 1 begins on May, 2010 and ends on May 2011; the annual cycle for WJM 2, 3, and 4 is from August 2009 to August 2010. To demonstrate the time dependent path of the monitored joint displacement, the beginning and end of the annual cycle are denoted in the figure.

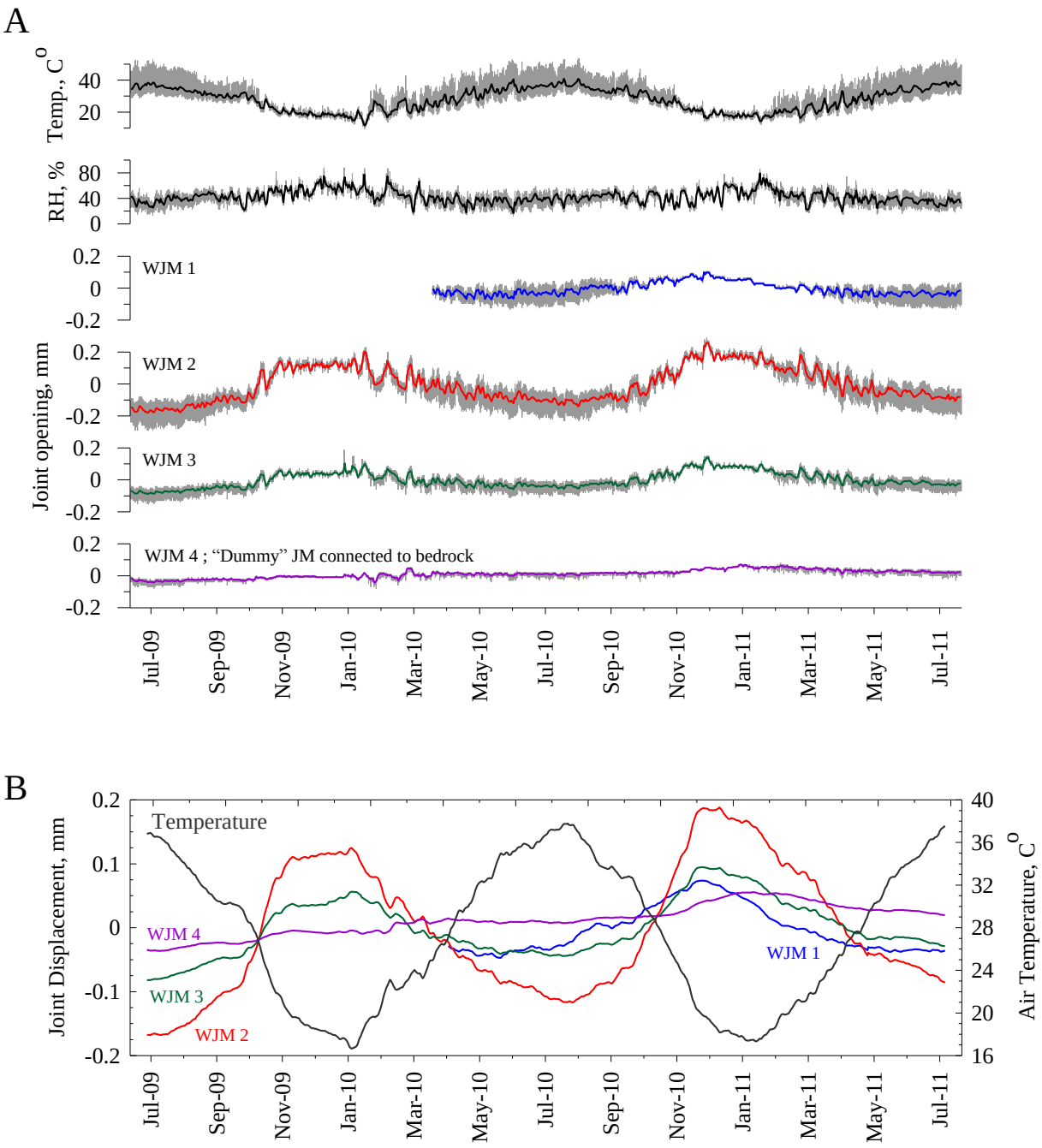

Figure 5-4. WMS output from July 2009 to August 2011 (Joint opening is positive). A) original data sampled every 2 hours (gray lines) smoothed by daily moving average (solid), B) temperature and joint displacement vs. time using monthly moving average.

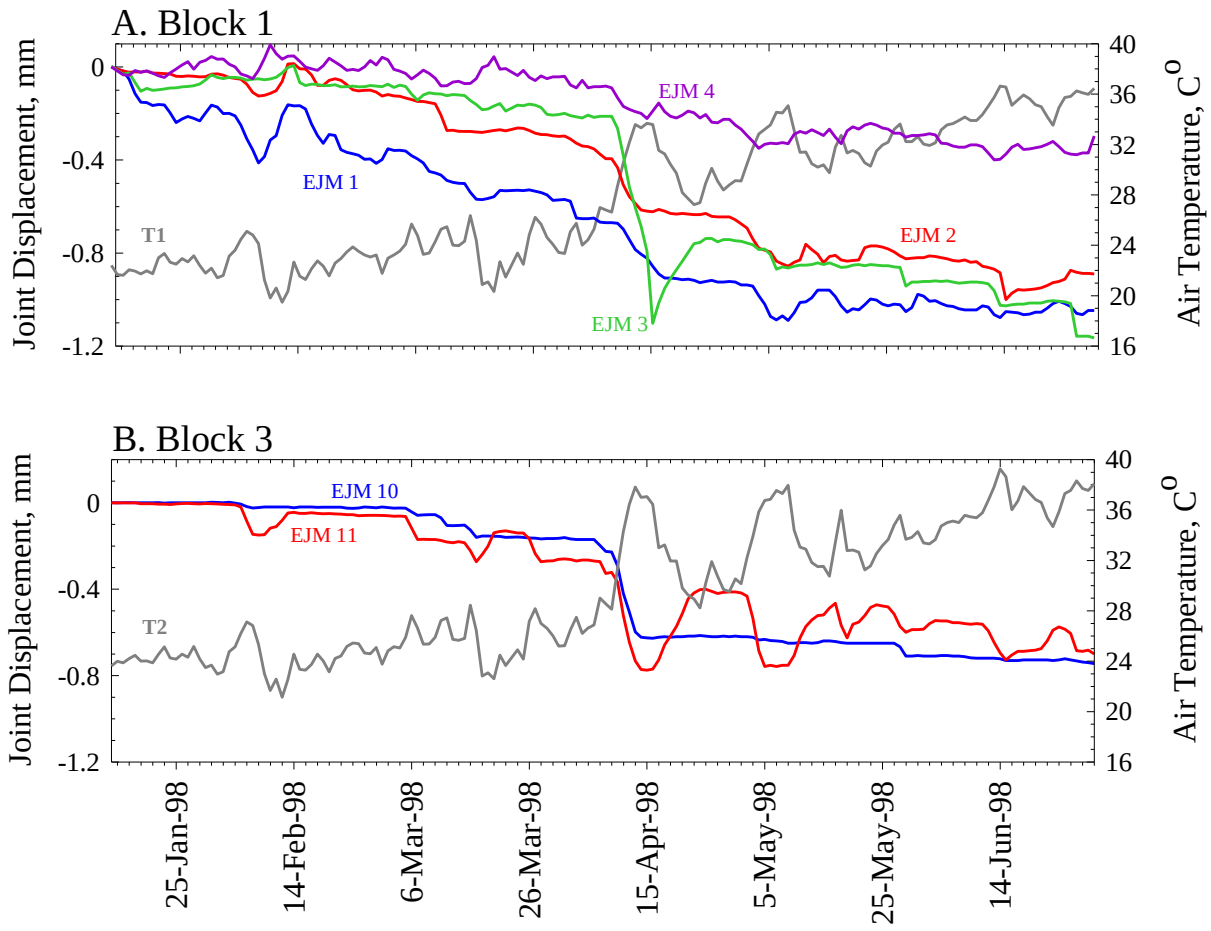

Figure 5-5**.** EMS output data from January 14 to June 30, 1998 (Joint opening is positive, T = temperature transducer).

An inverse relationship between joint opening and air temperature is obtained with a relatively high linear correlation for WJM 2 and 3 (Figure 5-6), implying that the dominant factor affecting joint displacement is thermo-elastic, the majority of which is recovered by the end of an annual loading cycle (Figure 5-6A). To address the drift of WJM 4, and assuming that all joint meters have a similar drift, the output of WJM 4 is subtracted from the output of WJM 1, 2, and 3 and the results are shown in Figure 5-6B. The subtraction of WJM 4 data suggests that at the end of an annual cycle the monitored joints do not exhibit any permanent deformation.

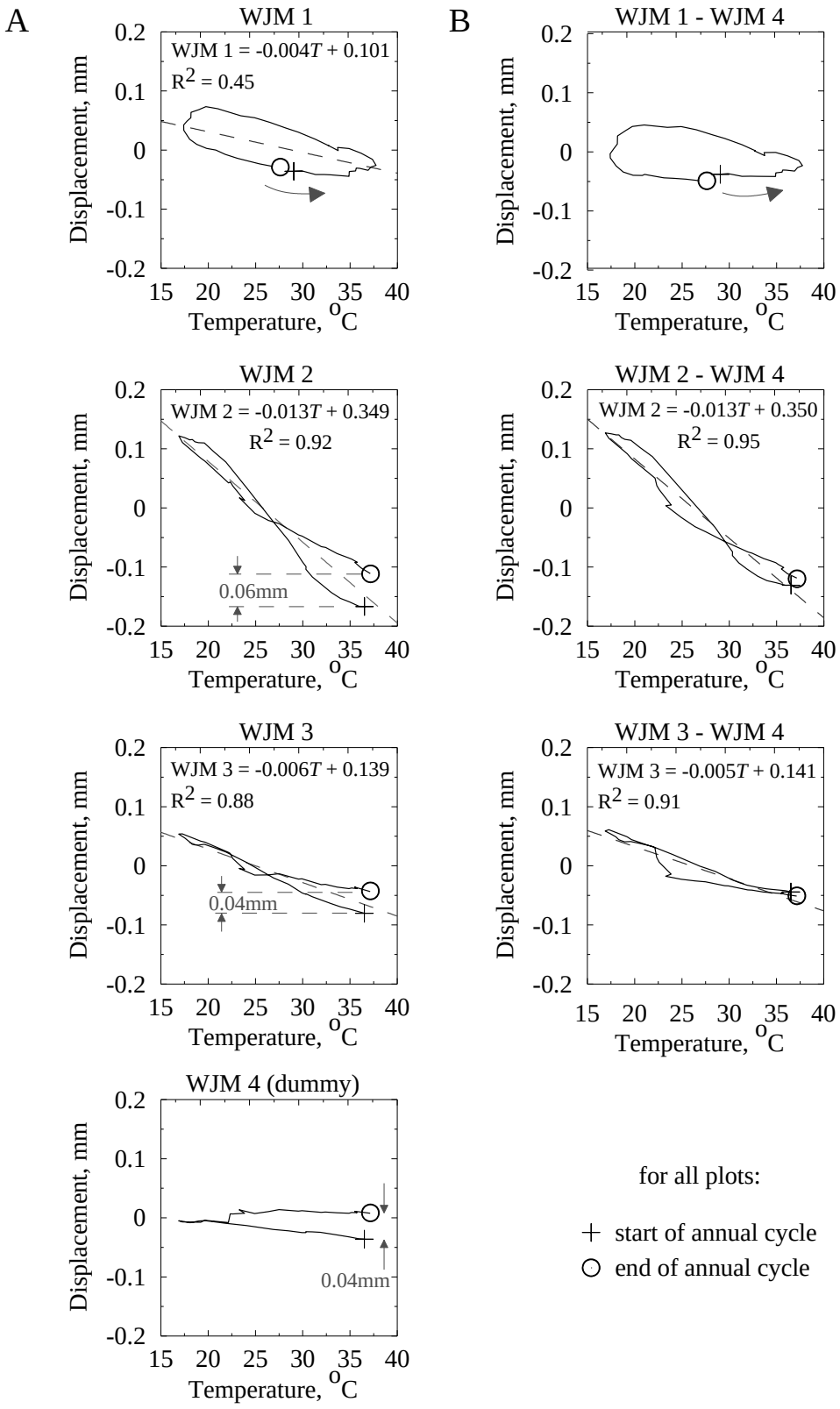

Figure 5-6. Joint opening vs. air temperature smoothed by monthly averaging for one annual cycle (Joint opening is positive): A) smoothed data with no correction where accumulated annual displacement is denoted, and B) WJM 1,2,3 corrected for apparent temperature effect as obtained from dummy transducer WJM 4. WJM 1 from May 2010 to May 2011, WJM 2,3,4 from August 2009 to August 2010. Best fit linear curves are shown as dashed gray lines.

5.4 Thermally induced block displacement

In this section the possibility of obtaining thermally induced block displacements in Masada rock slopes is explored, given the measured seasonal temperature amplitude and the mechanical and physical properties of the rock mass.

A conceptual model of thermally induced block sliding is schematically illustrated in Figure 5-7 following original ideas presented by Watson et al. (2004). With seasonal cooling the sliding block contracts, as a response the tension crack opens, and the wedge block penetrates into the newly formed opening in the tension crack. In summer, when the temperature rises, the sliding block expands and the wedge block is locked in place, prompting compressive stress generation in the block system and pushing the sliding block down slope. In the next cooling season shrinking of the sliding block enables further penetration of the wedge into the tension crack, and consequently further down slope block displacement commences in the summer by shear sliding along the sliding surface.

Gunzburger et al. (2005) argue that thermo-mechanical creep may take place without necessarily having a wedge in the tension crack, for instance when the sliding bock is located in a critical state from a mechanical stand point, namely very close to its limiting equilibrium. In the wedging mechanism, however, the block can slide downward even if it rests on gently dipping sliding surfaces, as will be shown later. Moreover, the wedging fragments are required in cases where the rock underlying the sliding plane also undergoes thermally induced expansion and contraction at the same rate and amount as the sliding block. In such a case, only a continuous supply of rock fragments into the opening tension crack will enable compressive stresses to develop and will prevent closure of the tension crack, thus allowing progressive down plane displacement. A similar wedging process has been suggested for fluvial erosion of river bedrock by plucking of loosened blocks (Whipple et al., 2000).

A recent photograph of Block 1 in EMS is shown in Figure 5-8, where the old EJM 1 and 2 that were installed in 1998 are still visible today. Inspection of the photograph reveals that the block has clearly separated from the cliff over the historic time by accumulated displacement of about 200 mm, and that sizeable rock fragments fill the aperture of the tension crack. It is suggested here that these rock fragments can play the role of the wedge block in a thermally induced wedging mechanism. In order to test the applicability of a thermally induced wedging mechanism for the observed displacement of Block 1 in Masada, an analytical approach suggested by Pasten (2012) is utilized in the next section.

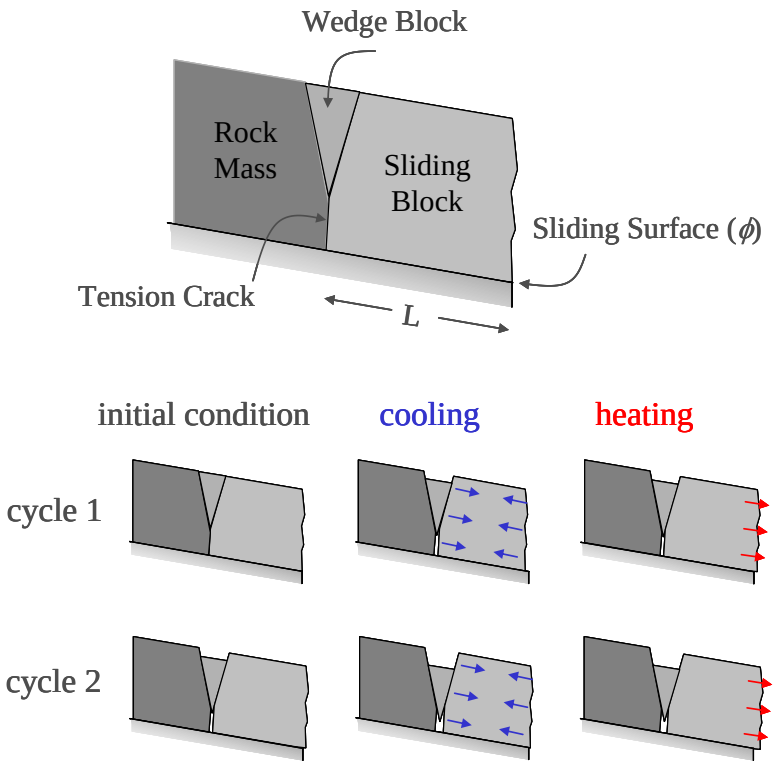

Figure 5-7 . Cartoon showing the principle elements of the thermally - induced wedging mechanism.

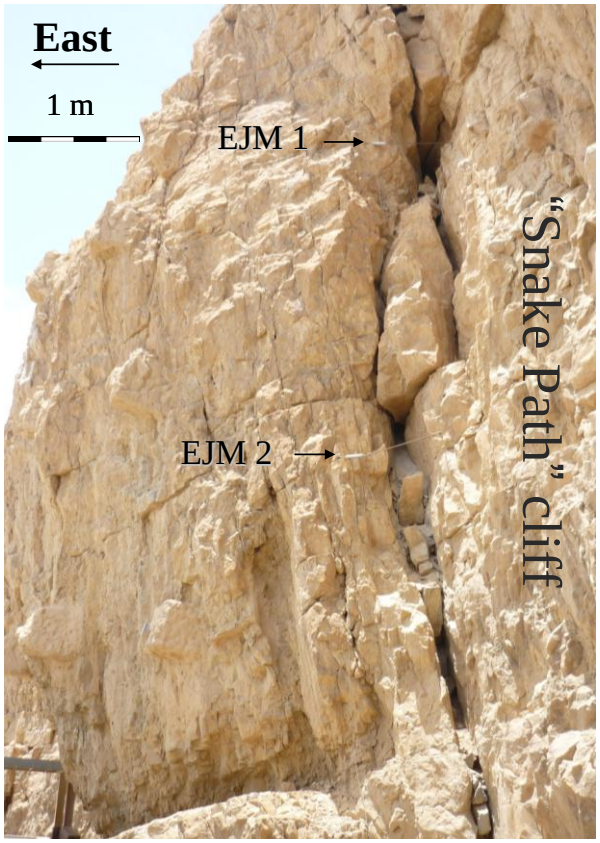

Figure 5-8. Wedge blocks in the tension crack of Block 1 at EMS. Block 1 is used for comparison between thermally and dynamically induced sliding mechanisms (see text).

5.4.1 Theoretical considerations

Consider the exact geometry of Block 1 as shown in Figure 5-9. The tension crack of length L_W is filled with rock fragments that represent the wedge block shown in the conceptual model in Figure 5-7 and the actual rock fragments captured in the photograph in Figure 5-8. The length and height of the sliding block are L_B and H, respectively.

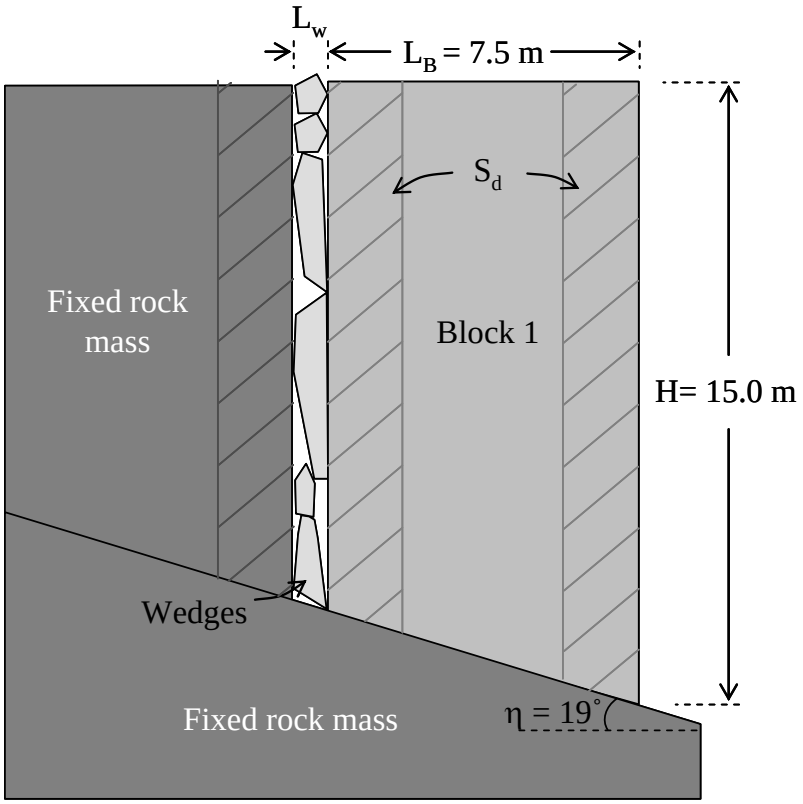

Figure 5-9. Exact geometry of Block 1 in the East slope of Masada with rock fragments representing the wedge block in the tension crack. S_d is the skin depth, L_w is the wedge length and L_B is the block length.

It is assumed here that the rock block is a homogeneous slab experiencing a change of temperature in its center from an initial temperature T_o to a new boundary temperature T_1. The homogenization time t^* required for the block center temperature to reach 99% of the new boundary temperature T_1 can be estimated as $t^* = 2 \cdot L^2/D_T$, where L is the slab length and D_T is the rock thermal diffusivity of the rock, which is proportional to the rock thermal conductivity (λ), and inversely proportional to its mass density (ρ) and specific heat capacity (C_p) (Carslaw and Jaeger, 1959). Following Pasten (2012), the depth of penetration of the heating front during an annual cycle, referred to here as the "thermal skin depth" (S_d), may be estimated as:

$$S_d \approx \sqrt{\frac{1}{2}\frac{\lambda}{\rho \cdot C_p} t_{\exp}} \tag{5.1}$$

where t_{exp} is the exposure time for the given period of interest, assuming it is shorter than the homogenization time ($t_{exp} < 2 \cdot L^2/D_T$). If $t_{exp} > 2 \cdot L^2/D_T$ then $S_d = L/2$. For a single seasonal cycle $t_{exp} \approx 180$ days is assumed.

Given the physical properties of the Masada rock mass (see next section), the estimated thermal skin depth for Block 1 is wider than the wedge length L_W but smaller than the block length L_B, as shown schematically in Figure 5-9.

Pasten (2012) suggest three displacement components that are involved in the thermal expansion process: the thermal expansion (δ_T), the elastic compression of the rock material (δ_σ), and the elastic shear response along the sliding interface (δ_j). The unconstrained seasonal thermal expansion (δ_T) of both sides of the tension crack as well as the wedge fragments inside the tension crack may be expressed by:

$$\delta_T = \alpha \cdot \Delta T_p \cdot (L_W + 2\beta \cdot S_d) \tag{5.2}$$

where α is the thermal expansion coefficient of the intact rock, ΔT_p is the seasonal temperature change from peak to peak, and β is a coefficient accounting for non-uniform diffusive temperature distribution inside the sliding block and the rock mass ($0 < \beta < 1$). Note that β is introduced when the skin depth S_d is smaller than the half-length of the rock element. During a thermal expansion period, uniform compressive stresses develop in the domain leading to an elastic force within the block. Considering Figure 5-9, the maximum force parallel to the sliding surface (F_{max}) that the frictional resistance of the sliding plane can sustain is:

$$F_{\max} = \gamma L_B (H - \frac{1}{2} L_B \tan\eta)(\tan\phi \cos\eta - \sin\eta) \tag{5.3}$$

where γ is the unit weight of the rock ($\gamma = \rho g$), ϕ is the friction angle of the sliding plane, and η is the inclination of the sliding plane. The elastic displacement δ_σ that is developed in the wedge and the block due to F_{max} is:

$$\delta_\sigma = \frac{F_{\max} \cos\eta}{H \cdot E}(L_W + \frac{L_B}{2}) \tag{5.4}$$

where E is the modulus of elasticity of the rock material. Only the half-length of the sliding block is considered in the initial element length undergoing contraction since the right boundary of the block (see Figure 5-9) is a free surface that does not provide any reaction for F_{max}.

Finally, assuming that the toe of the block (the lower right corner of Block 1 in Figure 5-9) is static during the expansion period, the limiting elastic displacement of the interface parallel to the sliding direction δ_j due to F_{max} is:

$$\delta_j = \frac{1}{k_l} \cdot \frac{F_{\max}}{L_B} \cos\eta \tag{5.5}$$

where k_j is the shear stiffness of the sliding interface. During seasonal thermal heating the permanent plastic displacement δ_p along the sliding surface may be obtained by:

$$\delta_p = \begin{cases} \delta_T - \delta_\sigma - \delta_j & \text{if } (\delta_T - \delta_\sigma - \delta_j) > 0 \\ 0 & \text{else} \end{cases} \tag{5.6}$$

5.4.2 Physical and mechanical properties of the rock mass in Masada

Experimental determination of thermal conductivity

In order to determine the thermal conductivity of Masada dolomite a non-steady-state probe (NSSP) is used in adherence to ASTM D 5334-00 and D 5930-97 standards. A 2.5 mm diameter hole is drilled at the center of cylindrical dolomite samples with a diameter of 68 mm, a height of 48 mm, and a density of 2600 kg/m^3. A 1.2 mm diameter thermo-resistance needle is used as both heating wire representing a perfect line source with heat resistance of R = 83.94 Ω/m and as a temperature sensor at the source (see Figure 5-10A). After a short transient period the temperature difference between the source and the measurement point for a constant heating of the needle can be expressed as:

$$\Delta T = A\ln(t) + B \tag{5.7}$$

where A and B are best-fit parameters that depend upon the heater power Q and the thermal properties of the heated medium. Results of four different tests performed using the NSSP are presented in Figure 5-10B on a semi-logarithmic scale. The thermal conductivity λ can be calculated from the linear slope A after the transient period as follows:

$$\lambda = \frac{1}{A}\frac{Q}{4\pi} \tag{5.8}$$

The average value obtained from four different tests is λ = 1.71 ±0.26 W/(m·K), a typical value for limestones and dolomites (e.g. Rohsenow et al., 1998). Using a rock mass density of 2600 kg/m^3 and assuming a typical heat capacity for dolomites of C_p = 810 J/(kg·K) (e.g. Rohsenow et al., 1998), the estimated thermal skin depth for a seasonal exposure time (Equation 5.1) is S_d = 2.5 m.

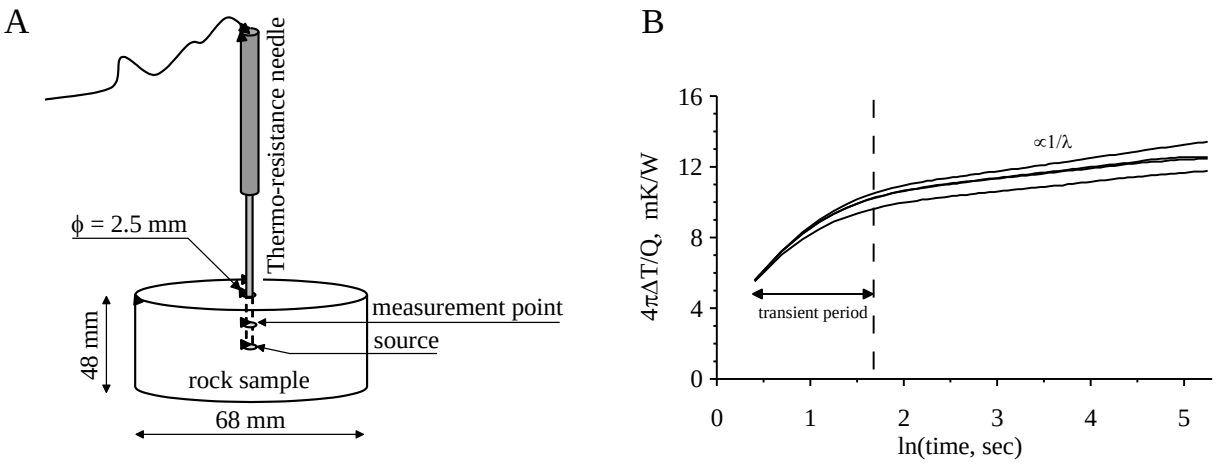

Figure 5-10. The NSSP thermal conductivity experiment in the lab: A) Experimental setting, B) obtained experimental results

Estimating the thermal expansion coefficient from field measurements

Consider the monitored thermal response of the rock mass at WMS over a single seasonal cycle; note that no permanent displacement of the monitored joints is observed (see Figure 5-6B). It is believed that this is because the monitored joints in WMS are clean and tight, i.e. because a ratchet mechanism is not possible. These results can therefore be used to compute the thermal expansion coefficient (α) of the Masada rock mass, assuming that the air temperature and the rock temperature across the skin depth are equal during the exposure time. The monitored block length in WMS (L_B = 1.6 m) is smaller than the estimated skin depth for a seasonal exposure time (S_d = 2.5 m). Therefore, the joint meter output represents the contraction and expansion of the rock material on both sides of the joint across the thermally affected zone of length L_o , which is assumed to be equal to half of the block length and the equivalent skin depth into the rock mass (see Figure 5-11A), namely $L_o = 0.5\, L_B + \beta\, S_d$. The thermal expansion coefficient α can be evaluated assuming a linear thermo-elastic response of L_o as follows:

$$\alpha = \frac{d\varepsilon}{dT} = \frac{dL}{L_0} \cdot \frac{1}{dT} = \frac{dL}{0.5L_B + \beta \cdot S_d} \cdot \frac{1}{dT} \tag{5.9}$$

where dL = 0.14 mm is the annual joint displacement measured by WJM 2 during an annual temperature amplitude of dT = 9 ˚C (Figure 5-4). The wedge length in L_o in Equation 5.9 is ignored because the monitored joint in WMS is extremely tight (see Figure 5-2A). The influence of the coefficient β on the computed thermal expansion coefficient is shown in Figure 5-11B. Typical α values for dolomites are 6 X 10^{-6} to 8 X 10^{-6} 1/˚C (e.g. Franklin and

Dusseault, 1988). A range of values for β between 0.45 - 0.7 is therefore assumed in further analysis.

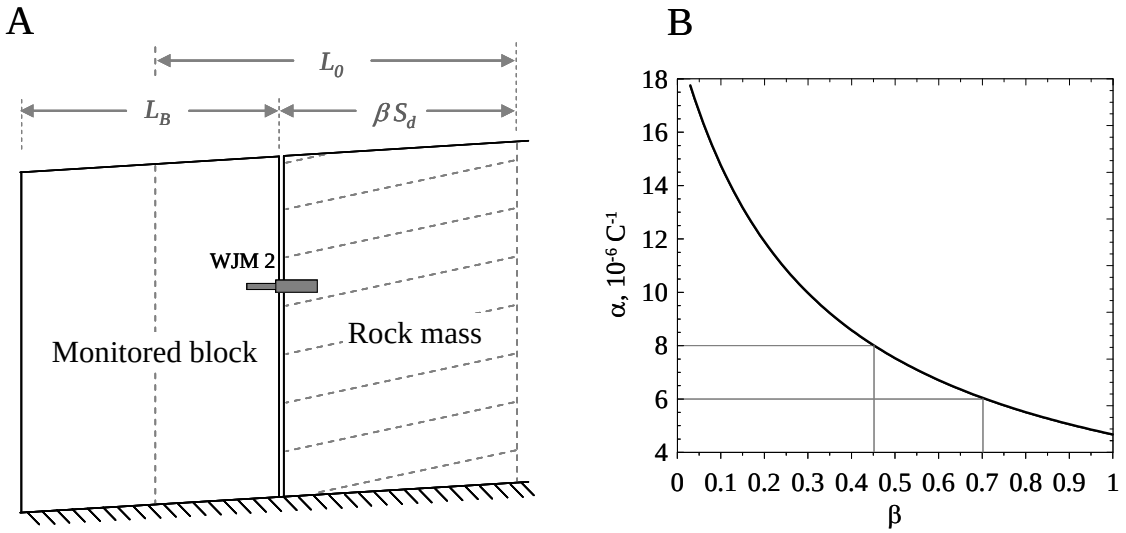

Figure 5-11. A) Definition of length parameters used in Equation 5.9, B) thermal expansion coefficient *a* as a function of the assumed non-uniform diffusive temperature distribution *b* . Taking *b* = 0.45 and 0.7 yields *a* = 8 X 10^{-6} and 6 X 10^{-6} 1/C ˚, respectively.

An experimental determination of shear stiffness and strength

Consider Figure 5-12 where results of direct shear tests performed on a bedding plane surface from Masada are presented. In this plot, shear stress vs. shear displacement is shown for seven cycles of loading, unloading, and reloading under increasing normal stress from 0.17 to 1.38 MPa, with the normal stress kept constant during each shear sliding segment using closed-loop servo control. In each cycle the sample is sheared forward for a distance of 0.5 mm at a displacement rate of 0.025 mm/sec. Inspection of Figure 5-12 reveals that a shear displacement of at least 0.09 mm would be required to reach steady state sliding for this particular interface for a sample length of 10 cm. Consequently the shear stiffness for the tested interface k_j is estimated to be 1.0 GPa/m for normal stress of 0.17 MPa. A Mohr - Coulomb failure envelope obtained from reduced data presented in Figure 5-12 yield a peak friction angle of 41˚ for the tested bedding plane surface of Masada dolomite.

5.4.3 Thermally induced sliding of Block 1 in EMS

To check the theoretical possibility of obtaining thermally induced sliding in Masada, the measured geometry of Block 1 in EMS (see Figure 5-9) is used. The physical properties of the rock mass obtained experimentally both in the laboratory and in the field (see Table 5-2)

are used as input parameters for the analytical approach summarized in Equations 5.1 – 5.6 above. The permanent annual thermal plastic displacement thus obtained is plotted in Figure 5-13 as a function of wedge length, for non-uniform diffusive distribution coefficients β = 0.45 and 0.7. The calculated annual displacement rate for Block 1 varied from 0.181 to 0.210 mm/year and from 0.238 to 0.260 mm/year for β = 0.45 and 0.7, respectively, when increasing the opening of the tension crack from 0 to 200 mm.

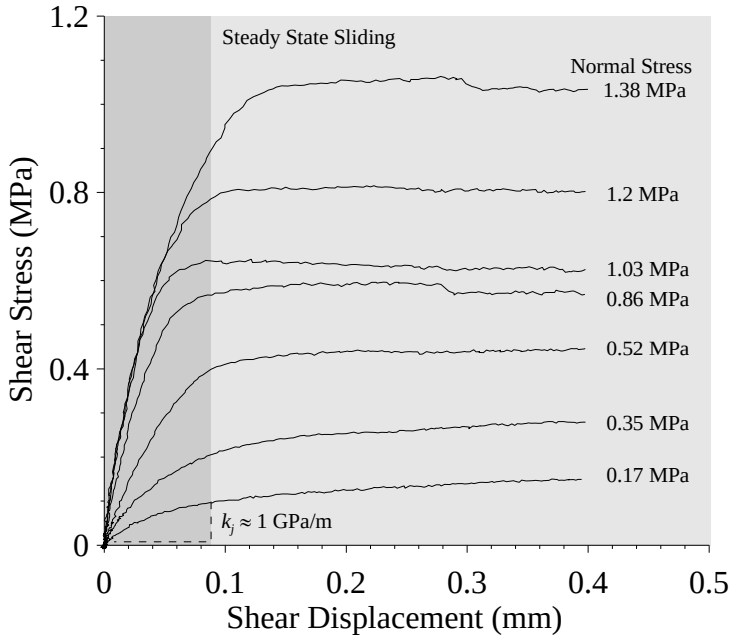

Figure 5-12. Results of direct shear tests performed on a natural bedding plane sample from Masada (after Hatzor et al., 2004).

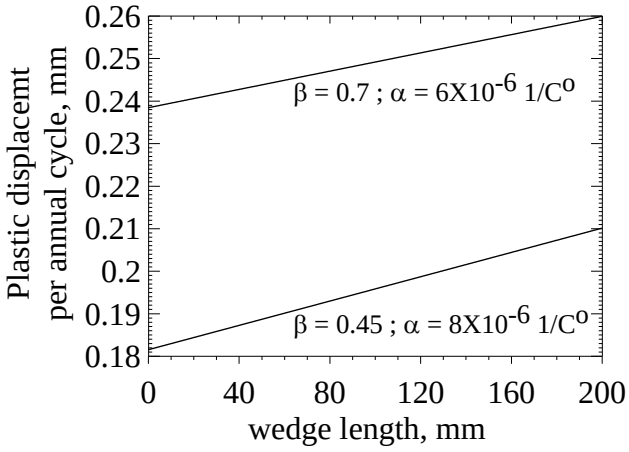

Figure 5-13. Thermally induced plastic displacement for a single annual cycle as a function of the wedge length (assuming β = 0.45 and 0.7), as obtained using the analytical model of Pasten (2012).

5.5 Seismically induced block displacement

A thermally-induced wedging mechanism that can explain one-directional block displacement in jointed rock masses has been discussed above. This mechanism operates under constant gravitational loading and is driven by cyclic thermal changes. The position of Masada, near a major fault – the Dead Sea rift, calls for a consideration of the possibility of block displacements due to seismic vibrations. Block 1 in the East slope of Masada (EMS) is chosen as a case study for testing two different driving mechanisms: thermal vs. seismic, because the geometry of this finite and removable block, the amount of opening of the tension crack, and relevant physical and mechanical parameters for this block are known. Moreover, there is a reasonably well constrained input seismic motion that could be used for dynamic seismic analysis for this block (e.g. Zaslavsky and Shapira, 2000), and the recurrence time of strong earthquakes is available (e.g. Begin, 2005; Hamiel et al., 2009).

Masada Mountain is situated along the Dead Sea transform (see Figure 5-1A) with moderate seismic activity and an expected maximum earthquake moment magnitude (M_w) of 7.5 (Begin, 2005; Shapira et al., 2007). According to the Israeli building code 413 a Peak Ground Acceleration (*PGA*) level of 0.22 g has an exceedance probability of 10% at least once within a period of 50 years in Masada area, corresponding to a return period of 475 years. The estimated return period for the Dead Sea region is about 300 years and 4000 years for earthquakes greater than $M_w \geq 6.0$ and $M_w \geq 7.0$, respectively (Begin, 2005; Shapira et al., 2007). Since instrumental records of strong earthquakes (Mw > 6.0) in the Masada region are not available, a strong event that took place elsewhere in the same tectonic setting (Nuweiba earthquake) is used as an input in the analysis.

5.5.1 Seismic input motion for dynamic analysis of block sliding

The M_w = 7.2 Nuweiba earthquake occurred on November 22, 1995, in the Gulf of Eilat (Aqaba) with an epicenter near the village of Nuweiba, Egypt (Figure 5-1A). The main shock was recorded at a seismological station in the city of Eilat, located 70 km north of the epicenter. The recording station was positioned in a school basement built on a soil cover of 50 meter thickness composed of Pleistocene alluvial fan deposits. The recorded acceleration time history therefore represents the site response of the soil layer in Eilat, rather than hard bedrock. A one-dimensional multi layer model for the soil was utilized by Zaslavsky and Shapira (2000) to obtain the rock response by de-convolution, the transfer function based on material and physical parameters determined using both seismic refraction survey data and down-hole velocity measurements in the city of Eilat.

The de-convolution response spectrum thus obtained for the city of Eilat represents a "characteristic" rock response at a distance of 70 km from the epicenter of a M_w = 7.2 earthquake in the Dead Sea rift system. To scale this record to the foothills of Masada, the well-established attenuation relationships between *PGA*, moment magnitude, and epicenter distance suggested by Boore et al. (1997) is used here. Note that this attenuation relationships is also used for seismic risk assessment in the Israeli building code 413 (Shapira et al., 2007). The Nuweiba earthquake record as measured in Eilat, de-convoluted for rock response, and scaled for *PGA* = 0.275 *g*, is shown in Figure 5-14A, representing a "characteristic" M_w = 6.0 Dead Sea rift earthquake recorded at a distance of 1 km from the epicenter.

Although the Masada site is situated directly on rock, a significant topographic effect was recorded at the site during a geophysical survey in September 1998 (Zaslavsky et al., 2002) and it must be considered in the development of a realistic input motion for dynamic analysis of a block situated at the top of the mountain. The empirical response function for Masada (after Zaslavsky et al., 2002) is plotted in Figure 5-14B where three characteristic modes are found at f = 1.3, 3.8, and 6.5 Hz, with frequencies higher than 10 Hz filtered out. This empirical response function for Masada top is applied to the scaled rock response record of Nuweiba to obtain the expected rock response at the top of the mountain. Note that during the scaling procedure according to the attenuation relationship, the frequency content of the signal remains constant. The frequency content is changed after the convolution procedure according to the site response of the mountain, as discussed above. An example of an output using this procedure for a M_w = 6.0 event is shown in Figure 5-14C. As can be appreciated from the specific examples shown in Figure 5-14A and Figure 5-14C, the expected *PGA* of 0.275 *g* at the valley floor (Figure 5-14A) is amplified by this procedure to 0.465 *g* at the mountain top (Figure 5-14C). A flowchart summarizing this scaling procedure is shown in Figure 5-14D.

By utilizing the attenuation relationship of Boore et al. (1997) the expected *PGA* as a function of earthquake epicenter distance from Masada for moment magnitudes 6.0 and 7.5 Dead Sea rift earthquakes is shown in Figure 5-15 (dashed lines), representing *PGA* on bedrock at the foothills of Masada. For each curve, the amplified site response at the mountain top (solid lines) is obtained by convolution with the empirical response function for the topographic site effect at Masada as explained above. The *PGA* values of four amplified earthquakes with epicenter at a distance of 1 km from Masada are also shown in Figure 5-15 (symbols) for M_w levels of: 6.0, 6.5, 7.0, 7.5. The acceleration time series for these four

amplified earthquake records are used as input for numerical analysis of seismic block response using the numerical, discrete-element, Discontinuous Deformation Analysis (DDA) method.

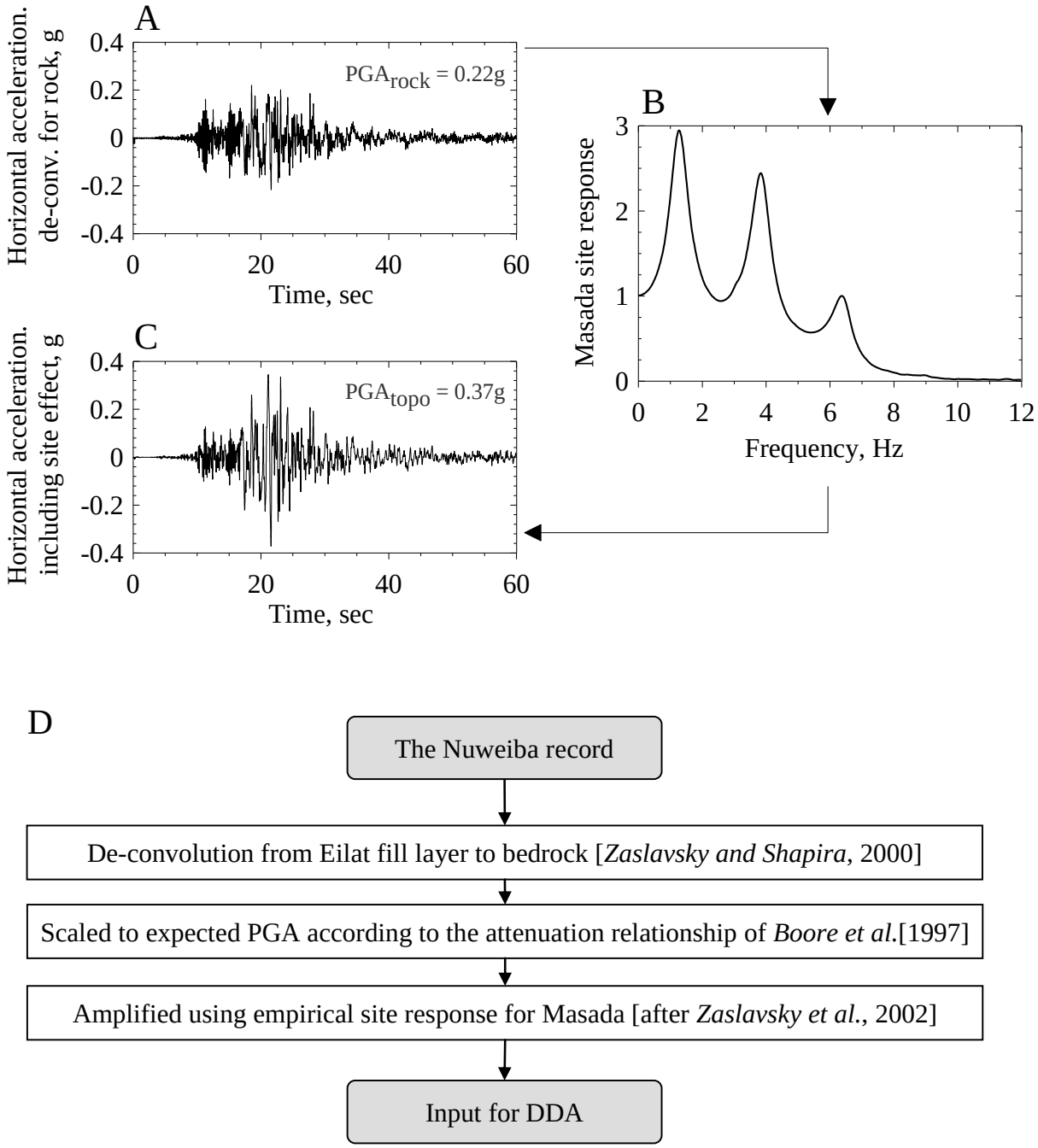

Figure 5-14. The input procedure for seismic loading simulations with DDA. A) The Nuweiba earthquake as recorded in Eilat on a fill layer de-convoluted for bedrock response (Zaslavsky and Shapira, 2000) and scaled to PGA = 0.275*g*, corresponding to a Mw = 6.0 earthquake at a distance of 1 km from Masada (see Figure 5-15), B) an empirical site response function for Masada (after Zaslavsky et al., 2002), C) convoluted time series of the modified Nuweiba record (Figure 5-14A) to include the empirical site response function for Masada (Figure 5-14B), and D) flowchart summarizing the input procedure.

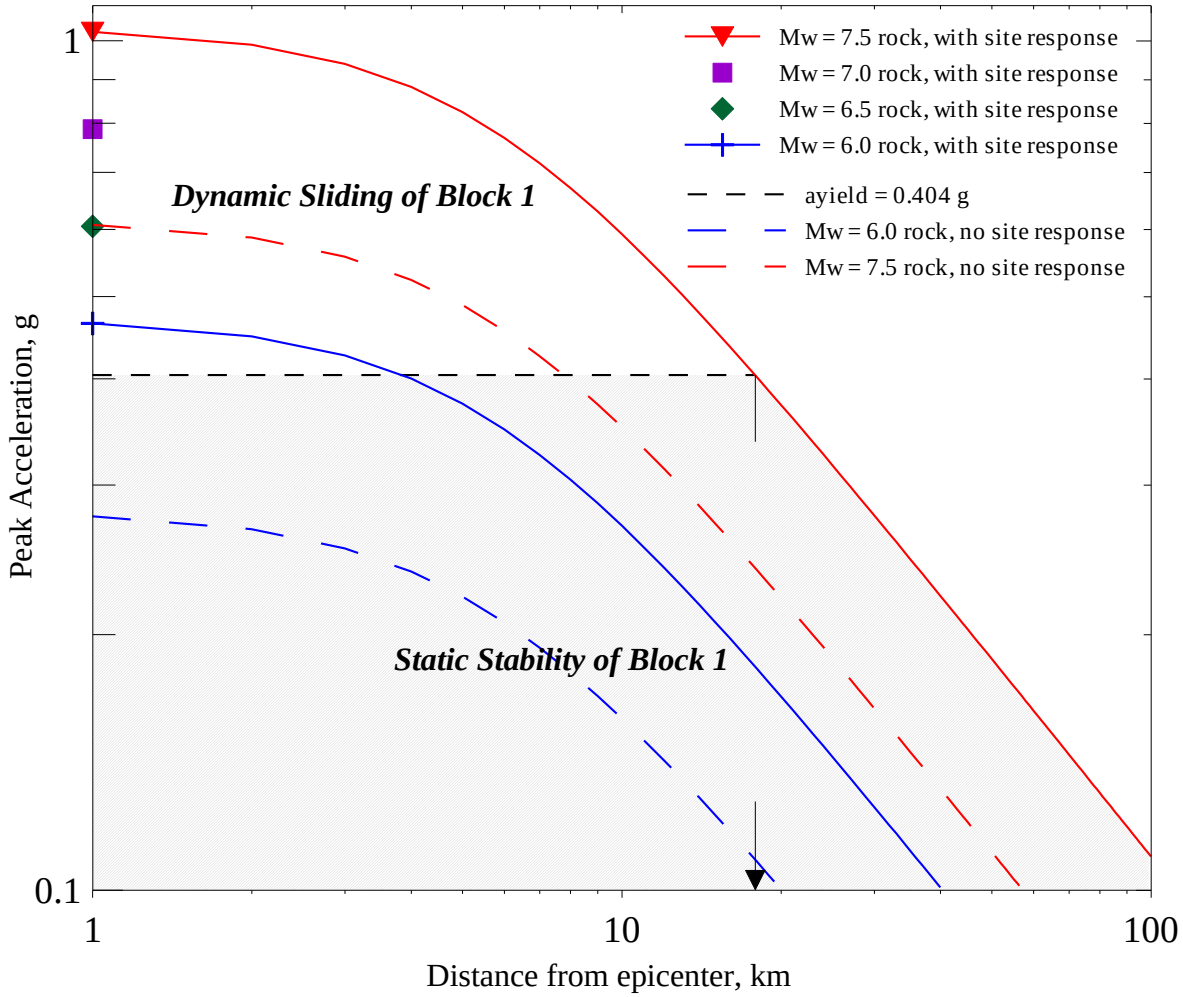

Figure 5-15. Assumed attenuation curves (after Boore et al., 1997) for Dead Sea Rift earthquakes (dashed lines) with amplification due to topographic site effect at Masada (solid lines and symbols). Shaded region delineates conditions at which seismically-induced sliding of Block 1 at Masada is not possible.

5.5.2 Numerical procedure using DDA

Results obtained with DDA are sensitive to the choice of both the numerical contact spring stiffness (k) and the time step size (Δt). Therefore, sensitivity analysis has been done to select the most appropriate couple of these numerical control parameters. In this case the geometry of Block 1 resting on an inclined plane with no wedge in the tension crack is used. The block subjected to synthetic sinusoidal input loading consisting of constant amplitude and frequency, a problem for which an exact analytical solution exists (Newmark, 1965). 2D-DDA code verification for this problem is shown by Kamai and Hatzor (2008). Previous code verifications for dynamic cases indicate that the optimal contact spring stiffness in DDA is frequency-dependent. To obtain the optimal k value for this case the two dominant frequencies of the mountain f_1 = 1.3 and f_2 = 3.8 Hz as obtained from the topographic site

response survey (see Figure 5-14B) are used. Eighteen simulations of sinusoidal input functions are performed for each of the dominant frequencies of Masada mountain (f_1 and f_2) with k = 1, 5, 10, 100, 500, 1000 GN/m, Δt = 0.01, 0.005, 0.002 sec, and an arbitrary constant value of 0.5 g for input amplitude.

For each input frequency the optimal numerical parameters are searched based on the lowest relative error between the analytical and numerical solutions at the final position of the block, where the relative error (R_e) for the displacement solutions (D) is defined as:

$$R_e = \frac{\left|D_{analytical} - D_{numerical}\right|}{\left|D_{analytical}\right|} \cdot 100\% \tag{5.10}$$

The results of the sensitivity analysis are shown in Figure 5-16. The optimal contact spring stiffness values thus obtained are 10 and 500 GN/m for f_1 and f_2 respectively, and the optimal time step size is 0.005 sec for both input frequencies. Using the optimal numerical control parameters a comparison between numerical DDA and analytical results are shown in Figure 5-17. To find the optimal contact spring stiffness when the two dominant frequencies are used as input, each set of relative error values obtained from the numerical computation at each input frequency is multiplied and the lower multiplied value is searched. The obtained optimal contact spring stiffness for the two dominant frequencies of Masada is 500 GN/m. For a list of mechanical and numerical parameters used in the fully dynamic seismic analysis see Table 5-2.

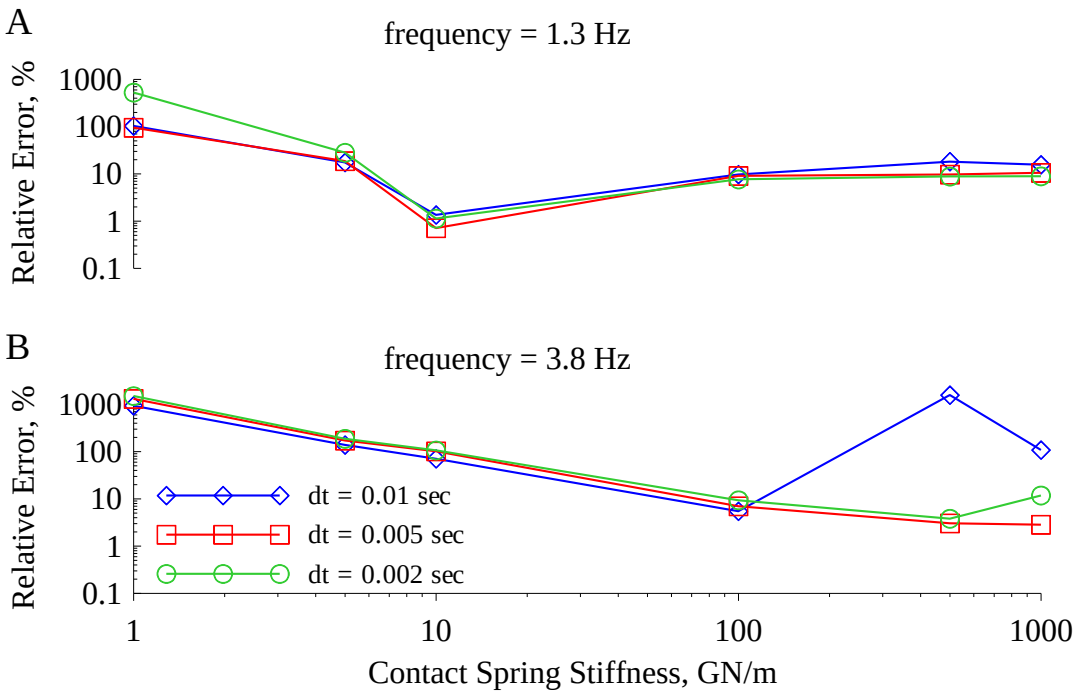

Figure 5-16. Sensitivity analysis results: The relative numerical error between the analytical and numerical solutions as a function of contact spring stiffness and varied time step size.

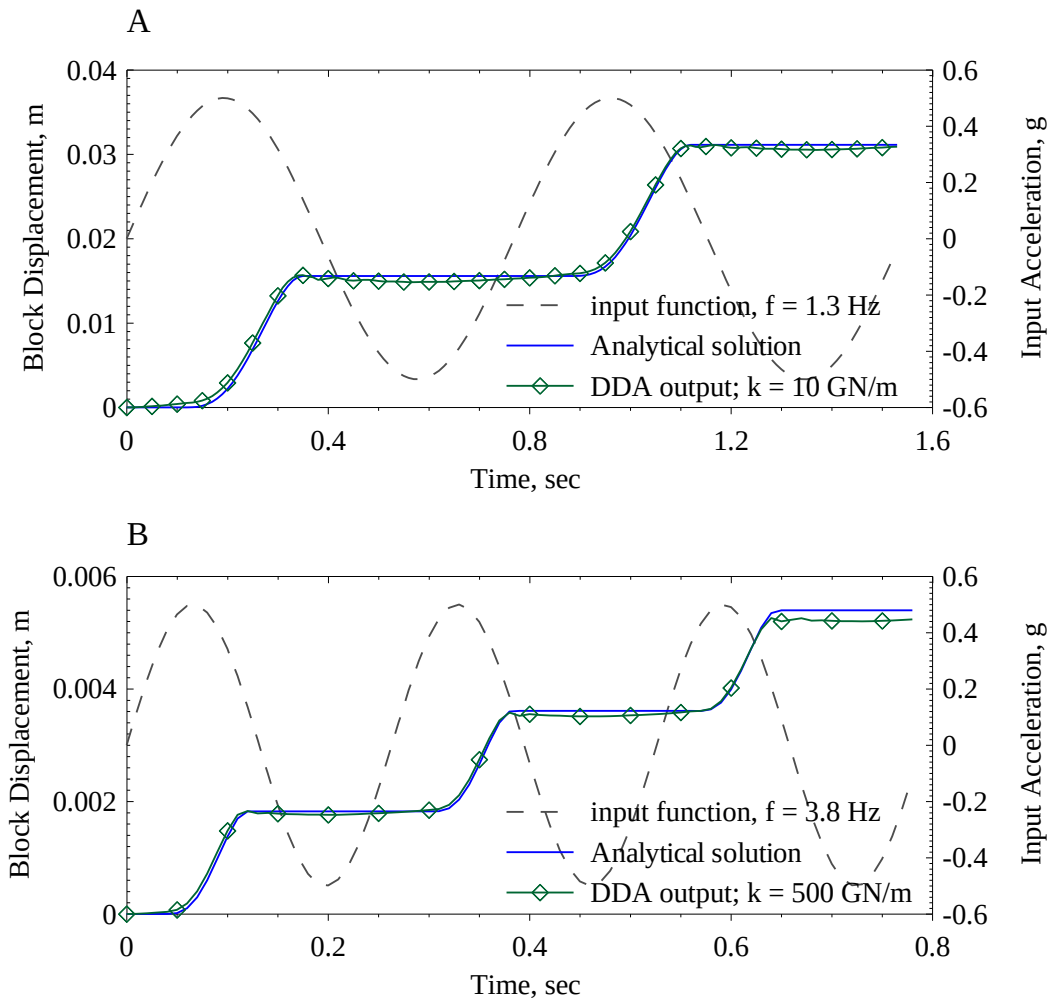

Figure 5-17. DDA results vs. analytical (Newmark's) solution for the dynamic displacement of Block 1 when subjected to a sinusoidal input function with 0.5*g* amplitude and the two dominant frequencies for Masada (see Figure 5-14B): 1.3 Hz (A) and 3.8 Hz (B). (k is the numerical contact spring stiffness used in DDA).

Table 5-2. Mechanical and thermal properties for Block 1 in EMS used for analytical and numerical solutions

	Symbol	Analytical model Thermal loading	Numerical DDA model Seismic loading
Mechanical Properties:			
Elastic Modulus, GPa	E	40	40
Poisson's Ratio	ν		0.2
Mass density, kg/m^3	ρ	2600	2600
Friction angles, Degrees	ϕ	41	41
Joint stiffness, GPa/m	k_j	1	-
Thermal Properties and Loading:			
Thermal expansion coefficient, C^{-1}	α	6 – 8 X 10^{-6}	-
Annual temperature amplitude, ˚C	ΔT	9	-
Thermal conductivity, W/(m·K)	λ	1.7	-
Specific heat capacity, J/(kg·K)	C_p	810 [a]	-
Numerical Parameters:			
Dynamic control parameter		-	1
Number of time steps		-	12000
Time interval, Sec	Δt	-	0.005
Assumed max. disp. Ratio, m		-	0.005
Contact stiffness, GN/m	k	-	500 [b]

[a] After Rohsenow et al., 1998.

[b] See text is section 5.5.2 for sensitivity analysis procedure.

5.5.3 Results of seismic analysis for Block 1

The horizontal yield acceleration (a_{yield}) for an inclined bedding plane dipping 19˚ with peak friction angle of 41˚ as in the case of Block 1 is readily obtained using pseudo-static analysis (see Goodman and Seed, 1966) at a_{yield} = 0.404 g. The a_{yield} value thus obtained constrains the epicenter location of the maximum expected earthquake (M_w = 7.5) at the Dead Sea rift capable of triggering sliding of Block 1, to a distance of up to 20 km from Masada (see Figure 5-15).

DDA results for seismic analysis of Block 1 subjected to amplified Nuweiba records corresponding to M_w = 6.0, 6.5, 7.0, 7.5 Dead Sea rift earthquakes at an epicenter distance of 1 km from Masada are shown in Figure 5-18. For moderate earthquakes ($M_w \leq 6.5$) the block displacement per single event is expected to be lower than 42 mm, whereas for strong earthquakes ($M_w \geq 7.0$) the block is expected to slide more than 447 mm along the inclined bedding plane in a single event. The mapped opening of the tension crack in the field is only 200 mm (see Figure 5-18), a value which constrains feasible earthquake scenarios, as discussed below.

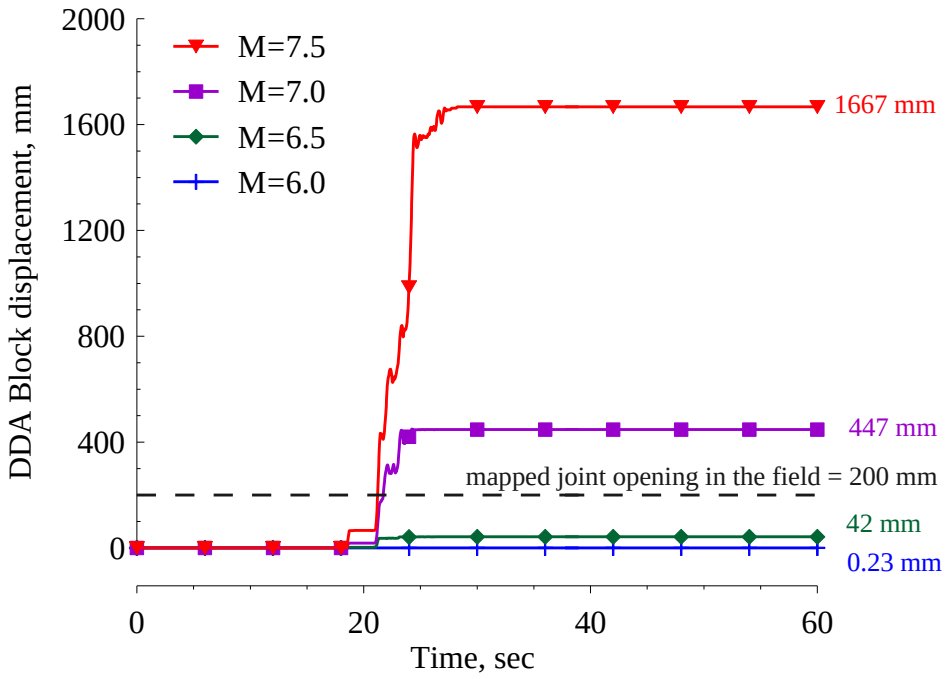

Figure 5-18. DDA results for dynamic displacement of Block 1 when subjected to amplified Nuweiba records corresponding to earthquakes with moment magnitude between 6.0 to 7.5 and epicenter distance of 1 km from Masada. Mapped joint opening in the field is plotted (dashed) for reference.

5.6 Discussion

5.6.1 Thermo elastic behaviour of the Masada rock mass

This chapter examines the theoretical possibility for thermally induced rock block displacement due to a natural wedging mechanism, where the key elements are the intact rock mass, the tension crack, the wedge fragments, the sliding block, and the sliding surface (see Figure 5-7). Although the geometry of the model discussed in this chapter is well defined, it is argued that the presented mechanism may lead to permanent sliding block displacements wherever wedging blocks are formed in tension cracks, as also suggested by Watson et al. (2004). Moreover, it is shown that the thermal induced sliding can also occur on shallow dipping planes, which are usually not considered as unstable configurations.

The monitoring station at West Masada (Figure 5-2) is installed on a block that is separated from the rock slope by clean and tight joints with no wedge fragments. It is assumed that for this reason, no permanent displacement has been recorded during the monitoring period in the West slope. On the other hand, it is assumed that the wedge fragments inside the tension crack of Block 1 in the East slope (Figure 5-8) can trigger the wedging mechanism conceptually illustrated in Figure 5-7. Since cable bolts were installed during the summer of 1998 to anchor Block 1 to the cliff, in connection with a comprehensive slope reinforcement campaign, no evidence for permanent displacement since then is available. The results obtained from the monitoring system at WMS are therefore utilized to evaluate the thermal expansion coefficient α of the Masada rock mass, for the analysis of thermally induced displacement of Block 1 in EMS.

Thermal conductivity measurements performed on a sample from Masada (Figure 5-10) enable to estimate the skin depth for the Masada rock mass for a seasonal exposure time at $S_d \approx 2.5$ m, assuming homogeneous, one-dimensional, temperature distribution within the rock element. In reality, however, the temperature distribution within the rock mass is not homogenous and the parameter β for non-uniform diffusive temperature distribution must be considered. A range of values of $0.45 < \beta < 0.7$ is used here assuming a typical range for the thermal expansion coefficient α for the Masada rock mass from 6×10^{-6} to 8×10^{-6} 1/°C (e.g. Franklin and Dusseault, 1988). This set of parameters (for α and β) are used to calculate the permanent thermally induced annual plastic displacement using the analytical model suggested by Pasten (2012).

It is important to note that the parameter β depends on the rock mass geometry and on

the tension crack aperture. In the West station, the data from which the parameter β is based on, the tension crack is very tight, and therefore a non-uniform thermal distribution within the rock mass is expected and consequently a relatively thin thermal skin depth. On the other hand, the tension crack behind Block 1 in EMS is relatively wide and the block is clearly separated from the rock slope (Figure 5-3A and Figure 5-8); it is therefore expected that the block responds more uniformly and therefore the actual value of parameter β may be higher than assumed here.

5.6.2 Block displacement rate under thermal and seismic loading

Block 1 is used to study displacement rates under thermal loading on one hand and seismic loading on the other hand. The geometry of the block is completely known, as well as the mechanical and physical parameters of the intact block material and the shear strength and shear stiffness of the sliding surface. Moreover, the magnitude of opening in the tension crack is readily measurable in the field and amounts to 200 mm. An inclination of 19˚ and a friction angle of 41˚ for the sliding plane are assumed in the analysis, based on field and laboratory measurements.

Analytical results (Figure 5-13) show that the thermally induced sliding rate of Block 1 ranges from 0.181 to 0.210 mm/year for β = 0.45, and from 0.238 to 0.260 mm/year, for β = 0.7. The sliding rate increases with time because the increased aperture of the tension leads to increased wedge block length L_W. This is true as long as the assumed skin depth is larger than the wedge length ($S_d > L_W$) and provided that a continuous supply of detritus material is made available from higher segments of the rock slope above the tension crack. Furthermore, it is assumed that the crushing strength of the detritus material is sufficiently high so as to sustain the compressive force F_{max} that develops in the block system during the expansion periods.

To obtain the displacement rate under seismic loading one must first make some assumptions regarding the recurrence probability of Dead Sea rift earthquakes. Based on paleo-seismic, historical, and instrumental records, the return period for moderate (M_w = 6.5) and strong (M_w = 7.0) Dead Sea rift earthquakes is estimated to be 1100 and 4000 years, respectively (Begin, 2005; Shapira et al., 2007). Consider Figure 5-18 where results of dynamic numerical analyses for the displacement of Block 1 under amplified Dead Sea rift M_w = 6.0 – 7.5 earthquakes with epicenter at a distance of 1 km from Masada are presented. From this chart equivalent displacement rates of 0.04 mm/year and 0.11 mm/year may be deduced for moderate (M_w = 6.5) and strong (M_w = 7.0) Dead Sea rift earthquakes. These rates clearly provide an upper bound because they apply to an earthquake epicenter at a distance of

only 1 km from Masada; with increasing epicenter distance up to 20 km from Masada (see Figure 5-15), the expected displacement of Block 1 under a single episode, and consequently the deduced displacement rates, would naturally be smaller.

The displacement rates of Block 1 under moderate Dead Sea rift earthquakes at an epicenter distance of 1 km from Masada, along with the rate deduced from the thermal mechanism, are plotted in Figure 5-19. Inspection of Figure 5-19 reveals that the thermal mechanism is more dominant than the seismic loading mechanism when each is considered individually.

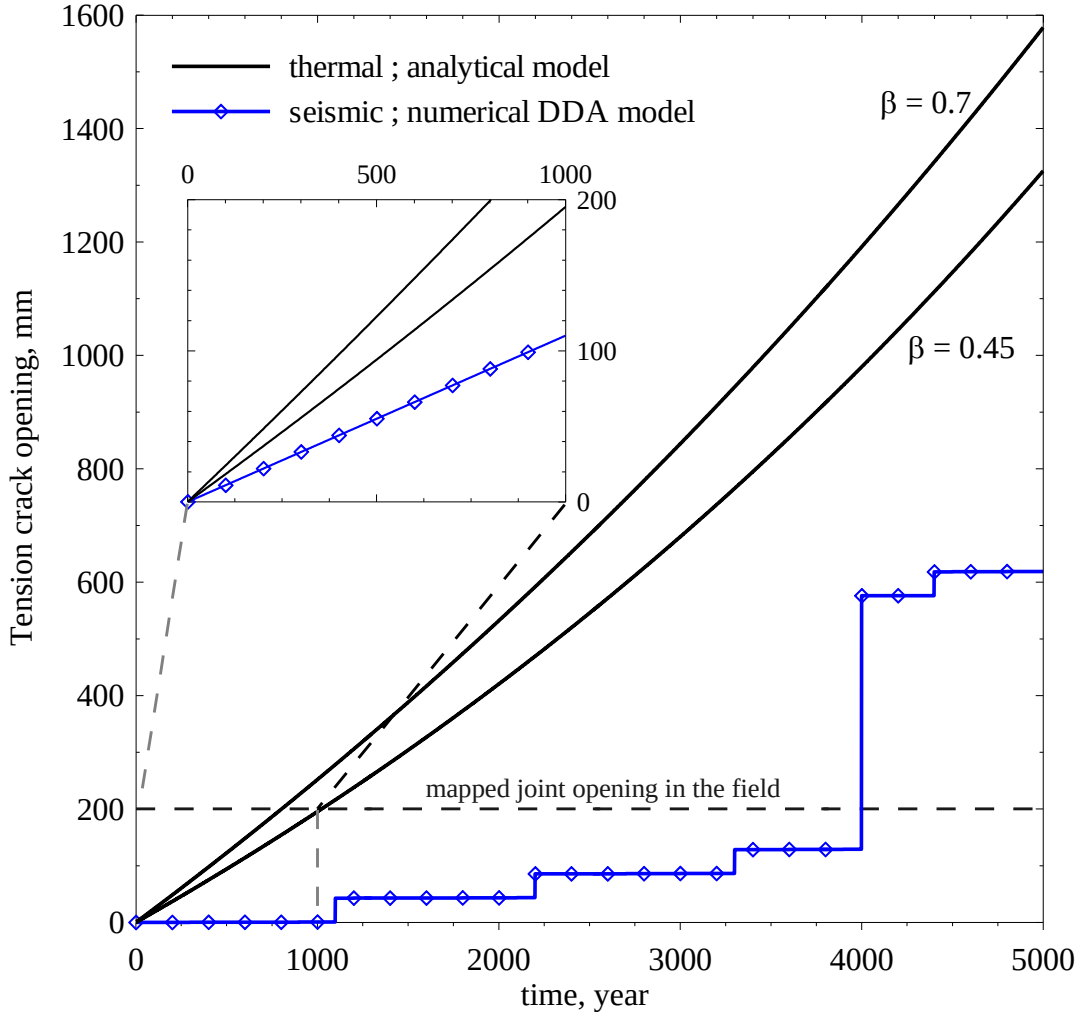

Figure 5-19. Comparison between thermally and seismically induced displacement rates for Block 1. Thermal displacement rate is calculated assuming β = 0.45 and 0.7. Seismic displacement rate is obtained by summation of earthquake magnitudes 6.0 to 7.0 with epicenter located 1 km from Masada based on the seismicity of the region. The seismic rates in the zoom-in box are for the long term seismicity (5000 years).

5.6.3 Paleo-seismic implications

The total mapped opening of the tension crack in Block 1 (200 mm) imposes some constraints on possible paleo-seismic scenarios at Masada. Consider for example strong Dead Sea rift earthquakes ($M_w \geq 7.0$) with an epicenter 1 km from Masada, the amount of sliding in a single episode is expected to be greater than 447 mm (see Figure 5-18); therefore Block 1, in its current configuration, could never have experienced a $M_w \geq 7.0$ earthquake at such close proximity to Masada. However, a single $6.5 < M_w < 7.0$ event at the foothills of Masada, or a stronger event ($M_w > 7.0$) at a distance of up to 20 km from the site (see Figure 5-15), could open the tension crack by the observed 200 mm at once. Therefore, these last two scenarios cannot be ruled out based on the field and analytical data.

It has been established that under thermal loading the mapped opening of 200 mm could have been attained over a period of ca. 1000 years assuming climatic conditions have remained more or less the same over this time period. To examine if this opening could have been triggered by seismic vibrations it would be instructive to search the historic regional earthquake catalogue and seek a $M_w > 6.5$ event at a distance of up to 20 km from Masada during that time window. The historical earthquake catalog in the Eastern Mediterranean region is based on a long and well-documented historical record and a wealth of archaeo-seismological information. Based on the historical earthquake catalog compiled by Ben-Menahem (1991), the earthquakes of May 362 and of May 1834, both located at the Eastern Lisan peninsula (for location see Figure 5-1A) with estimated local magnitude of 6.7, may have been possible candidates for triggering the observed displacements in Block 1, however the low accuracy of the assumed magnitude and location precludes any robust conclusions.

CHAPER 6 - CONCLUSIONS

The objectives of this dissertation were to develop an enhanced approach that numerically simulates complex rock structures and utilize it for dynamic analysis of rock mass in the context of slope stability. The slope stability issues discussed in this research are the seismically-induced sliding of tetrahedral wedge and the thermally-induced ratchet model. Since both of these problems deal with a single removable block, rather than a complex structure, the new hybrid geo-DFN-DDA preprocessor is demonstrated here for exploring the effect of mechanical layering on the stability of underground opening and the surface settlement. Since the hybrid approach has been established in this research, it can now be used for analyzing deformations in complex structure for any rock mechanics problem.

6.1 Simulating mechanically layered rock masses

The combination of the geologically realistic fracture models of mechanical layering provided by FRACMAN, and the advanced block-cutting algorithm and forward modeling capabilities of DDA can provide a powerful design tool in geomechanic analyses.

Classic mechanically layered rock masses, as simulated in the FMML model, obey the maximum Terzaghi's rock load prediction of 0.5B. Rock masses which exhibit through-going joints must be modeled differently and parameters such as joint length and bridge must be considered. In such rock masses with increasing joint length and decreasing rock bridges, the joint intersection (and block formation) probability increases, and consequently the total number of blocks in such rock masses increases. This results in more vertical deformations, expressed in greater surface settlements above the excavated opening. It is found that a rock mass rich in through-going joints exhibits greater vertical deformation and surface settlements above deep underground openings when compared to mechanically layered rock masses when the total number of blocks is kept equal. This is because through-going joints provide continuous surfaces for vertical shear displacements whereas in a mechanically layered rock masses the extent of vertical joints is limited by bedding plane boundaries and so are the vertical displacements. It is also reasonable to assume that mechanically layered configurations attain better interlocking between blocks, a process which further restricts vertical displacements in such rock masses.

With increasing bridge length the number of blocks per layer decreases. This is particularly significant in the stabilization of the immediate roof, because immediate roof

beam stability increases with increasing block width, up to an optimal block width beyond which the load due to beam weight dominates over arching (see Figure 3-10).

6.2 Seismically induced dynamic sliding of tetrahedral wedge

A new algorithm for dynamic sliding in three dimensions is presented in this research based on the static limit equilibrium equations suggested by Goodman and Shi (1985). The newly developed algorithm is found to be suitable for analyzing the dynamic response of a single block for both single and double plane sliding. Effective application of this algorithm however requires that the failure mode is assumed in advance.

A very good agreement between Newmark's method on one hand and the new 3D algorithm and 3D-DDA on the other is observed using theoretical dynamic problems, with high sensitivity to the choice of numerical penalty indicated in 3D-DDA. Dynamic 3D-DDA is applied in two loading modes ("load" and "displacement") both of which provide similar results, with the "displacement" mode found to be more sensitive to the choice of numerical penalty.

The friction coefficient of the tested concrete interface exhibits velocity weakening behavior. Several tens of loading cycles are required for onset of friction degradation when, as in this case, the input amplitude is slightly higher than the static yield acceleration. The number of loading cycles required for onset of friction degradation is found to be inversely proportional to the shaking amplitude.

A logarithmic relationship between friction coefficient and sliding velocity is observed with the velocity spanning five orders of magnitude, the linear trend of which confirms the Dieterich-Ruina "rate and state" variable friction law. The A - B value obtained from slow direct shear tests is one order of magnitude lower than a single value obtained from the entire suite of test data including rapid shaking table experiments. Extrapolation from slow rate direct shear test data to fast sliding rates therefore proves inaccurate, and from an engineering standpoint - unconservative. Hence, the velocity-dependent friction degradation, as determined in lab experiments, must be integrated into dynamic rock slope analyses in order to receive more realistic results.

6.3 Thermally induced “ratchet” model for rock slope stability

In addition to the seismically triggering dynamic sliding, comprehensive data on the thermal response of a monitored rock block in the slopes of the Masada Mountain are presented in this study. A new thermally induced "ratchet" mechanism is suggested to explain qualitatively the observed annual accumulated translation of the monitored block in the West slope of the mountain. It is shown that the thermally induced "ratchet" model is sufficient for significant cumulative translation of a distinct block that is bounded by a tension crack at the back and that rests on a discontinuity that provides the sliding plane. The thermally-induced "ratchet" mechanism may explain rock failure episodes occurring more frequently than is generally assumed or explained, as it is inferred from the comparison between thermal and seismic driving mechanisms for block sliding at the 'Snake Path cliff" in the East slope of Masada. Moreover, it is shown that the thermal induced sliding can also occur on shallow dipping planes, which are usually considered as stable configurations. Therefore, understanding the mechanism of the “ratchet” model, and identifying its potential in the field, can help mitigate rock slope stability risks in rock masses that are prone to such a failure mechanism.

While only preliminary analyses have been conducted and presented in this dissertation, it is recommended that in future researches the feasibility of the 'ratchet" mechanism should be studied more deeply under controlled conditions in lab and by using coupled thermo-mechanical solutions.

APPENDIX 1 – MATLAB FUNCTIONS FOR BLOCK SLIDING IN 3D

Single face sliding

```
function BlockDisp = BlockOnIncline(time, rx, ry, rz, Dip, DipDir, phi)

%  input:
%  time - time vector, in seconds; with length L and dimensions LX1
%  rx, ry, rz - resultant acceleration vectors, in m/sec^-2 ; each with
   dimensions LX1
%  Dip  - the inclination of the plane, degrees.
%  DipDir - dip direction of the plane, clockwise azimuth from the north, degrees.
%  phi -  friction angle
%
%  output:
%  BlockDisp - the 3 components calculated block displacement, in meters.

L = length(time);
dt = time(end) / (L-1);          % time step size
nx = sind(Dip) * sind(DipDir);   % x component of plane
ny = sind(Dip) * cosd(DipDir);   % y component of plane
nz = cosd(Dip);                  % z component of plane
n = zeros(L,3); p=n; f=n;        % Preparing matrixes in dimensions: LX3

n(:,1) = nx;
n(:,2) = ny;
n(:,3) = nz;

r=[rx ry rz];                    % resultant force
m=cross(cross(n,r),n);           % driving force

V=[0 0 0];D=[0 0 0];             % Velosity & Displacement at t(0)

% For the first time step:
p(1,:) = n(1,:) * dot(n(1,:),r(1,:));   % (normal force)
% the resisting force:
f(1,:) = tand(phi) * norm(p(1,:)) * ((m(1,:)) / norm(m(1,:)));
if norm(f(1,:))>=norm(m(1,:));
        f(1,:) = m(1,:);
end

s(1,:) = m(1,:) - f(1,:);  % sliding force
S(1,:) = s(1,:);

% For each time step:
for i=[2:L]
    p(i,:) = n(i,:) * dot(n(i,:),r(i,:)); % (normal force)
    % the resisting force:
    if V(i-1,:) == 0;
        f(i,:) = -tand(phi) * norm(p(i,:)) * ((m(i,:)) / norm(m(i,:)));
        if norm(f(i,:)) > norm(m(i,:));
            f(i,:) = -m(i,:);
        end
    else
       f(i,:) = -tand(phi)*norm(p(i,:)) * ((V(i-1,:))/norm(V(i-1,:)));
    end

    s(i,:) = m(i,:)+f(i,:);                      % sliding force
    S(i,:) = 0.5*(s(i-1,:)+s(i,:));              % Acceleration
    V(i,:) = V(i-1,:)+dt*S(i,:);                 % Velosity
    D(i,:) = D(i-1,:)+dt*V(i-1,:)+S(i,:)*(dt)^2; % Displacement
end

BlockDisp = D;
%  The end of the code.
```

Double face sliding

```
function WedgeDisp = wedge(time, rx, ry, rz, Dip1, DipDir1, phi1, Dip2, DipDir2,
phi2)


%   input:
%   time - time vector, in seconds; with length L and dimensions LX1
%   rx, ry, rz - resultant acceleration vectors, in m/sec^-2 ; each with dimensions
    LX1
%   Dip1, Dip2  - the inclination of the planes, degrees.
%   DipDir1, DipDir2 - dip direction of the planes, clockwise azimuth from the
    north, degrees.
%   phi1, phi2 -  friction angles for each plane
%
%   output:
%   WedgeDisp - the 3 components calculated block displacement, in meters.


L = length(time);
dt = time(end) / (L-1);                 %time step size

nx1=sind(Dip1)*sind(DipDir1);           % x component of plane 1
ny1=sind(Dip1)*cosd(DipDir1);           % y component of plane 1
nz1=cosd(Dip1);                         % z component of plane 1
nx2=sind(Dip2)*sind(DipDir2);           % x component of plane 2
ny2=sind(Dip2)*cosd(DipDir2);           % y component of plane 2
nz2=cosd(Dip2);                         % z component of plane 2

n1=zeros(L,3);                          % [L,3] preparing matrix
n2=n1;
n1(:,1)=nx1;n1(:,2)=ny1;n1(:,3)=nz1;
n2(:,1)=nx2;n2(:,2)=ny2;n2(:,3)=nz2;

j=cross(n1(1,:),n2(1,:));

V=[0 0 0];D=[0 0 0];            % Velosity & Displacement at t(o)
r=[rx ry rz];                   %resultant force
for i=[1:L];
    m(i,:)=j*dot(r(i,:),j);     % driving force
end


p(1,:)=(dot(cross(r(1,:),n2(1,:)),j))*n1(1,:); % normal force of plane 1
q(1,:)=(dot(cross(r(1,:),n1(1,:)),j))*n2(1,:); % normal force of plane 2
f(1,:)=(tand(phi1)*norm(p(1,:)+tand(phi2)*norm(q(1,:)))*((m(1,:))/norm(m(1,:)));
% resist force
if norm(f(1,:))>norm(m(1,:));
        f(1,:)=-m(1,:);
end
s(1,:)=m(1,:)+f(1,:);                           %sliding force
S(1,:)=s(1,:);

for i=[2:L]
   p(i,:)=(dot(cross(r(i,:),n2(i,:)),j))*n1(i,:); % normal force of plane 1
   q(i,:)=(dot(cross(r(i,:),n1(i,:)),j))*n2(i,:); % normal force of plane 2

   % resisting force:
        if V(i-1,:)==0;
            f(i,:)=-
(tand(phi1)*norm(p(i,:))+tand(phi2)*norm(q(i,:)))*((m(i,:))/norm(m(i,:)));
            if norm(f(i,:))>norm(m(i,:));
                f(i,:)=-m(i,:);
            end

        else
```

```
            f(i,:)=-(tand(phi1)*norm(p(i,:))+tand(phi2)*norm(q(i,:)))*((V(i-
1,:))/norm(V(i-1,:)));

        end
    s(i,:)=m(i,:)+f(i,:);                              % sliding force


    S(i,:)=0.5*(s(i-1,:)+s(i,:));                      % Acceleration
    V(i,:)=V(i-1,:)+dt*S(i,:);                         % Velosity
    D(i,:)=D(i-1,:)+dt*V(i,:)+0.5*(dt)^2*S(i,:);    % Displacement
end

WedgeDisp = D;


%  The end of the code.
```

REFERENCE

Bai, T. and M. R. Gross (1999). Theoretical analysis of cross-joint geometries and their classification. *Journal of Geophysical Research-Solid Earth* 104(B1), p:1163-1177.

Bakun-Mazor, D., Y. H. Hatzor and W. S. Dershowitz (2009). Modeling mechanical layering effects on stability of underground openings in jointed sedimentary rocks. *International Journal of Rock Mechanics and Mining Sciences* 46(2), p:262-271.

Bakun-Mazor, D., Y. H. Hatzor and S. D. Glaser (2012). Dynamic sliding of tetrahedral wedge: The role of interface friction. *International Journal for Numerical and Analytical Methods in Geomechanics* 36(3), p:327-343.

Barton, N., R. Lien and J. Lunde (1974). Engineering classification of rock masses for the design of tunnel support. *Rock Mechanics and Rock Engineering* 6(4), p:189-236.

Beer, G. and J. Meek (1982). Design curves for roofs and hanging-walls in bedded rock based on'voussoir' beam and plate solutions. *Institution of Mining and Metallurgy Transactions* 91, p:A18-A22.

Begin, Z. B. (2005). Destructive Earthquakes in the Jordan Valley and the Dead Sea - their Recurrence Intervals and the Probability of their Occurrence, Geological Survey of Israel, Report No. 12/05, p.

Ben-Menahem, A. (1991). Four thousand years of seismicity along the Dead Sea rift. *Journal of Geophysical Research* 96(B12), p:20195-20216.

Bieniawski, Z. (1989). *Engineering rock mass classifications*. New York, John Wiley & Sons.

Biran, O., Y. H. Hatzor and A. Ziv (2010). Micro-scale roughness effects on the friction coefficient of granite surfaces under varying levels of normal stress. *Meso-scale shear physics in earthquake and landslide mechanics*. Y. H. Hatzor, J. Sulem and I. Vardoulakis, CRC Press/Balkema, p: 145-156.

Boore, D. M., W. B. Joyner and T. E. Fumal (1997). Equations for estimating horizontal response spectra and peak acceleration from western North American earthquakes: a summary of recent work. *Seismological Research Letters* 68(1), p:26.

Carslaw, H. S. and J. C. Jaeger (1959). *Conduction of heat in solids*. Oxford, London, Clarendon Press.

Corsmeier, U. (2006). Meteorological Observation and Assimilation of the Atmosphere on Long term (Dead Sea, Israel). from http://www.imk-tro.kit.edu/english/4520_3690.php.

Cravero, M. and G. Iabichino (2004). Analysis of the flexural failure of an overhanging rock slab. *International Journal of Rock Mechanics and Mining Sciences* 41(3), p:475-475.

Cundall, P. A. (1988). Formulation of a 3-Dimensional Distinct Element Model .1. A Scheme to Detect and Represent Contacts in a System Composed of Many Polyhedral Blocks. *International Journal of Rock Mechanics and Mining Sciences & Geomechanics Abstracts* 25(3), p:107-116.

Cundall, P. A. and O. D. L. Strack (1979). Discrete Numerical-Model for Granular Assemblies. *Geotechnique* 29(1), p:47-65.

Davies, T. R. and M. J. McSaveney (2009). The role of rock fragmentation in the motion of large landslides. *Engineering Geology* 109(1-2), p:67-79.

Dershowitz, B., et al. (2000). Integration of discrete feature network methods with conventional simulator approaches. *Spe Reservoir Evaluation & Engineering* 3(2), p:165-170.

Dershowitz, W. S. and H. H. Einstein (1988). Characterizing Rock Joint Geometry with Joint System Models. *Rock Mechanics and Rock Engineering* 21(1), p:21-51.

Diederichs, M. S. and P. K. Kaiser (1999). Stability of large excavations in laminated hard rock masses: the voussoir analogue revisited. *International Journal of Rock Mechanics and Mining Sciences* 36(1), p:97-117.

Dieterich, J. H. (1979). Modeling of Rock Friction .1. Experimental Results and Constitutive Equations. *Journal of Geophysical Research* 84(Nb5), p:2161-2168.

Einstein, H. H., et al. (1983). The Effect of Discontinuity Persistence on Rock Slope Stability. *International Journal of Rock Mechanics and Mining Sciences* 20(5), p:227-236.

Evans, W. (1941). The strength of undermined strata. *Trans. Inst. Min. Metall* 50, p:475-500.

Franklin, J. A. and M. B. Dusseault (1988). *Rock engineering*. New York, NY, McGraw Hill Book Co.

Friedmann, S. J., G. Kwon and W. Losert (2003). Granular memory and its effect on the triggering and distribution of rock avalanche events. *Journal of Geophysical Research-Solid Earth* 108(B8), p:11.

Gischig, V. S., et al. (2011a). Thermomechanical forcing of deep rock slope deformation: 1. Conceptual study of a simplified slope. *Journal of Geophysical Research-Earth Surface* 116, F04010, Doi 10.1029/2011jf002006.

Gischig, V. S., et al. (2011b). Thermomechanical forcing of deep rock slope deformation: 2. The Randa rock slope instability. *Journal of Geophysical Research-Earth Surface* 116, F04011, Doi 10.1029/2011jf002007.

Goodman, R. and G. Shi (1985). *Block theory and its application to rock engineering*. New Jersey, Prentice-Hall Englewood Cliffs.

Goodman, R. E. (1976). *Methods of Geological Engineering in Discontinuous Rocks*. San Francisco, West Publishing Company.

Goodman, R. E. and H. B. Seed (1966). Earthquake induced displacements in sands and embankments. *J Soil Mech Foundation Div ASCE* 92(SM2), p:125-146.

Goren, L. and E. Aharonov (2009). On the stability of landslides: A thermo-poro-elastic approach. *Earth and Planetary Science Letters* 277(3-4), p:365-372.

Grayeli, R. and K. Hatami (2008). Implementation of the finite element method in the three-dimensional discontinuous deformation analysis (3D-DDA). *International Journal for Numerical and Analytical Methods in Geomechanics* 32(15), p:1883-1902.

Greif, V., K. Sassa and H. Fukuoka (2006). Failure mechanism in an extremely slow rock slide at Bitchu-Matsuyama castle site (Japan). *Landslides* 3(1), p:22-38.

Gross, M. R. (1993). The Origin and Spacing of Cross Joints - Examples from the Monterey Formation, Santa-Barbara Coastline, California. *Journal of Structural Geology* 15(6), p:737-751.

Gross, M. R. and Y. Eyal (2007). Throughgoing fractures in layered carbonate rocks. *Geological Society of America Bulletin* 119(11-12), p:1387-1404.

Gunzburger, Y., V. Merrien-Soukatchoff and Y. Guglielmi (2005). Influence of daily surface temperature fluctuations on rock slope stability: case study of the Rochers de Valabres slope (France). *International Journal of Rock Mechanics and Mining Sciences* 42(3), p:331-349.

Hamiel, Y., et al. (2009). The Seismicity along the Dead Sea Fault during the Last 60,000 Years. *Bulletin of the Seismological Society of America* 99(3), p:2020-2026.

Hart, R., P. A. Cundall and J. Lemos (1988). Formulation of a 3-Dimensional Distinct Element Model .2. Mechanical Calculations for Motion and Interaction of a System Composed of Many Polyhedral Blocks. *International Journal of Rock Mechanics and Mining Sciences & Geomechanics Abstracts* 25(3), p:117-125.

Hatzor, Y. H. (2003). Keyblock stability in seismically active rock slopes - Snake Path cliff, Masada. *Journal of Geotechnical and Geoenvironmental Engineering* 129(8), p:697-710.

Hatzor, Y. H., et al. (2004). Dynamic stability analysis of jointed rock slopes using the DDA method: King Herod's Palace, Masada, Israel. *International Journal of Rock Mechanics and Mining Sciences* 41(5), p:813-832.

Hatzor, Y. H. and R. Benary (1998). The stability of a laminated Voussoir beam: Back analysis of a historic roof collapse using DDA. *International Journal of Rock Mechanics and Mining Sciences* 35(2), p:165-181.

Hatzor, Y. H. and A. Feintuch (2005). The joint intersection probability. *International Journal of Rock Mechanics and Mining Sciences* 42(4), p:531-541.

Hatzor, Y. H. and R. E. Goodman (1997). Three-dimensional back-analysis of saturated rock slopes in discontinuous rock-a case study. *Geotechnique* 47(4), p:817-839.

Hatzor, Y. H., M. Talesnick and M. Tsesarsky (2002). Continuous and discontinuous stability analysis of the bell-shaped caverns at Bet Guvrin, Israel. *International Journal of Rock Mechanics and Mining Sciences* 39(7), p:867-886.

Hermanns, R. L., et al. (2004). Rock avalanching into a landslide-dammed lake causing multiple dam failure in Las Conchas valley (NW Argentina) - evidence from surface exposure dating and stratigraphic analyses. *Landslides* 1(2), p:113-122.

Hoek, E. and J. W. Bray (1981). *Rock slope engineering*. London, Institution of Mining and Metallurgy.

Hoek, E. and E. T. Brown (1997). Practical estimates of rock mass strength. *International Journal of Rock Mechanics and Mining Sciences* 34(8), p:1165-1186.

Israel Meteorological Service. (2011). Climate information. from http://www.ims.gov.il/IMSEng/CLIMATE.

Jiang, Q. H. and M. R. Yeung (2004). A model of point-to-face contact for three-dimensional discontinuous deformation analysis. *Rock Mechanics and Rock Engineering* 37(2), p:95-116.

Jing, L. (2003). A review of techniques, advances and outstanding issues in numerical modelling for rock mechanics and rock engineering. *International Journal of Rock Mechanics and Mining Sciences* 40(3), p:283-353.

Kamai, R. and Y. H. Hatzor (2008). Numerical analysis of block stone displacements in ancient masonry structures: A new method to estimate historic ground motions. *International Journal for Numerical and Analytical Methods in Geomechanics* 32(11), p:1321-1340.

Kanamori, H. and E. E. Brodsky (2004). The physics of earthquakes. *Reports on Progress in Physics* 67(8), p:1429-1496.

Kemeny, J. (2005). Time-dependent drift degradation due to the progressive failure of rock bridges along discontinuities. *International Journal of Rock Mechanics and Mining Sciences* 42(1), p:35-46.

Keneti, A. R., A. Jafari and J. H. Wu (2008). A new algorithm to identify contact patterns between convex blocks for three-dimensional discontinuous deformation analysis. *Computers and Geotechnics* 35(5), p:746-759.

Klerck, P. A., E. J. Sellers and D. R. J. Owen (2004). Discrete fracture in quasi-brittle materials under compressive and tensile stress states. *Computer Methods in Applied Mechanics and Engineering* 193(27-29), p:3035-3056.

Liu, J., X. J. Kong and G. Lin (2004). Formulations of the three-dimensional discontinuous deformation analysis method. *Acta Mechanica Sinica* 20(3), p:270-282.

Londe, P. F., G. Vigier and R. Vormeringer (1969). Stability of rock slopes, a three dimensional study. *J. Soil Mech Foundation Div ASCE* 95(SM7), p:235-262.

MacLaughlin, M., et al. (2001). Investigation of slope-stability kinematics using discontinuous deformation analysis. *International Journal of Rock Mechanics and Mining Sciences* 38(5), p:753-762.

Mandez, B., E. Botero and M. Romo (2009). A new friction law for sliding rigid blocks under cyclic loading. *Soil Dynamics and Earthquake Engineering* 29(5), p:874-882.

Marone, C., B. E. Hobbs and A. Ord (1992). Coulomb constitutive laws for friction - contrasts in frictional behavior for distributed and localized shear. *Pure and Applied Geophysics* 139(2), p:195-214.

Matasovic, N., E. Kavazanjian and J. P. Giroud (1998). Newmark seismic deformation analysis for geosynthetic covers. *Geosynthetics International* 5(1-2), p:237-264.

Mauldon, M. and J. G. Mauldon (1997). Fracture sampling on a cylinder: From scanlines to boreholes and tunnels. *Rock Mechanics and Rock Engineering* 30(3), p:129-144.

Moosavi, M., A. Jafari and S. Beyabanaki (2005). Dynamic three-dimensional discontinuous deformation analysis (3-D DDA) validation using analytical solution. *The Seventh international conference on the analysis of discontinuous deformation (ICADD-7)*, Honolulu, Hawaii.

Mufundirwa, A., et al. (2011). Analysis of natural rock slope deformations under temperature variation: A case from a cool temperate region in Japan. *Cold Regions Science and Technology* 65(3), p:488-500.

Narr, W. and J. Suppe (1991). Joint Spacing in Sedimentary-Rocks. *Journal of Structural Geology* 13(9), p:1037-&.

Newmark, N. M. (1965). Effects of earthquakes on dams embankments. *Geotechnique* 15(2), p:139-160.

Obert, L. and W. Duvall (1967). *Rock mechanics and the design of structures in rock*. New York, John Wiley & Sons.

Passaris, E. K. S., J. Q. Ran and P. Mottahed (1993). Stability of the Jointed Roof in Stratified Rock. *International Journal of Rock Mechanics and Mining Sciences & Geomechanics Abstracts* 30(7), p:857-860.

Pasten, C. (2012). Repetitive Loadings in Geomaterials. PhD Thesis. Georgia Institute of Technology, Atlanta, GA.

Ran, J. Q., E. K. S. Passaris and P. Mottahed (1994). Shear Sliding Failure of the Jointed Roof in Laminated Rock Mass. *Rock Mechanics and Rock Engineering* 27(4), p:235-251.

Rohsenow, W. M., J. P. Hartnett and Y. I. Cho (1998). *Handbook of heat transfer*, McGraw Hill, New York.

Ruf, J. C., K. A. Rust and T. Engelder (1998). Investigating the effect of mechanical discontinuities on joint spacing. *Tectonophysics* 295(1-2), p:245-257.

Ruina, A. (1983). Slip Instability and State Variable Friction Laws. *Journal of Geophysical Research* 88(Nb12), p:359-370.

Sagy, A., Z. Reches and A. Agnon (2003). Hierarchic three-dimensional structure and slip partitioning in the western Dead Sea pull-apart. *Tectonics* 22(1), p:17.

Schmitz, S. (2009). Untersuchung thermisch induzierter Hang- und Talwindsysteme am Toten Meer und deren Kopplung an größere Skalen. Institute for Meteorology and Climate Research, Karlsruhe Institute for Technology, Karlsruhe, Germay.

Scholz, C. H. (1998). Earthquakes and friction laws. *Nature* 391(6662), p:37-42.

Shapira, A., et al. (2007). Earthquake hazard assessments for building codes - final report. *Grant No. PCE-G-00-99-00038*, Geophysical Institute of Israel, p: 88.

Shi, G. (1988). Discontinuous Deformation Analysis - a new numerical method for the statics and dynamics of block system. PhD Thesis. Dept. of Civil Engineering, University of California, Berkeley.

Shi, G. H. (1993). *Block system modeling by discontinuous deformation analysis*. Southampton, UK, Computational Mechanics Publications.

Shi, G. H. (1999). Technical manual and verification for Keyblock codes of dynamic Newmark Method. Belmont, CA, DDA Company, p: 18.

Shi, G. H. (2001). Three dimensional discontinuous deformation analysis. *38th US Rock Mechanics Symposium*, Washington, DC, Balkema, Rotterdam.

Shi, G. H. and R. E. Goodman (1989a). Generalization of Two-Dimensional Discontinuous Deformation Analysis for Forward Modeling. *International Journal for Numerical and Analytical Methods in Geomechanics* 13(4), p:359-380.

Shi, G. H. and R. E. Goodman (1989b). The Key Blocks of Unrolled Joint Traces in Developed Maps of Tunnel Walls. *International Journal for Numerical and Analytical Methods in Geomechanics* 13(2), p:131-158.

SIM STRUMENTI. (2009). Products. from http://www.simstrumenti.com/en/products.html.

Sitar, N., M. M. MacLaughlin and D. M. Doolin (2005). Influence of kinematics on landslide mobility and failure mode. *Journal of Geotechnical and Geoenvironmental Engineering* 131(6), p:716-728.

Sofianos, A. I. (1996). Analysis and design of an underground hard rock voussoir beam roof. *International Journal of Rock Mechanics and Mining Sciences & Geomechanics Abstracts* 33(2), p:153-166.

Sornette, D., et al. (2004). Towards landslide predictions: two case studies. *Physica a-Statistical Mechanics and Its Applications* 338(3-4), p:605-632.

Taboada, A. and N. Estrada (2009). Rock-and-soil avalanches: Theory and simulation. *Journal of Geophysical Research-Earth Surface* 114, p:23.

Terzaghi, K. (1946). Load on tunnel supports. *Rock tunneling with steel supports*. P. R.V. and W. T.L. Ohio, Commercial Shearing Inc, p: 47–86.

Tsesarsky, M., Y. H. Hatzor and N. Sitar (2005). Dynamic displacement of a block on an inclined plane: Analytical, experimental and DDA results. *Rock Mechanics and Rock Engineering* 38(2), p:153-167.

Vardoulakis, I. (2000). Catastrophic landslides due to frictional heating of the failure plane. *Mechanics of Cohesive-Frictional Materials* 5(6), p:443-467.

Vargas Jr, E., et al. (2009). Is thermal fatigue a possible mechanism for failures of some rock slopes in Rio de Janeiro, Brazil? *the 43rd US Rock Mechanics Symposium and 4th U.S.-Canada Rock Mechanics Symposium*. ARMA. Asheville, NC, Curran Associates, Inc., p: 8.

Veveakis, E., I. Vardoulakis and G. Di Toro (2007). Thermoporomechanics of creeping landslides: The 1963 Vaiont slide, northern Italy. *Journal of Geophysical Research-Earth Surface* 112(F3), p:21.

Vicko, J., et al. (2009). Rock displacement and thermal expansion study at historic heritage sites in Slovakia. *Environmental Geology* 58(8), p:1727-1740.

Wang, J., G. Lin and J. Liu (2006). Static and dynamic stability analysis using 3D-DDA with incision body scheme. *Earthquake Engineering and Engineering Vibration* 5(2), p:273-283.

Wartman, J., J. D. Bray and R. B. Seed (2003). Inclined plane studies of the Newmark sliding block procedure. *Journal of Geotechnical and Geoenvironmental Engineering* 129(8), p:673-684.

Watson, A., D. Moore and T. Stewart (2004). Temperature influence on rock slope movements at Checkerboard Creek. *Landslides: Evaluation and Stabilization, Proceedings of the Ninth International Symposium on Landslides*, Rio de Janeiro, Brazil., London:Taylor & Francis Group.

Whipple, K. X., G. S. Hancock and R. S. Anderson (2000). River incision into bedrock: Mechanics and relative efficacy of plucking, abrasion, and cavitation. *Geological Society of America Bulletin* 112(3), p:490-503.

Yan, L. (1991). Seismic deformation analysis of earth dams: a simplified method. *Soil Mechanics Laboratory*. Pasadena, California Institute of Technology, p.

Yeung, M. R., Q. H. Jiang and N. Sun (2003). Validation of block theory and three-dimensional discontinuous deformation analysis as wedge stability analysis methods. *International Journal of Rock Mechanics and Mining Sciences* 40(2), p:265-275.

Yeung, M. R., Q. H. Jiang and N. Sun (2007). A model of edge-to-edge contact for three-dimensional discontinuous deformation analysis. *Computers and Geotechnics* 34(3), p:175-186.

Zaslavsky, Y. and A. Shapira (2000). Questioning nonlinear effects in Eilat during MW= 7.1 Gulf of Aqaba earthquake. *Proceedings of XXVII General Assembly of the European Seismological Commission (ESC), Lisbon, Portugal*, p:343-347.

Zaslavsky, Y., A. Shapira and A. A. Arzi (2002). Earthquake site response on hard rock-empirical study. *Stability of rock structures: Proceedings of the Fifth International Conference of Analysis of Discontinuous Deformation*. Y. H. Hatzor. Lisse, Balkema Publishers, p: 133-144.